The Self-Assembly of Surfactants in Ordered Mesoporous Silica Studied by Neutron Scattering

vorgelegt von
Diplom-Physiker
Tae Gyu Shin
aus Geoje, Südkorea

Von der Fakultät II – Mathematik und Naturwissenschaften
der Technischen Universität Berlin
zur Erlangung des akademischen Grades

Doktor der Naturwissenschaften
Dr. rer. nat.

genehmigte Dissertation

Promotionsausschuss :

Vorsitzender: Prof. Dr. P. Strasser
Berichter: Prof. Dr. G. H. Findenegg
Berichter: Prof. Dr. M. Gradzielski
Berichter: Prof. Dr. O. Paris

Tag der wissenschaftlichen Aussprache : 13. Juli 2010

Berlin 2010

D 83

Zusammenfassung

Shin, Tae Gyu

Strukturuntersuchungen von Tensidaggregaten in den Poren von mesoporösen SBA-15 Materialien mittels SANS.

In dieser Arbeit wurden die Struktur und die Gestalt der Aggregaten von nicht-ionischen und kationischen Tensiden in den Poren vom mesoporösen Silikat SBA-15 durch Neutronen Kleinwinkelstreuung untersucht. Aufgrund der unterschiedlichen Wechselwirkungsstärken von Kopfgruppen mit der Porenwand und von der hydrophoben Anziehung der Alkylketten untereinander, wurden unterschiedliche Streukurven für jeweiligen SBA-15 Proben beobachtet, die mit verschiedenen Typen von Tensiden und bei verschiedenen Beladungen adsorbiert waren. SBA-15 Materialien weisen 2D hexagonale Anordnung von zylindrischen Poren auf, wobei die Porenweite, die spezifische Oberfläche, das Porenvolumen und die Gitterkonstante mittels N_2-adsorption und SAXS charakterisiert werden. Für einige Tenside waren vor der Neutronstreumessung Adsorptionsmessung erforderlich.

Die Neutron-Streukurven von den stark adsorbierenden nicht-ionischen Tensiden $C_{10}E_5$ und $C_{12}E_5$ weisen eine Überlagerung von diffuser Kleinwinkelstreuung mit Bragg-Reflexen auf und konnten mittels einer passenden Modellfunktion (modifizierte Teubner-Strey Funktion) gefittet werden. Die Ergebnisse dieser Analyse liefern den mittleren Abstand zwischen Tensidaggregaten d, die Korrelationslänge ξ, und die mittlere Dicke der Tensidschicht t. Bei zunehmender Beladung von Tensid wird d kleiner, wobei ξ und t größer werden. Dies besagt, dass die Tensidmoleküle bei der kleinen Beladung zunächst in einem größeren Abstand isoliert aggregieren (Oberflächenmizelle), mit zunehmender Beladung die Abstände zwischen den Aggregaten kleiner und diese Aggregate dann bei der höchsten Beladung zu einer Tensidschicht vernetzt werden.

Für die SBA-15 Proben mit dem schwach adsorbierenden $C_{10}G_2$ wurde der Formfaktor der Kugelmizellen angewendet, um die Streudaten zu fitten. Die mit $C_{10}G_1$ adsorbierte SBA-15 Probe zeigt jedoch eine Überlagerung von einer Streukurve der zylindrischen Mizellen und *(10*) Bragg-Peak der 2D hexagonalen Anordnung von Mesoporen.

Die Streukurven von den mit kationischen Tensiden adsorbierten SBA-15 Proben konnten mit der modifizierten Teubner-Strey Modellfunktion nicht analysiert werden. Der Grund dafür besteht darin, dass die Streukurven nur bei den höchsten zwei Beladungen 4 führende Bragg-Peaks zeigen, wodurch die Fit-Analyse sehr eingeschränkt möglich ist.

Die Ergebnisse der TGA Messungen konnten dazu verwendet werden, um die Plateauwerte der Adsorptionsmessungen zu vergleichen, so dass tatsächliche Plateauwerte der Adsorption in der vorliegenden Arbeit qualitativ überprüft werden konnten.

Abstract

Shin, Tae Gyu

The Self-Assembly of Surfactants in Ordered Mesoporous Silica Studied by Neutron Scattering.

In this work the structure and the shape of the aggregates of nonionic and cationic surfactants in the pores of mesoporous silica SBA-15 were investigated by neutron scattering. Due to the different strengths of interaction of the head groups with the pore wall and the hydrophobic attraction between the alkyl chains, different scattering curves for the respective SBA-15 samples which were adsorbed with various types of surfactants and at different loadings were observed. SBA-15 materials show 2D hexagonal arrangement of cylindrical pores, where the pore size, the specific surface, the pore volume and the lattice constant were characterized by N_2-adsorption and SAXS. For some surfactants, adsorption measurements were required prior to the neutron scattering measurement.

The neutron scattering curves of the strongly adsorbing nonionic surfactants $C_{10}E_5$ and $C_{12}E_5$ show a superposition of diffuse small-angle scattering with Bragg reflections and could be fitted using a suitable model function (modified Teubner-Strey function). The results of this analysis provide the mean distance between surfactant aggregates d, the correlation length ξ, and the average thickness of the surfactant layer t. With increasing surfactant loading, d becomes smaller, while ξ and t become greater. This says that at small loading the surfactant molecules aggregate at first in a larger distance (isolated surface micelles), with increasing surfactant amount the distances between the aggregates become small and these aggregates are then interconnected to a patch-like surfactant layer at the highest loading.

For the SBA-15 samples adsorbed by weakly adsorbing $C_{10}G_2$ the form factor of spherical micelles was applied in order to fit the scattering data. On the other hand, the SBA-15 sample with adsorbed $C_{10}G_1$ shows a superposition of a scattering curve of the cylindrical micelles and *(10)* Bragg peak of the 2D hexagonal arrangement of the mesopores.

The scattering curves of SBA-15 samples with adsorbed cationic surfactants could not be analyzed with the modified Teubner-Strey model function. The reason is that the scattering curves show only the two highest loadings leading four Bragg peaks, making the Fit-analysis very limited.

The results of the TGA measurements could be used to compare the plateau values of the adsorption measurements, which allow qualitative check of the actual plateau values of adsorption in the present work.

Contents

Chapter 1

Introduction

The purpose of the present work has been to provide a better understanding of the structure of surfactant aggregates in pores of mesoscopic size and well-defined geometry. A surfactant, a shortened form of "*surf*ace-*ac*tive *a*g*ent*", is a chemical that reduces the surface tension of water by adsorbing at the liquid-gas interface, or the interfacial tension between oil and water by adsorbing at the liquid-liquid interface. Surfactants are usually organic compounds composed of a hydrophobic tail group and a hydrophilic head group. This amphiphilic nature of surfactants makes them soluble in both organic solvents and water.

The adsorption of surfactants at solid/liquid interfaces is of enormous importance in many fields of technological, environmental and biological importance, such as cleaning and detergency, wetting, spreading and lubrication, paint and food technology, and cosmetics. In most of these applications the essential role of the surfactant results from its amphiphilic character, which causes the molecules to assemble to micellar aggregates in selective solvents like water, and to adsorb to surfaces due to the preference of the surface for either the hydrophilic or hydrophobic moieties of the surfactant.

To obtain structural information about surfactant adsorbed layers at solid/water interfaces with atomically flat solid substrates, several techniques have been employed, including scanning force microscopy (AFM) [Gran98, Warr00], neutron reflectometry [Pen02, How01] and grazing incidence small-angle neutron scattering (GISANS) [Stei04]. For flat hydropholic silica substrates, laterally homogeneous bilayers are reported [Gran98].

Figure 1.1 Possible structures of surfactant aggregate adsorbed on flat surface.

The structure of surfactant layers adsorbed on colloidal silica has been studied by SANS [Cumm90, Des03, Lug09], where it was found that the nonionic surfactant n-dodecyl-penta(ethylene glycol) ($C_{12}E_5$) is forming globular surface micelles on silica nanoparticles. On the other hand, little is known about the structure of surfactant adsorbates in narrow pores, when confinement and curvature effects become important. ^{2}H nuclear-magnetic resonance [Qiao03] and adsorption flow microcalorimetry [Dra02] studies indicate that these effects can indeed become significant when the pore size is approaching the characteristic length of the surfactant aggregate, which is of the order of a few nanometers. Adsorption isotherm measurements indicate that the maximum surface concentration Γ_{max} (plateau value of the adsorption isotherm) as well as the critical surface aggregation concentration (csac) of the surfactant decreases significantly as the pore width is decreased [Diet07, Gior92]. However, the structural implications of these effects are not yet fully understood also due to the lack of well-defined high quality nanoporous material.

Surface micelle in pore Adsorbed bilayer

Figure 1.2. Possible structures of surfactant aggregate adsorbed in pores.

In this context the Periodic Mesoporous Silica (PMS), one of outstanding developments in nanotechnology, is suggested as an appropriate candidate for adsorbent to enlighten the structural aspects of surfactant aggregate in the narrow pores of nanoscopic scale. This novel material has applications in catalysis, drug delivery and imaging [Arai08, Leer05, Nala08, Schm06, Tale01]. Periodic mesoporous silicas such as MCM-41 and SBA-15 (SBA stands for Santa Barbara Amorphous type material) comprise arrays of cylindrical pores which are arranged parallel to each other in a 2D hexagonal symmetry (space group P6mm). The pore diameter can typically be adjusted in a range of 2-5 nm (MCM-41) and 5-15 nm (SBA-15).

In the present work, the SBA-15 samples of uniform pore size (8 nm in diameter) have been employed.

For the aggregate structure of surfactants in pores with hydrophilic surfaces two limiting situations can be envisaged (see Figure 1.2). If the behaviour is dominated by the interaction of the surfactant heads or tails with the surface, adsorption may lead to a laterally uniform film. Alternatively, if the behaviour is dominated by the hydrophobic interaction between the surfactant tails, surface aggregation to surface micelles will prevail. Moreover, when the width of the pore is approaching the size of the surfactant aggregates, the effect of geometrical confinement in narrow pores may further influence the structure of surfactant aggregates.

Few surfactant adsorption measurements on SBA-15 have been reported in the literature. From their sigmoidal shape, however, the formation of surface aggregates has been suggested. Some studies indicate that the critical surface aggregation concentration may depend on the pore size [Find07].

In the present work, the self-assembly of cationic and nonionic surfactants in the pores of SBA-15 was investigated, in order to asses the influence of the head-group interaction with the silica surface, and the influence of the tail length on the surface aggregation. Alkyl pyridinium chloride surfactants have a relatively small head group (the pyridinium ion). Due to their positive charge, the head groups of these surfactants have a rather strong interaction with the negative charges of the silica surface.

Nonionic surfactants of the alkyl polyoxyethylene family

$$C_nH_{2n+1}(OCH_2CH_2)_mOH \text{ (abbreviated } C_nE_m)$$

have large head groups which are strongly hydrated in aqueous media. The interaction of the polyoxyethylene group with the surface is mostly due to hydrogen bonds with surface silanol groups.

Alkyl glucosides are composed of a glucosyl moiety (one or several units) linked to the hydroxyl group of a fatty alcohol which may be a normal-chain, a branched-chain or a phenolic alcohol. The index *n* indicates the length of hydrocarbon chain and the index *m* represents the number of glucose units. The hydrophobic hydrocarbon chain is formed by a fatty alcohol obtained from palm kernel oil or coconut oil. The tension-active properties depend on the length of the carbon chain. The hydrophilic part of the molecule is based on glucose (dextrose)

obtained from starch. Depending on the structure of employed sugar modules they are called as glucosides, galactosides, maltosides, mannosides and so on. Decyl glucoside, decyl maltoside and dodecyl glucoside are selected in the present work.

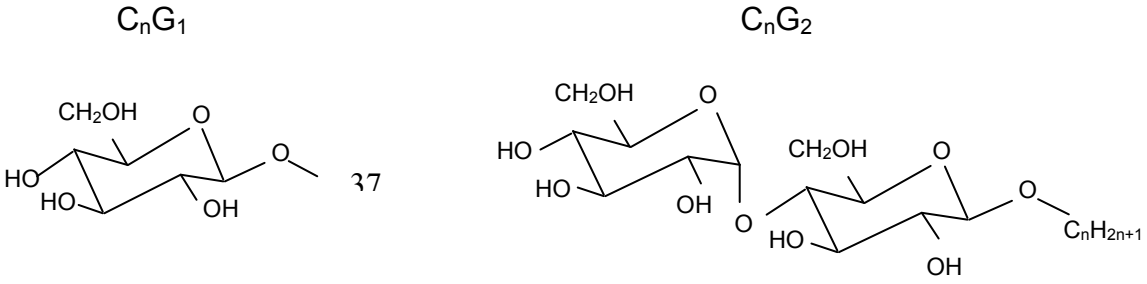

Neutron small-angle scattering (SANS) method was employed to study the organisation of surfactant aggregates adsorbed in the cylindrical pores of periodic mesoporous silica such as SBA-15. By using contrast matching mixture of H_2O/D_2O to silica matrix, the prominent Bragg reflexes from 2D hexagonal arrangement of cylindrical nanopores can effectively be suppressed to enlighten the structural aspects of the surfactant aggregates adsorbed in the SBA-15 silica.

Present thesis is organized as follows:
Chapter 2 gives a compact overview of fundamental description about the surface chemistry of silica in aqueous solution as well as the adsorption and self-assembly of the surfactants in mesoporous silica material. Chapter 3 deals with experimental background such as scattering theory and principles of other experimental methods employed for the investigation. In chapter 4, details of performed experiment will be documented. Experimental details and results of supplementary measurements such as adsorption isotherm measurement and thermogravimetric analysis will be presented in Chapter 5. The results of Small-angle Neutron Scattering experiment and their analysis are presented in Chapter 6 (cationic surfactants) and Chapter 7 (non-ionic surfactants).

The present work was performed in the framework of Sonderforschungsbereich 448, *Mesoskopisch strukturierte Verbundsysteme*. It involved a co-operation with the Department Biomaterials at the Max-Planck-Institut für Kolloid- und Grenzflächenforschung, Wissenschaftspark Golm, Potsdam, Germany.

Chapter 2

Theoretical background

In this chapter the theoretical backgrounds about the investigated systems, such as adsorption behaviour of surfactants in a confined geometry under various chemical conditions, and the surface chemistry of silica in aqueous solution will be presented. It is well known that surfactants in aqueous solutions self-organize into various aggregates of characteristic size and shape (spheres, cylinders or platelets) depending on the nature of the surfactant and properties of the solution (CMC, concentration, temperature, pH, and salinity). The intrinsic parameters affecting the shape of surfactant aggregates are the head group size and the length (and volume) of the hydrophobic tail. It is well established that surfactants with large head groups and short tails tend to form spherical micelles, while surfactants with small head groups and long tails tend to form aggregates of lower mean curvature. The extrinsic influence by the solution properties often arises from the fact that the effective head group size depends on these parameters. In section 2.2 these influences on the aggregate size and shape will be presented.

In the following, the behaviour of surfactant molecules in aqueous solution and at the interfaces, influence of various parameters such as pH, temperature, concentration, salinity and geometrical confinement will be described and shortly be discussed with respect to the performed experiments.

2.1 Surface chemistry of silica in aqueous solution

It is generally accepted that surface silicon atoms tend to have a complete tetrahedral configuration and that in an aqueous medium their free valence becomes saturated with hydroxyl groups, forming silanol groups [Berg94]. They are formed on the silica surface during the condensation-polymerization of $Si(OH)_4$ or as a result of rehydroxylation of thermally dehydroxylated silica when treated with water or aqueous solutions. The surface silanol groups are generally classified in three categories (an isolated silanol, geminal silanol or silanediols, and vicinal or H-bonded or associated silanols) depending on their nature,

multiplicity of sites (Q^n, where n is the number of bridging oxygens bonded to the central silicon in NMR terminology), and type of association [Bunt07].

On an oxidic surface, either H^+ or OH^- ions can be adsorbed depending on the pH value of solution, so that silica surface may cary differently charged surface silanol groups, respectively. The silanol groups of silica surfaces at basic and neutral conditions are slightly acidic, so that they react with water as follows:

$$\equiv Si\text{-}OH + H_2O \leftrightarrows \equiv Si\text{-}O^{\ominus} + H_3O^{\oplus} \tag{2.1}$$

At low pH the silica surface can act as proton acceptor according to

$$\equiv Si\text{-}OH + H_3O^{\oplus} \leftrightarrows \equiv Si\text{-}OH_2^{\oplus} + H_2O \tag{2.2}$$

Thus the electrical nature of the silica-water interface is strongly determined by the pH of the aqueous phase. In the presence of a background electrolyte, the hydroxylated silica surface has the isoelectric point near pH 2, at which the surface is uncharged. Accordingly, at basic and neutral conditions the silica surface is negatively charged, whereas at strongly acidic conditions the surface will be positively charged. At high pH values the degree of ionization of the surface silanol groups reaches its maximum value. This leads to a selective adsorption of cationic or anionic surfactants to the silica surface and makes silica to be a classical adsorbent to study adsorption of cationic surfactant on negatively charged surface.

Silica surfaces are partially hydrophobic due to the presence of siloxane groups, thus the aliphatic surfactant tails can also interact favourably with the surface. The degree of hydrophobicity of silica surfaces increases when the silica is treated at high temperatures, which leads to a partial dehydration and increase of siloxane bonds at the surface. On such hydrophobic silica surfaces surfactants are adsorbed mainly with their hydrophobic moiety of the surfactant. On hydrophilic surfaces, OH groups are the main centers for the adsorption of water molecules, at low surface concentrations. For this reason, and because hydrogen bonding to surface silanol is postulated as the main adsorption mechanism, it cannot be excluded that the deuterium in heavy water may influence the adsorption condition of the surfactant molecules.

2.2 Surfactant aggregation in aqueous systems

Aqueous solutions of surfactants exhibit several special features because of the amphiphilic nature of the molecular structure. The hydrophilic part of the surfactant molecule is hydrated with a shell of water molecules. Water molecules next to the hydrocarbon chain of the surfactant rearrange in such a way that each molecule retains four hydrogen bonds to neighboring water molecules. This effect forces a structural reinforcement of the water structure around the hydrophobic part of the surfactant molecule. As a consequence, the separation of hydrophobic moieties of surfactant molecules from aqueous medium is entropically favoured. This in essence is the so-called hydrophobic effect. As a result, some of the surfactant molecules are expelled to the interfaces of the system, with their hydrophobic groups oriented in such a way, so as to minimize contact with water molecules and in this way lowering the free energy of the system. Accordingly, the hydrophobic effect leads to an enrichment of the surface with surfactant molecules. A single layer of surfactant molecules is formed with their hydrophobic groups oriented predominantly toward the air. The presence of surfactant at the air/liquid interface leads to a decrease of the surface tension, because the water molecules close to the interface will not be as constrained as it would be in the situation without the surfactant molecules.

Two important aspects among the essential criteria for these phenomena may be the CMC (*C*ritical *M*icelle *C*oncentration) and packing parameter $P = v/(a_0 l_c)$, where v is the volume and l_c the critical length of the hydrocarbon tail, and a_0 the effective head group area of the surfactant. It is well-established that the shape of surfactant aggregates depends strongly on the packing parameter, large values of P favoring flat aggregate structures and small values of P highly curved (spherical) aggregates. When the adsorption of surfactants occurs at silica/water-interface and additionally under geometrical confinement, the CMC as well as the packing parameter may change. The hydrophobic effect leads to the formation of aggregates of surfactant molecules ("micelles") in the aqueous phase above the certain system-characteristic concentration CMC. The CMC is the surfactant concentration at which micelles start to form. Upon reaching the CMC, any further addition of surfactants will cause an increase in the number of micelles rather than a growth of existing micelles. Typical micellar aggregation numbers lie in the range $N = 30 – 100$ [Evans94]. A set of important reference numbers for the packing parameter for surfactant aggregates is presented in Table 2.1.

Packing parameter *P*	Expected structure
$P < 1/3$	spherical micelles
$1/3 < P < 1/2$	cylindrical micelles
$1/2 < P < 1$	vesicles, flexible bilayers
$P \approx 1$	lamellar, planar bilayers
$P > 1$	inverse structures

Table 2.1. Possible structures of surfactant aggregates with respect to the packing parameter *P*.

When the surfactant concentration is further increased above the CMC, interactions between micelles become important in the micellar solution. Accordingly, micelles can become the building units of ordered mesophases. A typical phase diagram of a surfactant-water binary system is shown in Figure 2.1, where the typical succession of phases is shown for the binary system consisting of water as solvent and the nonionic surfactant $C_{12}E_5$ as the solute. Starting from monomeric surfactant molecules, the CMC will be reached by enhancing the amount of added surfactant. Above the CMC one can see an optically isotropic solution (L_1) in which the molecules are aggregated to micelles. At high surfactant concentration and low temperature ordered lyotropic mesophases are formed in the sequence 2D hexagonal (H_1), cubic (V_1) and lamellar (L_α). Not all possible lyotropic mesophases are to be observed for all surfactants, because their formation is strongly influenced by the molecular properties of individual surfactant molecules besides the external parameters such as water content, temperature and other parameters. Contrary to the mesophases formed by pure substances (thermotropic liquid crystals), the lyotropic mesomorphism not only depends on the temperature and pressure, but also on the contents of solute. For example, in Fig. 2.1 the domain of L_α phase is strongly dependent on temperature and extends into the region of low surfactant concentration at high temperatures. This can be explained by different amounts of water between the surfactant bilayers of the lamellar phase.

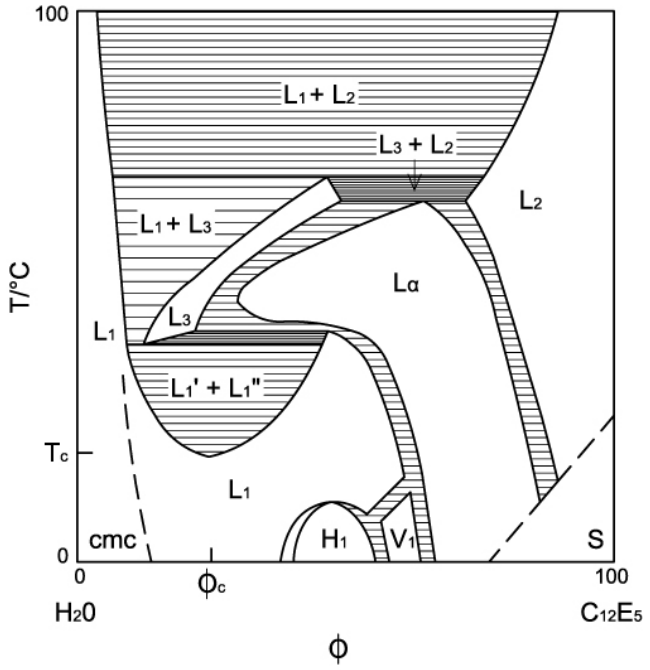

Fig.2.1. Temperature-surfactant volume fraction (T, Φ) phase diagram of the binary system H_2O - $C_{12}E_5$ after Strey et al [Strey90]. The volume fraction (Φ) axis is plotted on a non-linear scale to show the characteristics of dilute solutions.

Factors influencing the effective head group size

The effective head group size of a surfactant molecule can be changed in various ways, depending on the type of surfactant, which consequently influence the packing parameter. The head group of a non-ionic surfactant molecule in aqueous solution becomes dehydrated as the temperature increases, making it less hydrophilic and more compact, i.e., the effective head group area a_0 decreases. Accordingly, the packing parameter P will increase and the surfactant will tend to form aggregate structures of lower mean curvature. For example, in the phase diagram in Fig. 2.1 it is seen that in a certain range of surfactant concentrations the heaxagonal phase H_1 (which is made up of cylindrical micelles) is stable at lower temperatures, whereas at the same composition but high temperatures the lamellar phase L_α (which consists of flat surfactant bilayers) is stable.

For cationic surfactants such as the alkyl pyridinium salts C_nPCl, the concentration of electrolyte has a similar effect as temperature has for nonionic surfactants, because the effective size of their positively charged head groups is reduced due to the screening effect of the electrolyte. Thus, by changing the concentration of added salt the packing parameter of ionic surfactants and further, the shape of surfactant aggregate can be changed. Specifically, surface aggregation of cationic surfactants on silica surfaces is expected to occur only at high salt concentrations where the electrostatic repulsion of the head groups is minimized. This situation can be well understood in terms of the Debye-Hückel theory of electrolyte solution, which describes how the potential $\Phi(r)$ decreases exponentially with the distance around a spherical ion:

$$\Phi(r) = \frac{z_j e}{4\pi\varepsilon_r\varepsilon_0} \frac{\exp[-\kappa(r - R_{ion})]}{r(1+\kappa R_{ion})} \tag{2.3}$$

where z_j stands for the valency of central ion, $1/\kappa$ is the Debye screening length[1], r is the distance from the origin, and R_{ion} is the radius of central ion. This is an expression for the potential caused by a central ion, which states that the potential decays slowly (as $1/r$) at distances $r \ll 1/\kappa$ but rapidly (as $\exp(-\kappa r)$) at distances $r \gg 1/\kappa$. Accordingly, as the screening length $1/\kappa$ decreases when the ionic strength is increased, the range of the potential is decreasing parallel to $1/\kappa$ [Evans94].

2.3 Surfactant adsorption at the hydrophilic silica/water interface

Adsorption of surfactants from aqueous solutions onto solid surface can be regarded as a transfer process of surfactant molecules from the bulk solution phase to the surface or interface which is caused by a combination of hydrophilic and hydrophobic interactions of the surfactant

[1] The Debye length is distance from the charged surface into the solution within which the major portion of the electrical interactions with the surface can be considered to occur. This is given by $\frac{1}{\kappa} = \left(\frac{\varepsilon\varepsilon_0 k_B T}{e^2 \sum C_i z_i} \right)^{\frac{1}{2}}$, where $\varepsilon,\varepsilon_0$ are the dielectric constants of solution and in vacuum, respectively, k_B, T, e, C, z are the Boltzmann constant, absolute temperature, charge of electron, molar concentration of ion in solution and valency of ion in solution, respectively [Evans94].

molecules with the surface and the solvent, as well as interactions between the surfactant molecules. This results in an increase in the local concentration or surface concentration.
Adsorption onto hydrophilic surfaces can be well described by the so-called two-step adsorption mechanism, which is based on the assumption that the adsorption of surfactants on the solid/liquid interface generally occurs in two steps. In the first step, the surfactant adsorbs as individual molecules at active sites of the silica surface through specific intermolecular interaction. Then in the second step the adsorption increases dramatically as surface micelles form on the silica walls through association and hydrophobic interaction between hydrocarbon chains of the surfactants. Each of the molecules adsorbed during the first step provides possible active centers (nucleation sites or anchor molecules) for surface micellization.

Gu and Zhu derived an isotherm equation based on the two-step adsorption model for surfactants at the solid/liquid interface mentioned above [Zhu89]. The general isotherm equation for the two-step adsorption model is given as:

$$\Gamma = \frac{\Gamma_m k_1 C((1/n) + k_2 C^{n-1})}{1 + k_1 C(1 + k_2 C^{n-1})} \tag{2.4}$$

where Γ is the amount of surfactant adsorbed at concentration C, Γ_{max} is limiting adsorption at high concentrations, k_1 and k_2 are the equilibrium constants for the first and second step, respectively, and n is the number of monomers per surface micelle. This equation and the two-step adsorption model can be applied also for the surfactant adsorption in hydrophilic silica mesopores.

More detailed description about adsorption isotherms depending on the surfactant type, such as three-region adsorption isotherm for non-ionic surfactant in hydrophilic cylindrical nanopore or four-region adsorption isotherm for cationic surfactant on hydrophilic silica surface, can be obtained by varying k_1 and k_2 respectively [Zhu89]. Eq. 2.4 can be expressed in terms of Henry's law constant, K_H, and a reduced concentration, $x = c/c_0$, as

$$\Gamma = \frac{K_H c_0 x + (\Gamma_m / N) x^N}{1 + N K_H c_0 x / \Gamma_m + x^N / N} \tag{2.5}$$

where the critical surface aggregation concentration $c_0 = (Nk_1k_2)^{-1/N}$ and $K_H = k_1\Gamma_m/N$ [Diet07].

Influence of electrolyte on surfactant adsorption. Non-ionic surfactants are physically adsorbed rather than electrostatically adsorbed or chemisorbed at solid surfaces but electrolytes can alter their solubility, surface activity, and aggregation properties, which in turn may affect the adsorption at the solid-liquid interface. However, for non-ionic surfactants electrolyte effects are weak and play a role only at high salt concentrations.

For cationic surfactants, addition of electrolyte can lead more significant change in their adsorption and aggregation behaviour. When the surface charge density is relatively high, the driving forces of adsorption of cationic surfactants on silica are the Coulombic attractions between surfactant ions and charged surface groups and the hydrophobic interactions between hydrocarbon moieties. At surfactant concentrations well below the critical micelle concentration, specific interactions between the surfactant ions and the charged surface can also have a pronounced influence on the adsorption process.

At high electrolyte concentration the initial surface charges are much higher than at low electrolyte concentration so that the surfactant ions have to replace the ordinary counterions (ion exchange). The existing relatively high surface charge density reduces the surface hydrophobicity, but it increases the possibility for lateral hydrophobic tail-tail interactions. Nevertheless, the electrostatic attraction is low due to the screening by the salt ions. As a consequence, the adsorption starts later than at low salt concentration. An increase in ionic strength of the bulk solution also causes a screening of the electrostatic attraction between the surfactant head group and opposite charges on the silica surface, which leads to a decrease in adsorption [Golo96].

At low electrolyte concentration, the salt ions hardly contribute to the surface charge compensation in the presence of surfactant. Electrostatic repulsions between “head-on” adsorbed headgroups and local crowding prevent the aggregation process in the adsorbed layer. At low surface concentrations, the adsorption of cationic surfactants at silica surfaces can represent an ion exchange process in which protons of the silanol groups are released. Accordingly, adsorption is causing a pH change of the solution. Therefore, without careful pH control, pH changes may occur along an isotherm [Atki03]. Whereas salt concentration has only a small influence on adsorption in the first layer, adsorption in the second layer may increase significantly with salt concentration, as a consequence of the screening of the head-group repulsion.

For the cationic surfactants dodecyl pyridinium chloride (C_{12}PCl = DPCl) and cetyl pyridinium chloride (C_{16}PCl = CPCl) on a nonporous silica (Aerosil OX50), the adsorption isotherms were found to be strongly dependent on the salt concentration [Golo97]. Whereas at high c_{salt}

strongly cooperative adsorption similar to that of nonionic surfactants occurs, the isotherms at low c_{salt} show two regimes: An initial low-affinity regime dominated by surfactant-surface interactions, followed by a high-affinity regime attributed to surface aggregation of the surfactant. The low affinity regime extends over almost two orders of magnitude in surfactant concentration.

However, it is possible that this behaviour is modified in the case of the adsorption of the cationic surfactant in mesopores, where the long-range interaction may have no more effect due to the size of pores with a diameter of several nanometers. The validity of screening effect by electrolyte will be discussed in a context of interpreting TGA results in chapter 5.

2.4 Surfactants in hydrophilic silica pores (confinement effect)

In the cylindrical pores of periodic mesoporous silica, more or less pronounced one dimensional geometrical confinement is expected, depending on the pore diameter. Figure 2.2 shows adsorption isotherms of the nonionic surfactant C_8E_4 in two different ordered mesoporous silica materials, MCM-41 with 2.9 nm pore diameter and SBA-15 with 8.5 nm pore diameter. In both cases, the low-affinity initial region of the isotherm can be attributed to the binding of a small number of isolated 'anchor molecules' (the first step) and the steep increase of the isotherm at a concentration somewhat below the CMC (in the range of 0.6-0.9 CMC) to surface micelle formation (the second step), as implicated in the Gu-Zhu model.

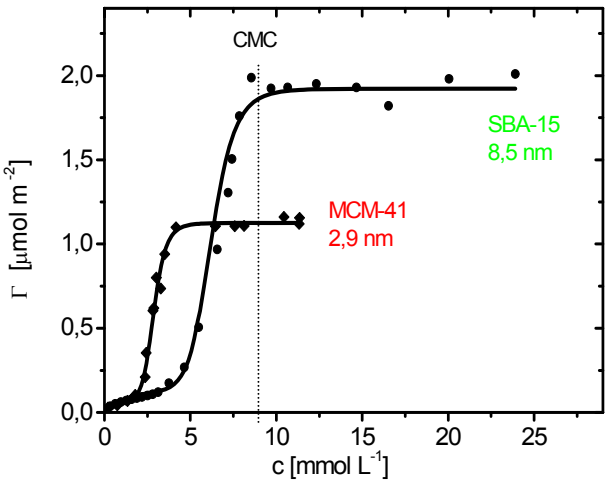

Figure 2.2: Adsorption isotherms of C_8E_4 in MCM-41 and SBA-15 silicas (points) and fit curves based onthe Gu-Zhu model (lines). Data from R. Dabiri [Dab02]. The influence of pore diameter on the critical surface aggregation concentration c_0 and the plateau value Γ_{max} is well demonstrated.

Two important features are shown in Figure 2.2: (i) With decreasing pore radius, the plateau value of adsorption Γ_{max} decreases and (ii) the critical surface aggregation concentration c_0 shifts to lower concentration. Further, while on flat surfaces the surfactant can form a symmetric bilayer film, geometrical constraints in cylindrical nanopores will prevent the formation of such a film if the pore radius is approaching the length scale of the thickness of such bilayer films. Surfactant surface aggregates of different structures can be envisaged to form in such cases: Small surface micelles or a highly distorted (and possibly fragmented) bilayer film. In either case, the total number of surfactant molecules per unit area will be less in case of geometrical confinement compared to the case of a flat surface.

If it is assumed that a laterally uniform surfactant layer is formed at the pore walls of the cylindrical pores, the thickness of such asymmetric layer t can be estimated as follows, because the pores of ordered mesoporous silica can be considered as nanotubes with infinite length [Find07]:

$$t = R\left(1 - \sqrt{1 - \varphi_{surf}}\right) \tag{2.6}$$

where R is the pore radius and φ_{surf} is the volume fraction of surfactant in the pore. φ_{surf} can be estimated from the volume of adsorbed surfactant per unit mass of silica, v_{surf}, and the specific pore volume v_p as

$$\varphi_{surf} = \frac{v_{surf}}{v_p} = \frac{n_{surf}}{v_p} V_{surf}\,, \tag{2.7}$$

where n_{surf} is the adsorbed amount per unit mass, and V_{surf} is the molar volume of the surfactant. For realistic estimates, the hydration of the surfactant head group has to be taken into account. For instance, for C_mE_n type surfactants, each ethylene oxide group (E) is hydrated by about two water molecules. Eq. 2.6 assumes that the surfactant forms a homogenous film at the pore walls. If only a fraction φ of the surface is covered by the film, a lower effective film thickness is expected.

The surfactant assembly in cylindrical nanopores has been studied by adopting the mean field lattice (MFL) theory for films of non-ionic surfactants [Huin97], where the structure and the field have been assumed to be homogeneous parallel to the surface. The situation may also hold in such cases where surfactant molecules build micellar aggregates or non-homogeneous films.

Chapter 3

Principles of Small-Angle Scattering (X-ray and neutron)

Small-angle scattering (SAS) techniques are powerful tools for performing a structural characterization of materials at length scales between 1 and 100 nm. For scattering experiments, X-rays of wavelengths from 0.5 to 2 Å and thermal neutrons of wavelengths from 1 to 10 Å are usually used. Elastic scattering of X-rays or neutrons delivers versatile possibilites for deriving information on the size and morphology of colloidal, and nanostructured materials of practical importance. Thus, by using SAS techniques processes such as self-assembly, aggregation, crystallization and phase separation can be studied at relevant conditions. Especially, to investigate molecular assemblies in confined geometry, such as surfactant aggregates in mesopores, neutron scattering methods are proved to be more suitable than X-ray scattering because: (1) direct imaging techniques for those systems such as high-resolution electron microscopy and tomography [Fried09, deJo06] are still under development (e.g. EM tomography) to deliver information about the structure for such systems, (2) neutrons can easily penetrate into a thick sample due to the weak interaction of neutrons with materials, and (3) the scattering contrast between sample constituents can be partly changed according to investigation scheme by simply exchanging isotopes.

3.1 General

Properties of X-ray and Neutron Radiation

For X-ray scattering experiments with laboratory equipment, the Cu-K_α line at wavelength λ = 1.542 Å is typically used, which has an energy of 8.0 keV according to Planck´s equation $E = hc/\lambda$, where $h = 6.626 \cdot 10^{-34}$ *J*s, $c = 3.0 \cdot 10^{8}$ m/s. Despite their high energy, X-rays are not so penetrating, because X-rays are scattered by the electron shell of the atoms in a similar way as light. On the other hand, neutron radiation penetrates materials very easily as neutrons are scattered by the nucleus which is very small compared to the electron clouds around it. This aspect is the most fundamental difference between neutron and electromagnetic radiation in scattering processes.

The wavelength of neutrons is given by the de Broglie relation $\lambda = h/p$, where p is the linear momentum, which for neutrons in thermal equilibrium with bath of temperature T is given by $p \propto \sqrt{m_n kT}$, where m_n is the mass of the neutron and k is the Boltzmann constant.

A typical wavelength range of cold neutrons is 0.01 – 3 nm, which are produced by nuclear reactors or spallation neutron sources. Because atomic nuclei are some 10^4 – 10^6 times smaller than typical neutron wavelengths, nuclei effectively behave as point scatterers. As a result the nuclear scattering remains constant on increasing scattering angle. In contrast, for X-rays the scattering decreases with increasing scattering angle in the case of X-rays, because atomic diameters are similar to the typical wavelength.

Scattering process

Scattering is a process of wave diffraction by a scattering body. Small-Angle X-Ray Scattering (SAXS) and Small-Angle Neutron Scattering (SANS) are static scattering techniques which are based on this wave diffraction phenomenon. In a scattering event the waves scattered at a given angle by all points in the sample interfere with each other to make up one point in an interference pattern. This can be transformed to reconstruct an image of all correlations in the sample. The motions of molecules are averaged over the measuring time by superposition of elastically scattered waves at scattering centers. Therefore information on dynamics of the system is lost. For static scattering, it is assumed that the relative motions of molecules are slow compared to the interaction time of the incident radiation.

Small-angle scattering means that the detection angles of scattered waves (2ϑ) are small in scattering experiment, typically in the range of $0.1° < 2\vartheta < 6°$. To express the scattering quantitatively, however, not the scattering angle, but the scattering vector is commonly used, which is defined as the difference between the incident wave vector $\vec{k}_i$ and the scattered wave vector $\vec{k}_f$. In case of elastic scattering we have no energy transfer, but a momentum change so that

$$k_i = \left|\vec{k}_i\right| = \left|\vec{k}_f\right| = k_f = \frac{2\pi}{\lambda} \tag{3.1}$$

as one can see in Figure 3.1.

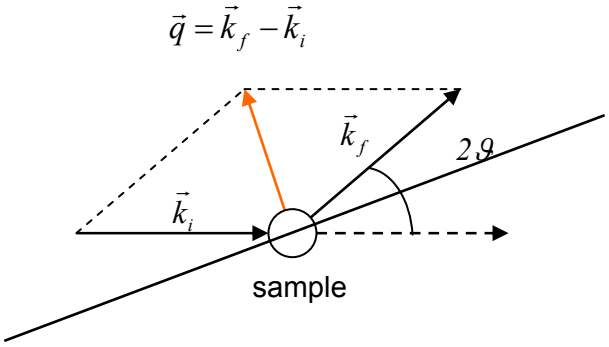

Fig. 3.1: Definition of scattering vector

The definition of q results in the following relation:

$$q = \left|\vec{q}\right| = \left|\vec{k}_f - \vec{k}_i\right| = \sqrt{k_f{}^2 + k_i{}^2 - 2k_f k_i \cos 2\vartheta} = \frac{4\pi}{\lambda} \cdot \sin(\vartheta) . \qquad (3.2)$$

For this definition it is assumed that the sample size is significantly smaller than the distance between sample and neutron source and between sample and detector (Fraunhofer approximation), so that both the incident and scattered wave field can be regarded as plane wave. This assumption holds in most situations for neutron scattering experiments. From Eq. (3.2) it can easily be seen that q has a dimension of (length)$^{-1}$. The q is conventionally expressed in nm^{-1} or Å^{-1}.

Scattering length density for neutrons

The neutron scattering length b_n is a measure for the distance on which the scattering centers and the incident radiation interact, that tells us how strong the sample scatters. As the dimensions of nucleus are much smaller than the neutron wavelength in the scattering experiment, b_n is independent of the scattering angle and represents a constant value for each isotope species. For a homogenous sample composed by several isotropic species i, the scattering length per unit volume (scattering length density ρ_n) is given by

$$\rho_n = N \cdot b_n = \sum_i b_{ni} \cdot \frac{D \cdot N_A}{M_W} , \qquad (3.3)$$

where D is the bulk mass density of the scattering body, M_W its molecular weight, N the number of scattering atoms per unit volume, N_A the Avogadro constant and b_n the bound coherent scattering length. ρ_n has a dimension of (length)$^{-2}$, because scattering length has been

divided by volume; typically ρ_n is expressed in units of 10^{10} cm^{-2} or 10^{-6} Å^{-2}. Depending on the value of b_n, ρ_n can also have negative value, as in the case of water (-0.56), octane (-0.53) and cyclohexane (- 0.28) because b_n can have a negative value. For example, $b_n(^1H)$ = -3.741 and b_n(Ti) = -0.382 [Caba87].

For structural investigations of a scattering sample, the coherent contribution to scattering will usually be used because this part of the scattered intensity arises from interference of different particles, while the incoherent scattering intensity does not depend on the scattering angle. For most nuclei the coherent scattering is stronger than the incoherent one with some exceptions, among which where the hydrogen atom (^{1}H) is a classical and important example.

General Expression for the Scattering Intensity

In a small-angle neutron scattering experiment a beam of collimated neutrons is directed at a sample and illuminates a small volume V with exactly defined thickness and cross-sectional area. Some of incident radiation is transmitted by the sample (T), some is absorbed and some is scattered into a solid angle Ω, where the sample transmission T is routinely measured for each sample by referencing incoming neutron flux to be merged in data reduction process. A detector counts then the flux of neutrons which are scattered and arrived on the detector element of size $dx \times dy$, placed at a distance of $L_{\text{Sample-Detector}}$ at scattering angle 2ϑ. Scattering intensity registered on the detector can be generally expressed as

$$I(\lambda,\vartheta) = I_0(\lambda)\cdot\Delta\Omega\cdot\eta(\lambda)\cdot T(\lambda)\cdot V\cdot\frac{\partial\sigma}{\partial\Omega}(q)\,. \tag{3.4}$$

The first three factors on the rights in this expression are dependent on the experimental setup: $I_0(\lambda)$ is the incoming flux and η the detector efficiency. The last three factors in equation (3.4) originate from physical properties of the sample. In particular, $(\partial\sigma/\partial\Omega)(q)$ is the differential scattering cross section which contains all relevant information on the system. In many cases this quantity, also called the scattered intensity $I(q)$ and expressed in units of cm^{-1} is given as

$$I(q) = \frac{\partial\sigma}{\partial\Omega}(q) = K(\Delta\rho_n)^2\cdot P(q)\cdot S(q) + B_{inc}\,, \tag{3.5}$$

where $(\Delta\rho_n)^2$ is the square of the difference in neutron scattering length density, $P(q)$ is a function known as form factor, $S(q)$ is the (inter-particle) structure factor, q is the modulus of scattering vector and B_{inc} is the (isotropic) incoherent background scattering intensity.

Below we consider two types of systems which both play an important role in this work: Scattering from periodically arranged objects (Section 3.2) and scattering from disordered or weakly ordered objects in a uniform matrix (3.3).

3.2 Diffuse scattering from particulate systems

For a system of particles of uniform size and shape dispersed in a solvent or matrix the scattered intensity $I(q)$ can be expressed as

$$I(q) = \frac{\partial \sigma_{coh}}{\partial \Omega}(q) = \varphi(\Delta\rho_n)^2 \cdot VP(q) \cdot S(q) + B_{inc} \tag{3.6}$$

where φ is the volume fraction of the scattering particles, $\Delta\rho_n$ is the contrast between the particles and the matrix, V is the average volume of one particle, $P(q)$ is the *particle form factor* and $S(q)$ is the *inter-particle structure factor*, which relates to the arrangement of the scattering particles in the system. B_{inc} again denotes the incoherent scattering background.

For dilute samples (volume fraction φ no more than a few percent) and in the presence of long-range interactions between the particles, $S(q) \approx 1$ for the relevant q range and can omitted from eq. (3.6). In this regime and after subtraction of B_{inc}, equation 3.6 reduces to

$$I(q) = \varphi(\Delta\rho_n)^2 V \cdot P(q) \tag{3.7}$$

Eq. 3.7 can be used to determine the particle form factor and thus to obtain information about the particle size and shape. The form factor of particles of well-defined geometry can be calculated, as explained below.

Form factor of simple geometric objects

The form factor is a function that describes how $I(q)$ is modulated by interference effects between radiation scattered by different parts of the same scattering object. $P(q)$ is called the normalized particle form factor, because $P(q)$ reaches a limiting value 1 for $q \rightarrow 0$. $P(q)$ can be calculated by Fourier transforming the density functions of the desired particle shapes.

Spheres. For spheres of radius R, the form factor is given by

$$P(q,R) = 9\frac{(\sin(qR) - qR\cos(qR))^2}{(qR)^6} \tag{3.8}$$

Cylinders. The form factor of cylinders of radius R and infinite length is given by

$$P(q,R) = \frac{2j_0(q \cdot l \cdot \cos\alpha)J_1(q \cdot a\sin\alpha)}{q \cdot a\sin\alpha} \tag{3.9}$$

where $j_0(x) = \sin(x)/x$, $J_1(x)$ is the first order Bessel function. α is defined as the angle between the cylinder axis, R radius, l is rod half length, and the scattering vector, q. The normalized form factor $P(q)$ for spheres and cylinders are shown in Fig. 3.2. An important difference between the two is that the form factor of spheres becomes flat for $q \rightarrow 0$, while the form factor of cylinders decays as q^{-1} in arange of low q values. At higher q, both form factor curves exhibit a series of pronounced minima.

Guinier approximation

Generally, for dilute solution of non-interacting monodisperse particales in the limit of low q, the scattered intensity $I(q)$ is related to the radius of gyration R_g of the particle by the Guinier Approximation:

$$I(q) = I_0 \exp\left(-\frac{q^2R_g^2}{3}\right) \tag{3.10}$$

where I_0 is the zero angle scattering. According to eq. 3.10 R_g can be obtained from the slope of the plot $\ln(I(q))$ vs. q^2. The Guinier approximation is strictly valid only in the range in which $qR_g \leq 1$.

Porod scattering

In the transitional range at the high resolution end of the SAS pattern the only contribution to the scattering comes from the interface between the two phases and the intensity should drop with q^{-4} if this interface is smooth. This is a consequence of the fact that in this regime any

other structural features, e.g. interference between one surface of a particle and the one on the opposite side, are so random that they do not contribute. Thus in the range where $l \cdot q >> 1$, Porod's law is valid:

$$\lim_{q \to \infty} I(q) \propto A_S q^{-4} \tag{3.11}$$

where l is the reciprocal length. This allows the surface area A_S of the particles to be determined with SAXS. In the case of a fractally rough surface area with a dimensionality d between 2-3 Porod's law becomes:

$$\lim_{q \to \infty} I(q) \propto A_S' q^{-(6-d)} \tag{3.12}$$

Influence of the interparticle structure factor

The structure factor S(q) arises from the interference of the radiation scattered from different particles of the system and thus it reflects the correlation of the positions of the individual particles. Generally, S(q) is given by the relation

$$S(q) \propto \sum_i \sum_j e^{-\vec{q} \cdot (\vec{r}_i - \vec{r}_j)} \tag{3.13}$$

where r_i and r_j represent the positions of particles i and j of the N-particle system. For isotropic systems the exponential can be replaced by the function $\sin(x)/x$ with $x = q\Delta r$. For a dilute system, when $x << 1$, this reduces to $S = 1$. At higher concentrations of charged particles becomes the most probable distance. In this case S(q) will exhibit a peak at $q_m = 2\pi/d$. Theories of the structure factor are commonly based on the Ornstein-Zernike equation with closure relations appropriate for different interparticle interactions. For example, the Percus-Yevick closure relation is appropriate for hard-sphere particles, while the mean spherical approximation is used for particles interacting by long-range repulsive interactions.

Teubner-Strey model scattering function

In the present context we are interested in the arrangement of surfactant aggregates in the mesopores of a SBA-15 matrix. This case has some resemblance with the distribution of surfactant-coated oil droplets in a oil-in-water microemulsion. As was shown by Teubner and Strey [Teub87] the scattering of microemulsions can be described by a scattering intensity distribution

$$I(q) \propto \frac{1}{a_2 + c_1 q^2 + c_2 q^4} \tag{3.14}$$

where a_2, c_1 and c_2 are coefficients of the Landau free energy expansion. Eq. (3.14) yields a maximum in I(q) if $c_1 < 0$ and $4a_2c_2 - c_1 > 0$. In this case eq. (3.14) corresponds to a correlation function of the form

$$g(r) = \frac{\sin(kr)}{kr} e^{-r/\xi} \tag{3.15}$$

where $k = (2/d)$ is related to the length d that characterizes the quasi-periodic repeat distance, and ξ is the decay length of this quasi-periodic arrangement. The length d diverges if $4a_2c_2 - c_1 = 0$, and in this case eq. (3.14) reduces to the form

$$I(q) \propto \frac{I_0}{(1 + \xi^2 q^2)^2} \tag{3.16}$$

with $\xi^2 = \sqrt{(c_2 / a_2)}$, where I(q) is now a monotonic decaying function which represents the Fourier transformation of the simple exponential correlation function

$$g(r) = \exp(-r / \xi) \tag{3.17}$$

This exponential decay is the signature of a random distribution of "objects" and "holes" [Deb57] or, in the present context, patches of adsorbed surfactant and water. In a study of the structure of the adsorption layer of the surfactant C_8E_4 at a flat silica surface using grazing-incidence small-angle neutron scattering (GISANS) [Stei04] it was found that the I(q) would

be described by eq. (3.16) but it was speculated that a transition from a random distribution of surfactant patches to a quasi-periodic structure of surface aggregates at the surface may be induced by an increase of the amphiphilic strength (e.g. changing from C_8E_4 to $C_{12}E_5$) In this work we are studying the arrangement of surface aggregates of the surfactants $C_{10}E_5$ and $C_{12}E_5$ in the pores of SBA-15 using SANS. Results of this study are presented in Chapter 7.

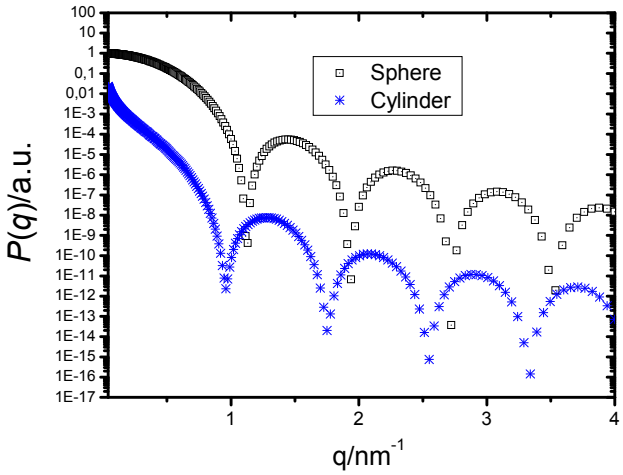

Fig. 3.2: Calculated form-factor curves for mono-disperse sphere (squares) and cylinder (blue crosses) of 4 nm radius.

3.3 Small-angle diffraction (SAD)

Crystals comprise a periodic arrangement of elementary cells and exhibit a high degree of long-range order. Incoming radiation is scattered at lattice planes and the scattered waves from two neighbouring lattice planes interfere constructively to produce a diffraction pattern which is specific for each crystal. This diffraction pattern comprises Bragg reflexes. For such systems with long-range order the Bragg condition is satisfied:

$$\lambda = 2d_{hkl} \cdot \sin \vartheta_{hkl} , \tag{3.18}$$

where n is the order of interference, d_{hkl} is spacing of the lattice planes characterized by the Miller indices hkl, ϑ_{hkl} is the glancing angle (one half of the scattering angle) [Atki94]. For a given wavelength and order of interference, each inter-planar spacing d_{hkl} determines a

glancing angle ϑ_{hkl}. Thus in diffractometry d_{hkl} can be experimentally obtained by measuring ϑ_{hkl}. By substituting the definition of scattering vector modulus q (equation 3.2) into Bragg condition (equation 3.7) we get the useful relation for a two dimensional lattice

$$q_{hk} = n \cdot \frac{2\pi}{d_{hk}}. \tag{3.19}$$

Through combined use of equations (3.2) and (3.8) we get the possibilities of configuring an instrument and easy determining the size of scattering bodies in a sample.

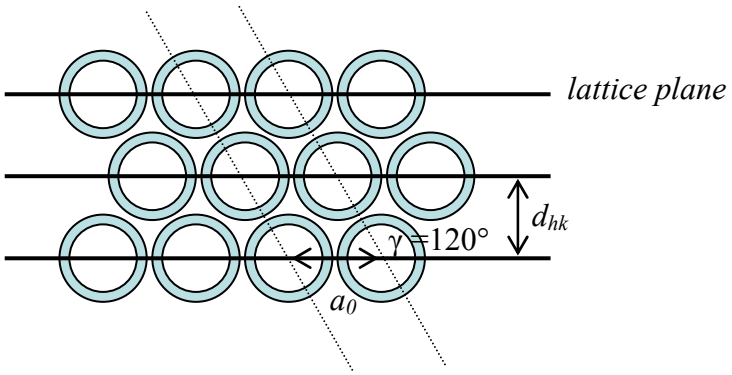

Fig. 3.3: Schematic presentation of a 2D hexagonal lattice, where d_{hk} is the spacings of lattice plane hk and a_0 is the lattice constant.

In the present work we are concerned with the periodic mesoporous silica SBA-15, which comprises arrays of cylindrical pores which are arranged parallel to each other in a 2D hexagonal symmetry (space group P6mm). Accordingly, we concentrate on a 2D hexagonal crystal lattice (Figure 3.3) in the following consideration.

For a close-packed 2D hexagonal array of lattice constant a_0 the positions of Bragg peaks can be then given by

$$q_{hk} = q_{10}\sqrt{h^2 + k^2 + hk} = \frac{4\pi}{a_0\sqrt{3}}\sqrt{h^2 + k^2 + hk} \tag{3.20}$$

The positions of the leading Bragg reflexions of a 2D hexagonal crystal are indicated in Figure 3.4.

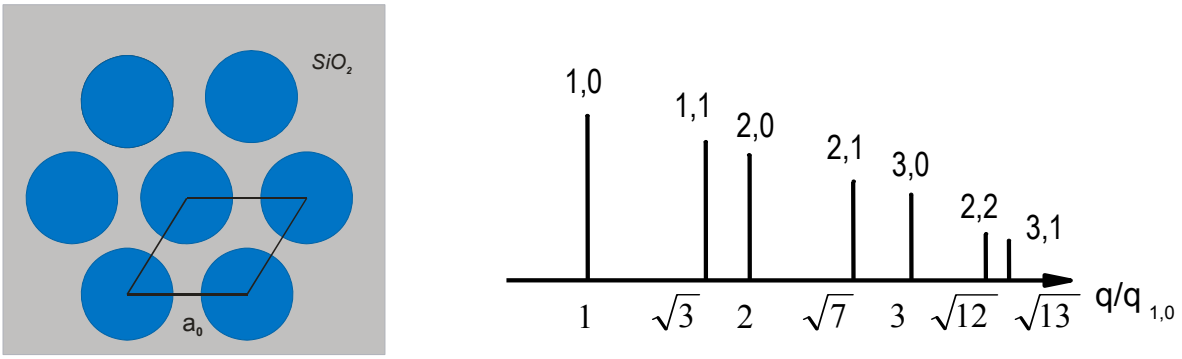

SBA-15 as a 2D hexagonal crystal

Fig. 3.4: Schematic presentation of 2D hexagonal crystal lattice and Bragg reflexes at characteristic values of q.

The small-angle scattering intensity of a SBA-15 powder sample is given by eq. 3.5. The structure factor $S(q)$ of SBA-15 materials can usually be represented by a sum of Gauss, Lorenz or pseudo Voigt functions [Förs05]. The structure factor $S(q)$ of an ideal undistorted lattice can be written as

$$S(q) \propto \frac{1}{q^2} \sum_{(hk)} m_{hk} L_{hk}(q) , \tag{3.21}$$

where the line-shape function L_{hk} can further be expressed as

$$L_{hk}(x) = (2/\pi\delta)\exp(-4x^2/\pi\delta^2) . \tag{3.22}$$

Since SBA-15 represents arrays of cylindrical pores, the form factor to be used in eq. (3.5) is the form factor of a cylinder (eq. 3.9) or of a core-shell cylinder. We return to this point in Chapter 6.

3.4 Method of contrast variation

The fact that neutrons do not interact with the electron cloud but with the atomic nuclei allows a fascinating possibility to neutron scattering experiments: the strength of neutron-nucleus interaction varies irregularly with the atomic number Z. Furthermore, different isotopes of a given element have different neutron scattering cross sections.

Thus on the basis of the relation $I(q) \propto (\Delta\rho_n)^2 \cdot S(q) \cdot P(q)$ the scattering intensity can be modulated by varying scattering length densities of sample constituents (here A and B in case of two-phase-systems), where $(\Delta\rho_n)^2 = (\rho_{n,A} - \rho_{n,B})^2$ is the contrast factor.

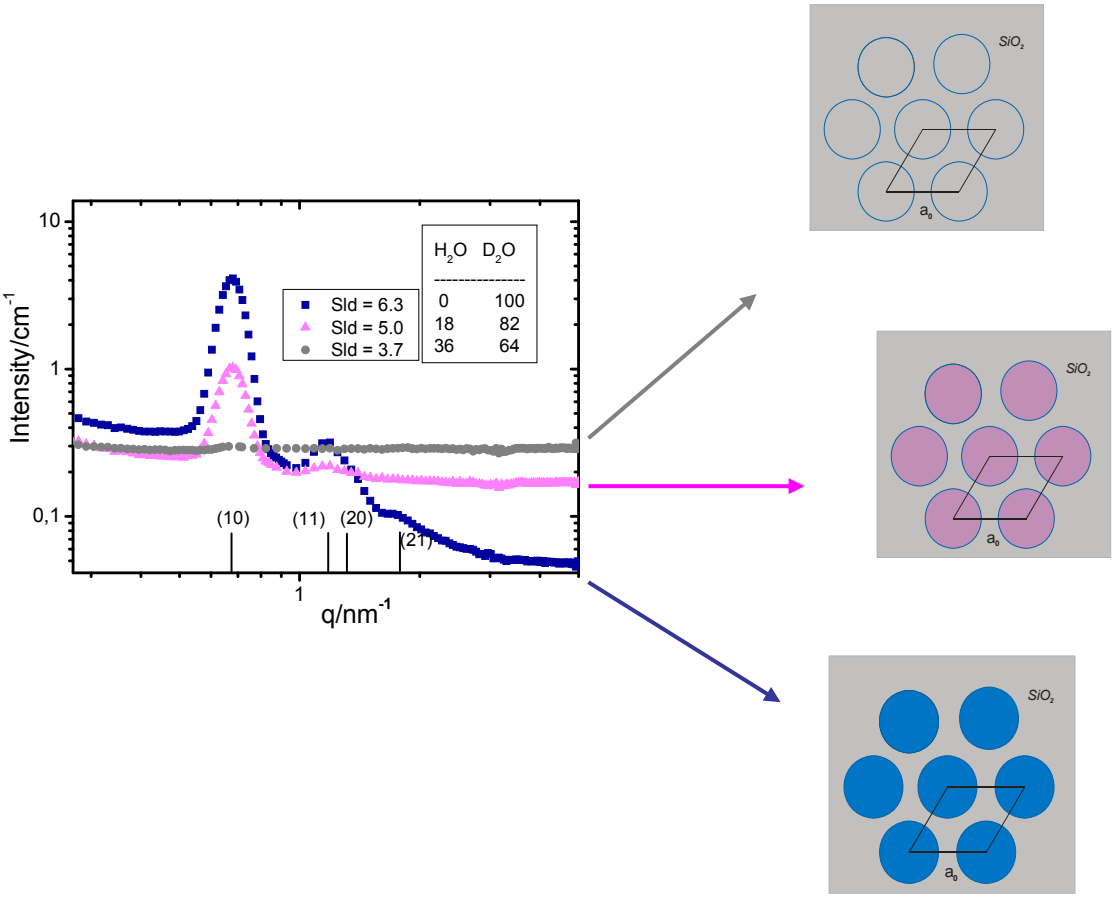

Fig. 3.5: SANS curves of SBA-15 immersed in H_2O/D_2O mixtures of different scattering length densities (SLD). The inset in the graph gives the weight fraction of light and heavy water for each SLD of the liquid. The positions of Bragg peaks arising from the pore lattice are marked with vertical lines and indices.

In the case of a SBA-15 powder sample immersed in a liquid (i.e., a typical two-phase-system), this can be done by mixing appropriate amounts of heavy and light water to get the required scattering length density ρ_n according to the relation:

$$\overline{\rho}_{n,Mixture} = \rho_{n,H_2O}\phi_{H_2O} + \rho_{n,D_2O}\phi_{D_2O} \tag{3.23}$$

where the symbols ϕ represent the volume fraction of H_2O and D_2O respectively. By choosing appropriate volume fractions of H_2O and D_2O the liquid can possess the same scattering length density as the silica matrix, so that $(\Delta\rho_n)^2$ will be zero (contrast matching).

The contrast-matching method is a very useful technique if a certain part of a polymer aggregate (for example, the shell of a block copolymer micelle) is to be quenched using solvent of appropriate scattering length density. For the purpose of the present structural study on surfactant aggregates in the pores of SBA-15 silica, an appropriate mixture of H_2O and D_2O was chosen to make the silica matrix "invisible" for neutron (see Chapter 4).

As shown in Fig. 3.5, the *(10)* Bragg peak of the pore lattice is very pronounced when the sample is immersed in pure D_2O (when $\Delta\rho_n = 2.6\cdot10^{10}cm^{-2}$) but much weaker in a H_2O/D_2O mixture of 18 wt-% H_2O (when $\Delta\rho_n = 1.3\cdot10^{10}cm^{-2}$). When the sample is immersed in a contrast-matching H_2O/D_2O mixture ($\Delta\rho_n = 0$) the Bragg peak is completely purged and only a constant background remains which is primarily due to the incoherent scattering of protons.

When surfactant is adsorbed into the cylindrical pores of SBA-15 from a contrast-matching H_2O/D_2O mixture, the dispersion will represent a two-phase system, and scattering will arise from the surfactant against a uniform scattering background of silica matrix and solvent. As the pores are now containing surfactant, either adsorbed at the walls or dispersed in the core, the contrast match condition is no longer met and the Bragg reflections will reappear, although the intensity ratio of the leading peaks will be modified by the way in which the surfactant is arranged in the pores. This will be discussed in Chapters 6 and 7.

4. Experimental

This chapter deals with the details of experiments such as experimental setups of SANS/SAND instruments, used materials, sample preparation and characterisation of SBA-15 sample. Introduced will be also two types of sample cells which were specially designed and manufactured for each neutron scattering instrument.

4.1 Materials

Silica materials

SBA-15 silica materials for present work were synthesized in our laboratory according to the method of Zhao *et al*., using a technical-grade poly(ethylene oxide)-poly(propylene oxide)-poly(ethylene oxide) triblock copolymer (Pluronic P103, BASF) as the structure-directing agent in aqueous H_2SO_4 solution, and tetraethyl orthosilicate (TEOS) as the silicate precursor [Zhao98-1].

The calcined SBA-15 samples were characterized using nitrogen adsorption and SAXS. The resulting properties derived by these methods are given in Table 4.1. The specific surface area a_s is obtained from nitrogen sorption isotherms of the porous solid (Gemini III 2375 Volumetric Surface Analyzer and Quantachrome Autosorb Automated Gas Sorption System) and calculated according to the theory of **B**runauer, **E**mmet and **T**eller (BET), in which the amount of the gas necessary for the formation of a complete monolayer at the surface can be determined. In gas-volumetric measurements this amount is often expressed by the respective gas volume V_{mono} under standard conditions (STP). By measuring the amount of adsorbed gas V_{ads} as a function of relative pressure p/p_0 sorption curves are obtained which can be described by the BET equation. After linearization the BET equation has the form

$$\frac{p/p_0}{V_{ads}(1-p/p_0)} = \frac{1}{V_{mono}\cdot C} + \frac{C-1}{C\cdot V_{mono}}\cdot\frac{p}{p_0} \qquad (4.1)$$

where C is the scalar BET constant which depends on the isotherm shape and characterizes the strength of the interaction between the gas molecules and the solid surface. The BET specific area a_s is calculated from V_{mono} according to the formula

$$a_s = V_{mono} \cdot \sigma(N_2) \cdot N_A \qquad (4.2)$$

where N_A is the Avogadro constant, and $\sigma(N_2)$ is the molecular cross-sectional area of N_2 in m^2/molecule occupied by each adsorbed molecule in a complete monolayer.

The pore width of the cylindrical mesopores was determined by the improved *KJS* method [Jaro06], which relates the pore diameter D to the pore condensation pressure $(p/p_0)_{pc}$ by

$$D = -1.15/[\log(0.875(p/p_0)_{pc})] + 0.2[60.65/(0.03 - \log((p/p_0)_{pc}))]^{0.397} + 0.27 \qquad (4.3)$$

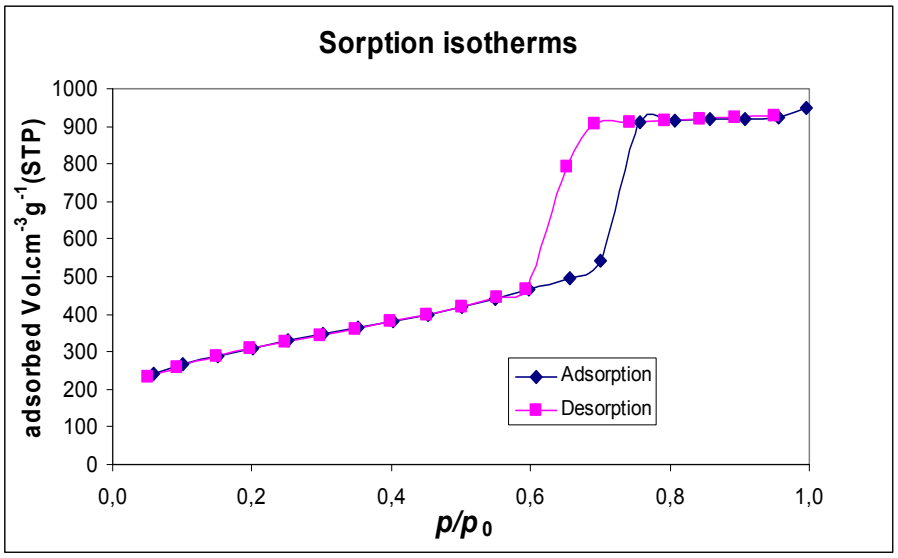

Fig.4.1 Sorption isotherms of a SBA-15 sample (D16 - 847) used in the present work.

SBA-15 powder grains are in the shape of curved cylinders. They are typically 200 - 400 nm in diameter and 1 - 3 μm long. While the SBA-15 materials comprise 2 dimensionally hexagonally close-packed unit cells of cylindrical mesopores, the walls of these materials are amorphous in atomic level. For present work SBA-15 materials of almost identical pore diameter (about 8 nm) were used. Typical scanning electron microscope images are shown in Figure 4.2.

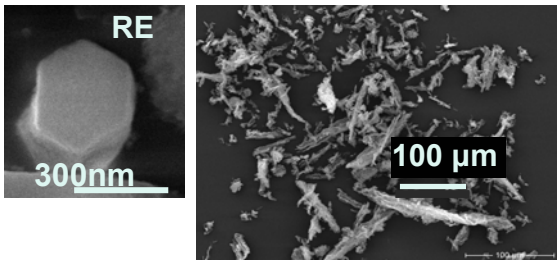

Figure 4.2: TEM images of typical SBA-15 powder (left: single particle, right: powder grains)

Sample	v_p / $cm^3\ g^{-1}$	a_s / $m^2\ g^{-1}$	p/p_0	*D(iKJS)* / nm	a_0 / nm
D16 - 129	**1.052**	**814**	**0.7287**	**8.23**	**10.51**
D16 - 847	*	1096	0.7196	8.04	10.69
V4 - 1091	1.000	801	0.7243	8.14	10.70
V4 - 1011	1.362	968	0.7610	8.96	10.46
	1.036	882	0.7350	8.36	10.98
V4 - 0935	1.235	905	*	8.80	*
V4 - 1140	1.160	872	0.7453	8.60	*

Table 4.1: Properties of SBA-15 materials : v_p specific pore volume, a_s specific surface area, p/p_0 pore condensation pressure, *D(iKJS)*[Jaro06] pore diameter from improved KJS method and a_0 lattice constant. The samples were named after the name of instrument (D16 at ILL or V4 at HZB, respectively) combined with the number of granted project at corresponding instrument.

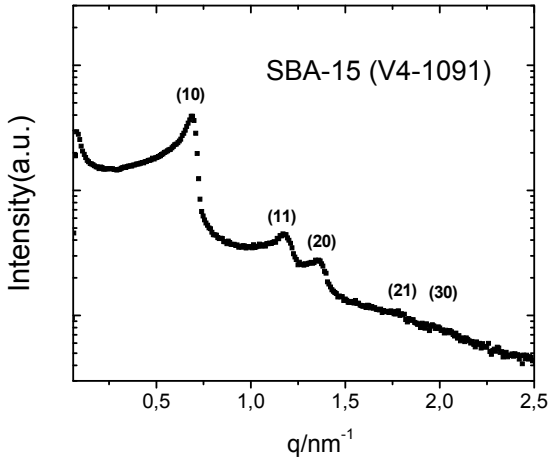

Fig. 4.3 SAXS(Kratky Camera) spectrum of a SBA-15 sample used in this work (V4-1091).

Surfactants

C_nG_m : The sugar-based surfactants decyl-*β*-D-glucoside ($C_{10}G_1$, purity > 99%), decyl-*β*-D-maltoside ($C_{10}G_2$, purity > 99.5%), and dodecyl-*β*-D-glucoside ($C_{12}G_1$, purity > 99%), were obtained from GLYCON Bioch. GmbH. Biotechnology and were used as received.

C_nE_m : The pentaethyleneglycol monodecyl ether ($C_{10}E_5$, purity > 97%) and pentaethyleneglycol monododecyl ether ($C_{12}E_5$, purity > 98%) were purchased from BACHEM and Fluka (Sigma-Aldrich).

C_nPCl : Dodecylpyridinium chloride (DPCl, purity 98%) and hexadecylpyridinium chloride (CPCl, purity 99%) were obtained from Sigma-Aldrich and used without further purification.

Other chemicals

Pro-analysis quality KCl was received from Merck. D_2O (99.9 % isotope purity) was received from Sigma-Aldrich and euriso-top®. High purity water (H_2O) was obtained from a Milli-Q pure-water system.

4.2 Sample preparation

To study the assembly of surfactants in the pores of SBA-15 by small-angle neutron scattering (SANS), samples of known amount of surfactant per unit area of the pore walls had to be prepared. Details of preparation procedure are presented in this section. In the initial stage of our investigation, two types of samples were prepared with respect to surfactant amount: so-called mixing-type and washing-type samples [Qiao03]. In “mixing-type” samples (Experiment series CHE 1011 and CHE 1091) surfactant loadings corresponding to the plateau value of the adsorption isotherm in SBA-15 were chosen (surface concentration Γ_{max}). Lower surfactant loadings were then reached by subsequent equilibration with known amounts of contrast-matching H_2O/D_2O solvent (“washing-type” samples). In later SANS experiments, in order to prepare the amount of surfactant in the sample in a controlled way, three surfactant loadings were then defined, which correspond to surface concentrations Γ_{max}, 2/3 Γ_{max}, and 1/3

Γ_{max}. Finally, a greater number of samples with more refined steps of 0.15 Γ_{max} were used. This enables the observation of small changes in scattering intensities with respect to the evolution of aggregate structures in the pores, especially at their earlier stage of building (Experiment 9-12-129 at D16, ILL).

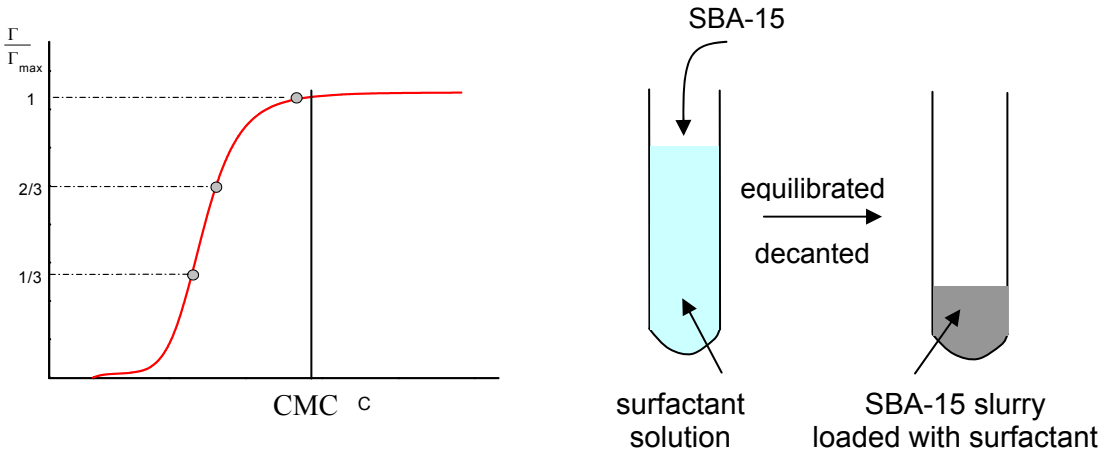

Figure 4.4: Schematic presentation of general sample preparation procedure. For cationic surfactant the pH must be adjusted additionally during equilibration process.

Sample preparation procedures can be classified with respect to following parameters:

1. Degree of fractional pore filling (amount of adsorbed surfactant)
2. Variation of contrast using D_2O for surfactant aqueous solution[2]
3. Electrolyte concentration (in case of cationic surfactant)

Nonionic surfactants

To prepare samples of SBA-15 loaded with well-defined amounts of non-ionic surfactant, the corresponding amount of surfactant $n = n_{pore} + n_{ce}$ was dissolved in water and the solution was then contacted with a known mass of silica powder (ca. 0.1 g). Here n_{pore} is the amount of

[2] The scattering length density (SLD) of pure D_2O is 6.34×10^{-10} cm^{-2} and SLD of pure H_2O is -0.56×10^{-10} cm^{-2}. By mixing SLD of D_2O and H_2O we can obtain contrast-matching water (SLD = 3.7×10^{-10} cm^{-2} : 63.9 wt.% of D_2O and 36.1 wt.% of H_2O) and water mixture of intermediate SLD = 5.0×10^{-10} cm^{-2} : 81.9 wt.% of D_2O and 18.1 wt.% of H_2O

surfactant adsorbed in the pores and n_{ce} is the equilibrium concentration of the surfactant in solution for given condition. The part n_{pore} is obtained by multiplying the surface surfactant concentration Γ with specific surface a_s (m^2/g) and the amount of added silica powder in gram, i.e. $n_{pore} = \Gamma \cdot a_s \cdot m_s$.

The amount of surfactant in solution is $n_{ce} = V \cdot c_e$, where V is the volume of solution (typically 10 ml) and c_e is the equilibrium concentration of the surfactant, which is similar to the CMC. n_{ce} is small because of the low CMC value, such that various loadings of samples have been produced at almost the same concentration of the supernatant solution. After sonification for several minutes and 2 hours of equilibration on the rotating cylinder, the prepared samples are conserved in the small glass bottle for scattering experiment.

Directly before the scattering experiment the supernatant was decanted from the suspension, where the surfactant-adsorbed silica particles have been already sedimented.

Cationic surfactants

Because the silica surface in aqueous solution shows a strong pH-dependency of surface charge it is necessary to ensure a well-defined pH of the silica suspension especially for ionic surfactants. On adsorption the pH values may also change. For the cationic surfactants a suspension of 0.12 g SBA-15 was prepared in aqueous KCl solutions of required concentration (0.1 or 0.001 M), then the pH was adjusted to 9 with appropriate amount NaOH solution and occasionally also with HCl, when more NaOH solution was added than required to get pH 9. After primary adjusting of pH the estimated amount of surfactant was added and the pH value which was lowered by H^+ due to surfactant adsorption was again corrected to 9. Analogous to non-ionic surfactant the samples were then treated in ultrasonic bath and equilibrated.

4.3 Small-angle scattering measurements

4.3.1 SAXS - Kratky Camera

SAXS measurements were performed to determine the lattice constant a_0 of the SBA-15 materials (Table 4.1). Kratky Camera, as a typical laboratory SAXS instrument, is distinguished by its slit collimation system which delivers a line shaped X-ray beam from an X-ray tube source perpendicular to the detector-source axis. Thus scattering curves are smeared in a different way than those measured by scattering instruments with point collimation due to this collimation geometry.

PSD (Position Sensitive Detector, M-Braun 50m): Using ionizing methane-argon gas mixture (usually 90% argon, 10% methane, "P10") the scattered X-ray photons ionize these gas molecules in the vicinity of a platinum detector wire of about 60 µm thickness. The argon is ionized by incoming X-ray photons, and the electric field multiplies this charge into a measurable pulse. The methane suppresses the formation of fluorescent photons caused by recombination of the argon ions with stray electrons. The positions of detected ions on the wire are registered using appropriate electronics.

For SAXS measurement with the Kratky camera, a small amount of mesoporous silica powder was transferred into a Mark tube, i.e. a capillary tube of about 1mm outer diameter and brought into a sample holder of Kratky Camera specially designed for strongly scattering samples. This sample holder is equipped with a defined small slit to characterize structural properties such as center-to-center distance of the pore or grade of order. The camera housing was evacuated to minimize the background scattering by air molecules. The X-ray diffractogram shows typically 5 well-separated peaks which can be indexed according to a 2D hexagonal lattice.

4.3.2 SANS

Experimental setup

Small-angle neutron scattering (SANS) and small-angle neutron diffraction (SAND) experiments were done at Instrument V4 (a Pin-Hole SANS instrument, Figure 4.5) of the Helmholz-Center Berlin (formerly Berlin Neutron Scattering Center of Hahn Meitner Institut, Berlin, Germany) and at Instrument D16 (a two-circle small-momentum transfer diffractometer/SANS, see Figure 4.6) of the Institute Laue-Langevin (Grenoble, France).

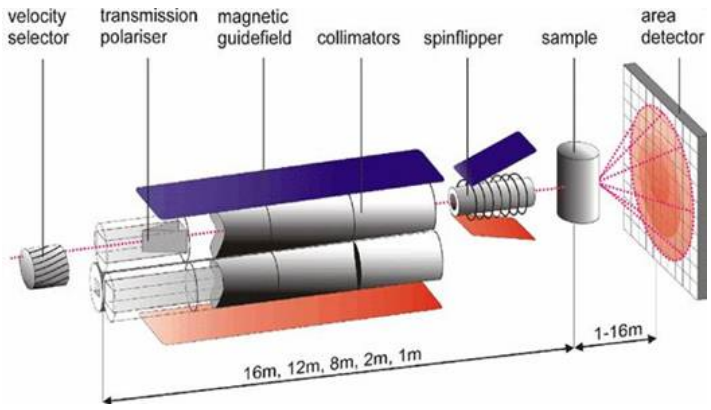

Fig. 4.5: Experimental setup of SANS instrument V4 at the Helmholz-Center Berlin. This instrument covers a q-range from 10^{-2} nm^{-1} to 8.5 nm^{-1}, allowing density composition and magnetization fluctuations in materials to be measured on a length scale from 0.5 nm to 400 nm. (http://www.hmi.de/bensc/instrumentation/instrumente/v4/v4-pic.html)

The main physical difference between the two instruments from the point of view of the present work is the different grade of instrumental smearing due to instrument architecture, wavelength resolution and collimation. Due to higher neutron flux of the ILL reactor, shorter measuring times per sample than V4 were possible at D16. The V4 instrument has a two-dimensional ^3He-detector of 64×64 cm^2 (5×5 mm^2 pixel size), which is equipped with new read-out electronics for 128×128 cells. D16 instrument is equipped with 256×256 mm^2 (2×2 mm^2 pixel size) ^3He-detector.

At V4 instrument, neutrons of wavelength $\lambda = 0.605$ nm (at 21000 rpm of mechanical velocity selector) with a wavelength distribution $\Delta\lambda/\lambda = 0.12$ (FWHM) and sample-to-detector distances of 1, 4, and 12 m were used to cover a range of scattering vectors q from 0.05 to 5 nm^{-1}. Additionally the detector plate can be elevated vertically for about 30 cm at 1 m position, which allows much larger q-range without losing good statistics in the case of strong scattering samples. The efficiency of single detector cells will be considered in the data reduction process by normalization on the intensity of H_2O.

The D16 instrument of ILL (instrumental setup of D16 is shown schematically in Figure 4.6) offers high intensity neutron flux and very small wavelength resolution of $\Delta\lambda/\lambda \leq 0.01$, which allows us to solve leading Bragg reflections of SBA-15 matrix even in a contrast matching H_2O/D_2O solvent mixture when surfactants are adsorbed on the pore wall. In terms of q-space

and *q*-resolution, D16 nicely fills the gap between the small angle instruments and classical diffractometers.

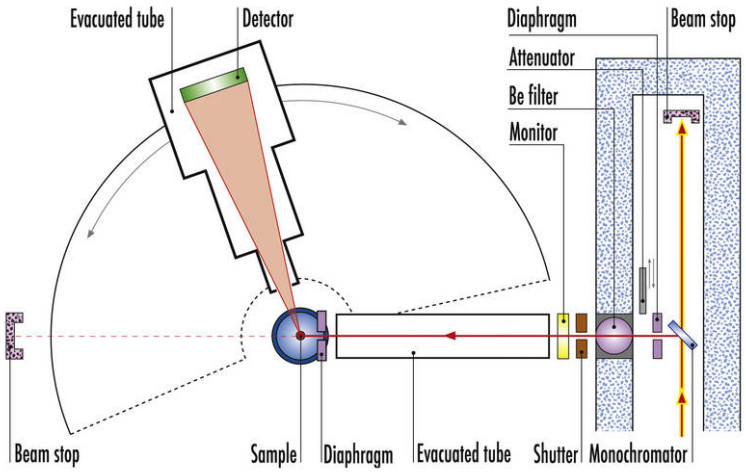

Fig.4.6: A schematic view (a bird's eye view) of D16 small-momentum-transfer diffractometer/SANS setup. (http://www.ill.eu/instruments-support/instruments-groups/instruments/d16/)

The primary white beam is reflected by a focussing pyrolytic graphite monochromator providing an important flux at the sample. The monochromator housing has two beam holes at take-off angles of 90° and 115°, corresponding to 4.7 Å and 5.6 Å beams and incorporates the slit systems. For our experiments the take-off angle of 90° was chosen, i.e. the neutron wavelength was 4.7 Å.

4.3.3 SANS Sample cells

Two types of specially designed aluminium sample cells were manufactured in the mechanical workshop of the Institue of Chemistry, to be used at Instrument V4 (rotating drum changer) and at Instrument D16 (linearly moving changer, see picture in Fig. 4.7) to fit the sample changer specification of the respective instrument. The width of the space between the two quartz glass windows, where the sample is placed, is determined by an aluminium ring of 1 mm thickness. This aluminium ring has an inner diameter of 11 mm, so that the volume

between the glass windows confined by the aluminium ring is 0.1 cm^3. This construction of the sample cell allows reproducible amounts of the silica sample to be placed into the cell and to be exposed to the neutron beam. The cells are sealed by O-rings to protect slurry samples from drying by evaporation of water. The cells filled with surfactant-loaded SBA-15 slurry samples were proved to be sufficiently protected against losing water in the samples during the measurement time. Photographs and technical drawings for these cells are shown in Fig.4.8 and 4.9.

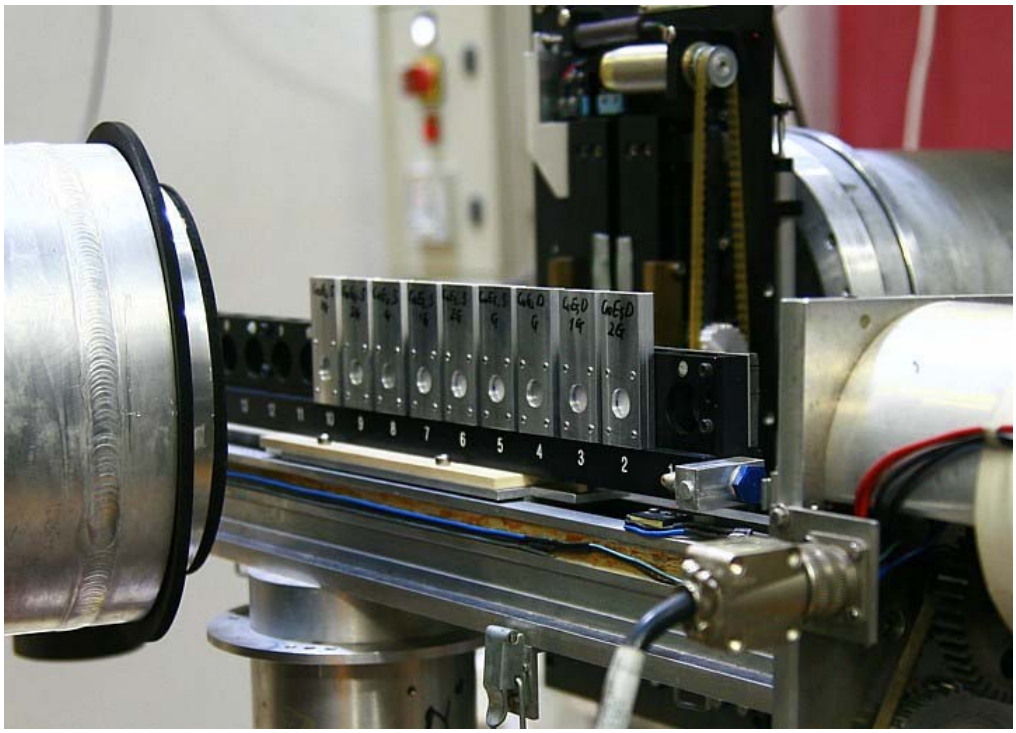

Fig.4.7: The linear sample changer of instrument D16 of ILL assembled with aluminium sample cells designed for the present measurements. The neutrons scattered by the sample are registered by a detector on the left side. Sample cells are exposed to ambient environment.

At the V4 instrument the required area of sample can be selectively exposed to neutron beam by placing cadmium beam stopper with a circular hole (1 cm in diameter) in front of the sample cell and thus defined sample volume can also be realised.

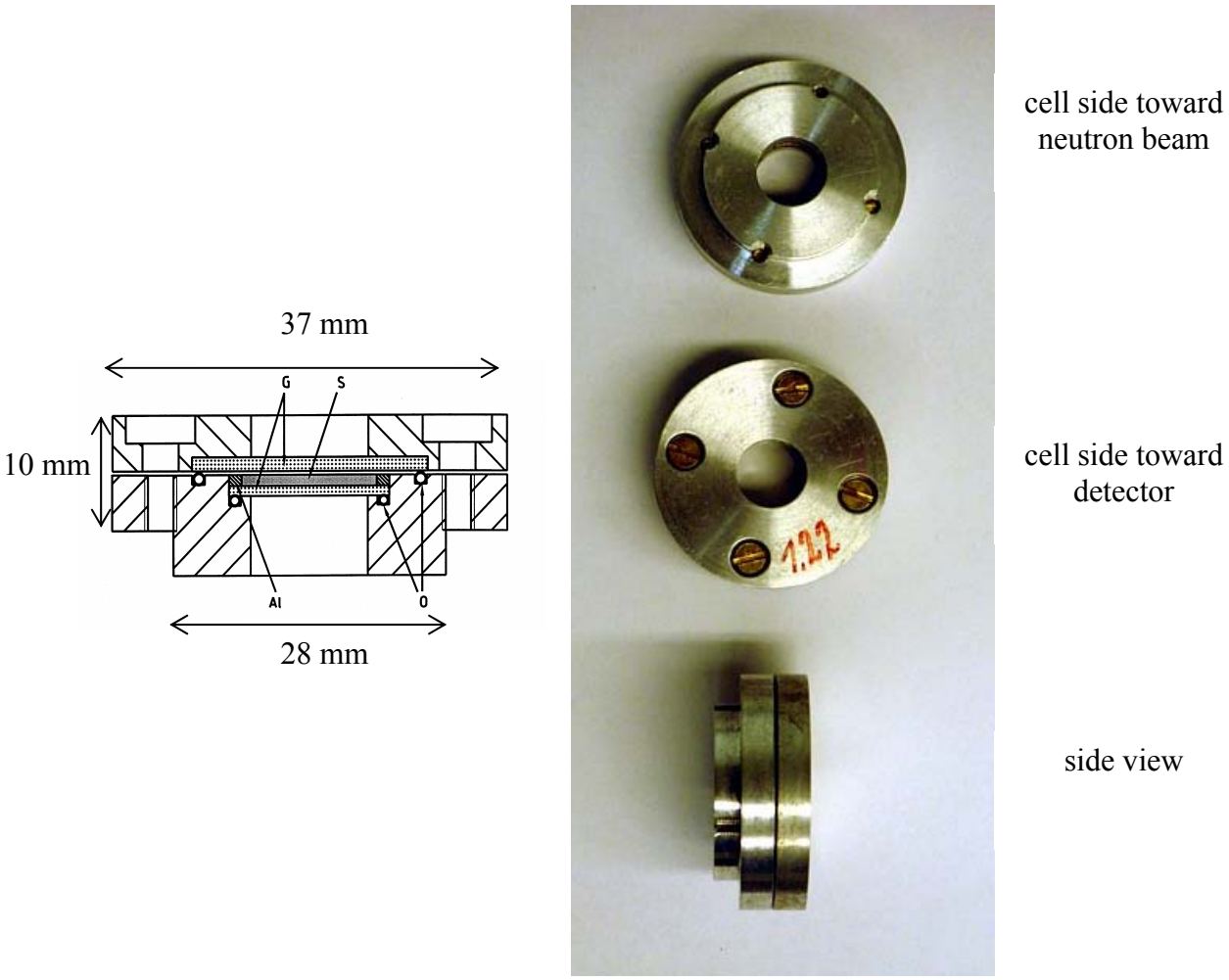

Fig.4.8: Cross-sectional drawing (left) and photograph (right) of sample cells designed for V4. After filling the sample, the cell is placed in an adapter which in turn is placed into drum sample changer in a chamber. In the drawing: S: sample, O: O-rings, Al: aluminium ring of 13mm outer 11mm inner diameter and 1mm thickness, G: quartz glass windows of 1.2mm and 0.9mm thickness.

As the center of the adapter holder coincides with that of the adapter, and since the sample cell in turn is well centered in the sample cell adapter, the sample positions are well defined. Thus by using the adapters placed on the drum sample changer the positions of sample cells are then applied for the setting parameters of the V4 instrument.

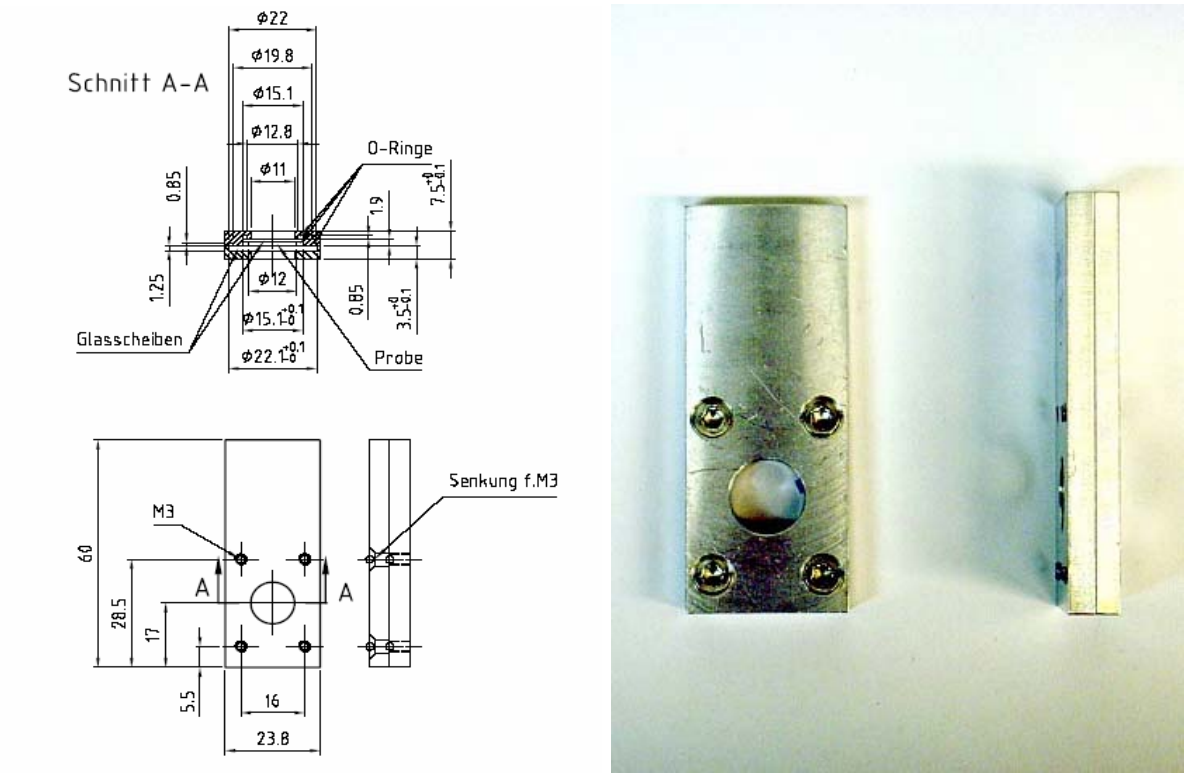

Fig.4.9: Technical drawing (left) and photograph (right) of sample cell designed for D16.

4.3.4 Supplementary measurement and data reduction

The SANS experiments require a series of additional measurements, which are necessary for the correction and data reduction process. These supplementary measurements include defining the beam center, the determination of the detector sensitivity, and of the transmission of each sample.

Beam center and beam stopper: The first step of the data reduction process is defining the center of the incoming neutron beam on the detector. For the conversion of the two-dimensional intensity distribution into q-dependent scattering intensity, it is necessary to know the mid-point of neutron beam on the detector (the beam center). To determine the beam center, an attenuator is brought in the beam instead of the beam stop which is normally placed directly in front of detector to protect the detector from the primary neutron beam. The center of radial intensity distribution will be defined in a symmetrical square around the geometrical detector center by choosing a mid-point, such that the integral intensity around this point becomes the

largest one. The position and size of beam stopper should be adjusted in such a way, that the primary beam can be fully covered. If it is not the case, the overexposed detector cells on the boundary of the beam stopper can be manually marked out with the help of data reduction software (so called 'mask').

Transmission: When the incoming neutron flux goes through a sample the intensity becomes weaker due to absorption and incoherent scattering. The measure for this intensity reduction is sample specific, so that it must be measured for all samples before or immediately after the scattering measurement. The sample transmission is defined as the ratio between the scattering intensity of sample $I_{SAMPLE}(i,j)$ to the intensity of beam itself, named as $I_{EH}(i,j)$:

$$Tr_{def} = \frac{I_{SAMPLE}(i,j)}{I_{EH}(i,j)}$$

Here, i and j refer to the detector cells. Because $I_{SAMPLE}(i,j)$ includes the transmission of sample holder too, the transmission of sample itself can practically be obtained as the ratio of the $\boldsymbol{Tr_{def}}$ values with and without sample.

Detector sensitivity/Normalisation: The individual cells of the ^3He-detector exhibit different sensitivities with regard to neutron detection. Therefore, it is required to calibrate the relative efficiency of detector cells. For this purpose, samples that scatter almost angle-independently in the small-angle region, like H_2O or vanadium, are used. At V4 and D16 instruments, sensitivity of the detector cells is determined by employing H_2O as the sample liquid. Because the scattering cross section of H_2O is well known, we consequently obtain an absolute scattering intensity ($I(q)/cm^{-1}$) through the normalization.

Data reduction: Because each detector cell simply counts and registers arriving scattered neutrons on it, the two-dimensional raw data of detector units should be converted to an understandable scattering curve by using appropriate data reduction software such as BERSANS (V4, Helmholz Zentrum Berlin) or RED16 (D16, ILL). After detector dead-time (τ) correction, the registered scattering intensity on the detector cell (i,j) can further be corrected according to the formula

$$I_{SAMPLE}(i,j) = \frac{(I_{SAMPLE}(i,j) - Cd(i,j))}{Tr_{SAMPLE}} - \frac{(I_{EC}(i,j) - Cd(i,j))}{Tr_{EC}} \cdot \frac{1}{A},$$

where *Cd(i,j)* is ambient background signal, *EC* stands for *Empty Cell*, and *A* is scaling factor. For the samples, the scaling factor *A* is practically the volume illuminated by neutron beam. To obtain the scaling factor of water for V4 instrument, an additional calculation is necessary:

$$A_{H_2O} = \frac{\frac{\pi}{4} D^2 \cdot \left(1 - \frac{Tr_{WATER}}{Tr_{EC}}\right)}{4\pi \cdot Tr_{WATER}},$$

where *D* is the diameter of illuminated cross section for water.

After normalization by $I_{WATER}(i,j)$, we get the scattering intensity $I_{NOR}(i,j)$ expressed in absolute units [cm^{-1}]:

$$I_{NOR}(i,j) = \frac{I_{SAMPLE}(i,j)}{I_{WATER}(i,j)}$$

The normalized scattering intensities $I_{NOR}(i,j)$ are then radially averaged around the beam center in dependency of radius and consequently be converted to a one dimensional, angle-dependent intensity distribution of *I*(q).

Determination of contrast matching point for mesoporous silica

As outlined in Section 3.3, SANS studies can yield valuable information when the samples are measured at different scattering contrasts. In the present work it is particularly useful to study the scattering resulting from the surfactant in the pores in a solvent that matches the scattering length density of the silica matrix of SBA-15.

Prior to the SANS studies with surfactants, the contrast-match point of SBA-15 with a H_2O/D_2O mixture was determined by measuring scattering curves of SBA-15 in a series of H_2O/D_2O mixtures of different D_2O weight fraction Φ_{D_2O}, i.e., different scattering length densities (SLD) of the solvent. An enlarged section of the scattering curves in the *q*-range of the *(10)* Bragg peak (q_{10} = 0.67 nm^{-1}) for H_2O/D_2O mixtures of SLD from 3.2 to 3.6· 10^{10} cm^{-2}

is shown in Fig. 4.4a. As explained in section 3.1 the overall intensity represents a sum of incoherent scattering (I_{inc}), which is essentially independent of q but increases with the volume fraction of H_2O in the solvent mixture, and Bragg-scattering which in the vicinity of the *(10)* Bragg peak is proportional to the scattering contrast $(\Delta\rho_n)^2$, where $\Delta\rho_n$ = SLD(matrix) – SLD(water):

$$I(q_{10}) = I_{inc} + C(\Delta\rho_n)^2$$

Accordingly, the intensity increment $I(q_{10}) - I_{inc} \equiv I_{10}$ is expected to be a quadratic function of $\Delta\rho$, and thus a plot of $\sqrt{I_{10}}$ vs. the weight fraction Φ_{D_2O} should be linear. This is indeed found for the present systems, as shown in Fig. 4.4b. Extrapolation of a $I^{1/2}$ vs. the weight fraction of D_2O (Φ_{D_2O}) plot delivers the zero contrast point at a weight fraction of 0.638, which corresponds to a scattering density of $3.7 \cdot 10^{10}$ cm^{-2}. This is $0.2 \cdot 10^{10}$ cm^{-2} larger than the theoretical SLD for SBA-15 silica matrix of $3.5 \cdot 10^{10}$ cm^{-2} calculated[3] by using density of 2.2 g/cm^{-3} for SiO_2.

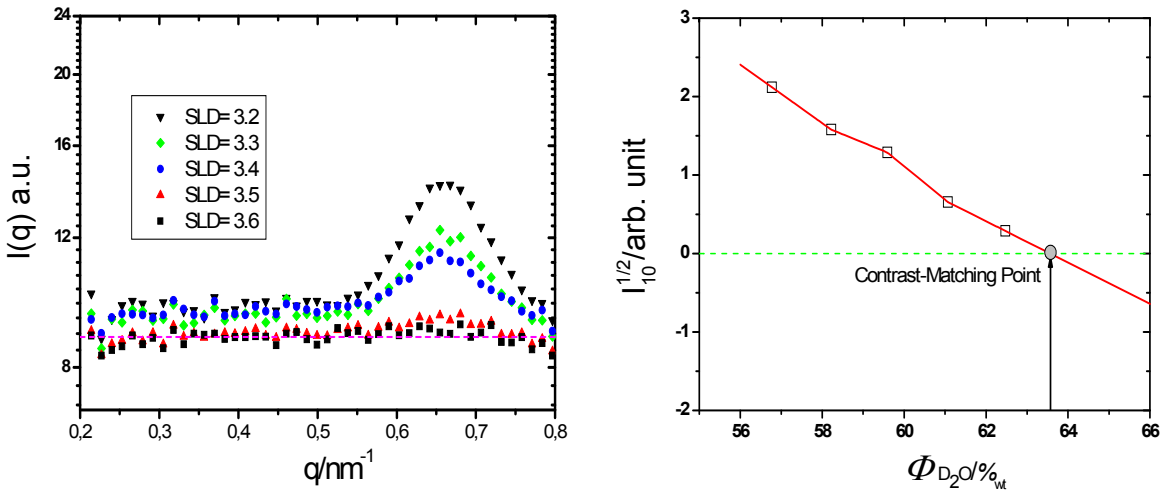

Fig. 4.4 Scattering curves of SBA-15 in H_2O/D_2O mixtures of various scattering length densities around theoretical SLD of $SiO_2 = 3.5 \cdot 10^{10}$ cm^{-2}. The square root values of the *(10)* Bragg peak intensity (incoherent background subtracted) were plotted and extrapolated.

Further, an experimental scattering length density determination of a commercial colloidal silica beads of type Bindzil B30 shows a value of $3.5 \cdot 10^{10}$ cm^{-2} [Des03], where for another commercial silica beads Ludox and for non-commercial synthesized silica beads, the same matching point of $3.5 \cdot 10^{10}$ cm^{-2} was obtained [Lugo09]. The somewhat higher value of the

[3] Calculated by scattering length density calculator at http://www.ncnr.nist.gov/resources/sldcalc.html

SLD of SBA-15 silica might be due to some preferential adsorption of D_2O in the pores. However, the deviation from the expected SLD is very small and might be caused by some artefact.

The contrast-matching point of SBA-15 silica was verified in succeeding experiments at V4 instrument of HMI Berlin as well as at D16 instrument of ILL Grenoble by measuring scattering intensity of SBA-15 immersed in H_2O/D_2O mixtures which possess neutron scattering densities around the empirical matching point of $3.7 \cdot 10^{10}\,cm^{-2}$.

For mixing water and heavy water their amount was calculated and weighed in mass to prepare the required scattering length densities more precisely than in volume.

4.4 Thermogravimetric Analysis

This analytical technique can be used to determine the thermal stability of a material and its fraction of volatile or combustible components by monitoring the weight change that occurs as a specimen is heated in an inert atmosphere or in air. TGA is commonly employed in research and testing to study the thermal characteristics of materials such as degradation temperatures, absorbed moisture content and the level of organic components in inorganic materials.

In a TG curve the change of sample weight is plotted as a fuction of temperature or time at a given heating rate. Commonly the ratio between sample weight at given temperature and initial weight is plotted, where TG is usually given in percent. In the present work, TG values are labeled by the character "m_x" with subindex x for the associated temperature T_x, at which significant changes in the TG profile occur. To increase the sensitivity of the method, the derivative of the weight loss curve (TG) is often included in the protocol (DTG) and used to interpret data in more detail and precision. As DTG profiles represent the derivatives of TG profiles, they show how fast or slow the weight of sample decreases. By analyzing the positions of peaks in DTG profile, useful information such as the types of decomposed species and the temperature at which the species may have been decomposed can be obtained.

In our case, as the SBA-15 materials were calcined at 550 °C after synthesis, the surfactant-loaded wet SBA-15 samples were at first dried by slowly evacuating and heated gradually up to about 50°C in an oven. The thermogravimetric analysis itself was then carried out in the

temperature range from 30 to 1000 °C, in artificial air (N_2 /N_2/O_2) at a heating rate of 10 $K \cdot min^{-1}$. The ambience of artificial air at high temperatures leads to a complete gasification of the surfactants during decomposition (C → CO_2; H, O → H_2O; N → N_2, NO/NO_2; Cl → HCl).

Measurements of the surfactant-loaded SBA-15 materials were made with a TGA instrument of type NETZSCH TG 209 F1 in the laboratory of Dr. K. Tauer of the Colloid Chemistry Department at MPI KG Potsdam.

Chapter 5

Adsorption measurements

This chapter presents results of adsorption measurements of two cationic surfactants in SBA-15 and of supplementary adsorption measurement of nonionic surfactants in SBA-15 silica. The results of these measurements are needed for the evaluation of the neutron scattering measurements. The results of both experiments will then be employed to compare the adsorption isotherms of the same cationic surfactants on nonporous silica beads or to discuss the reliability of adsorption experiments in general.

5.1 Adsorption isotherms of DPCl and CPCl in SBA-15

Adsorption isotherms of the cationic surfactants dodecyl pyridinium chloride (C_{12}PCl = DPCl) and hexadecyl pyridinium chloride (C_{16}PCl = CPCl) in SBA-15 were measured at room temperature (23 ± 2 °C) using the depletion method. To prepare the suspension of SBA-15 silica, an appropriate amount of SBA-15 powder was weighed into a 10-mL polycarbonate tube and (10 - x) g of 0.1 or 0.001 M KCl solution was added, where x is the amount of surfactant solution. The suspension was then sonified for several minutes and then the pH was adjusted to pH 9 using 0.1 M or 1 M NaOH. Subsequently, x g aqueous surfactant solution of known concentration was added to give total mass of 10 g.

After equilibration the concentration of the cationic surfactants in the supernatant was measured by UV-Vis spectroscopy using a CARY 50 Tablet UV-Vis Spectrophotometer by Varian Inc. For this purpose the UV absorption spectrum of the supernatant was measured between 200 nm and 350 nm and the absorption intensity of the pyridinium ion was determined at 260 nm. In most cases the supernatant had to be diluted appropriately to get a reasonable absorption spectrum because the concentration of surfactant in the supernatant was too high for the UV/Vis spectrometer to be measured with reliable accuracy. Thus a calibration measurement was performed beforehand between the concentration region of 0 and 0.25 mmol (DPCl at 0.001 M KCl for example) to extrapolate the actual surfactant concentration from the diluted supernatant by using this calibration graph.

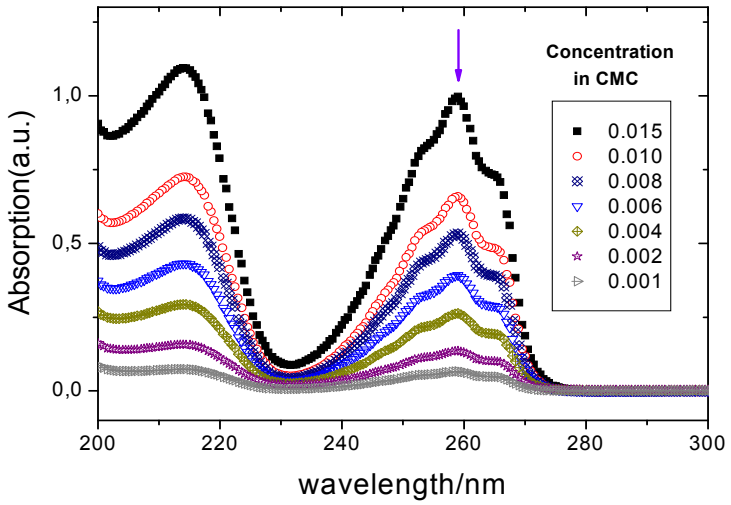

Fig.5.1 Typical UV/VIS spectra: here measured for calibration curve. The absorption peak of the pyridinium ion is marked by an arrow.

The adsorption isotherms of the two surfactants were measured in a wide concentration range to a concentration several times the CMC of the surfactants at two salt concentrations (0.1 M and 0.001 M). The primary aim of this measurement was to determine the plateau value of the adsorption isotherm in the pores of SBA-15 for further investigation on the structure of surfactant aggregates in the pore of SBA-15 silica.

The resulting adsorption isotherms of the surfactants DPCl and CPCl in SBA-15 for two concentrations of electrolyte (0.1 M and 0.001 M KCl) are shown in Fig. 5.2 and Fig. 5.3, respectively. For both surfactants, the isotherms are presented in a log-log plot (left) as well as in a lin-lin plot (right).

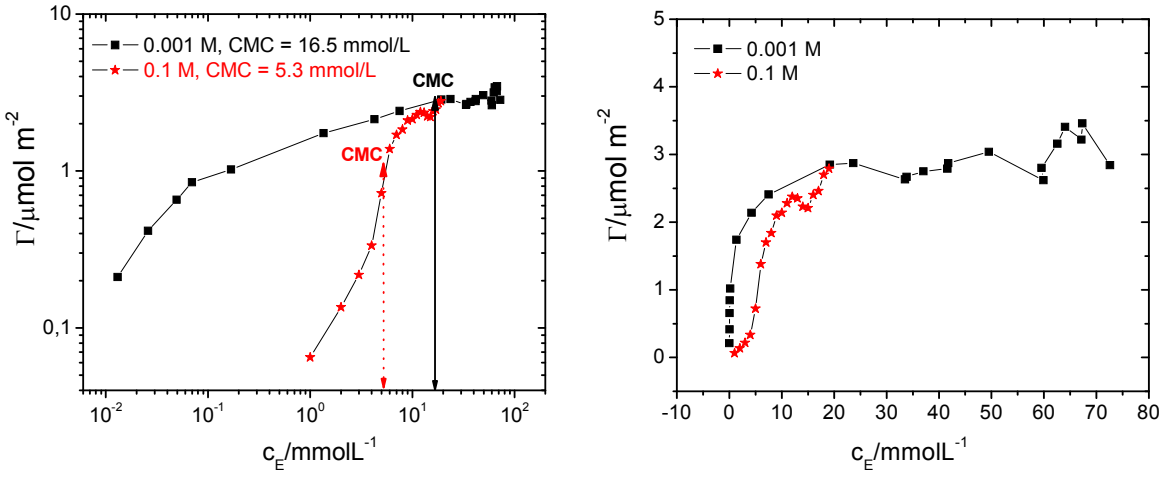

Fig. 5.2: Isotherms of DPCl adsorption in SBA-15 at 0.1 M and 0.001 M KCl concentration (pH = 9).

For both cationic surfactants at high salt concentration, the isotherm shapes in a lin-lin plot reflect the well-known two-step adsorption mechanism (S-type adsorption isotherm).

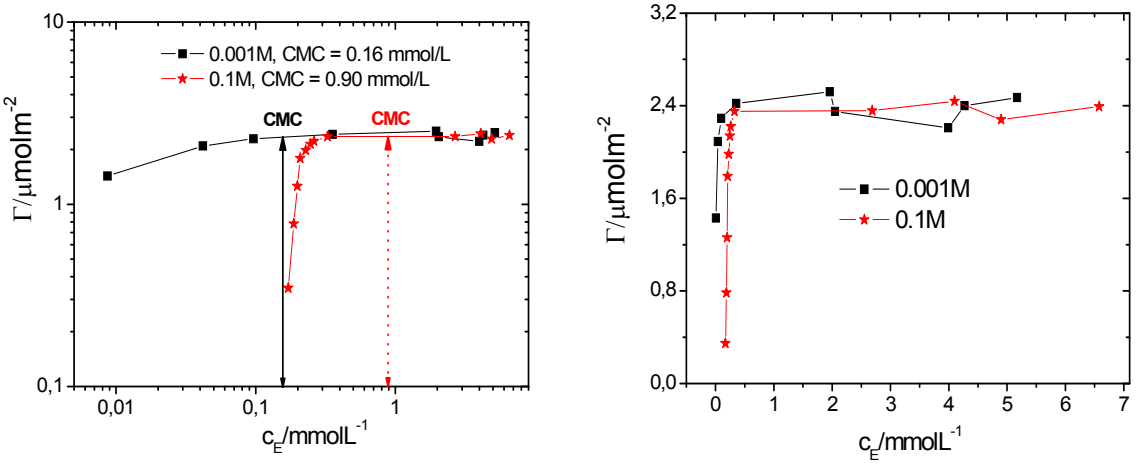

Fig. 5.3: Isotherms of CPCl adsorption in SBA-15 at 0.1 M and 0.001 M KCl concentration (pH = 9).

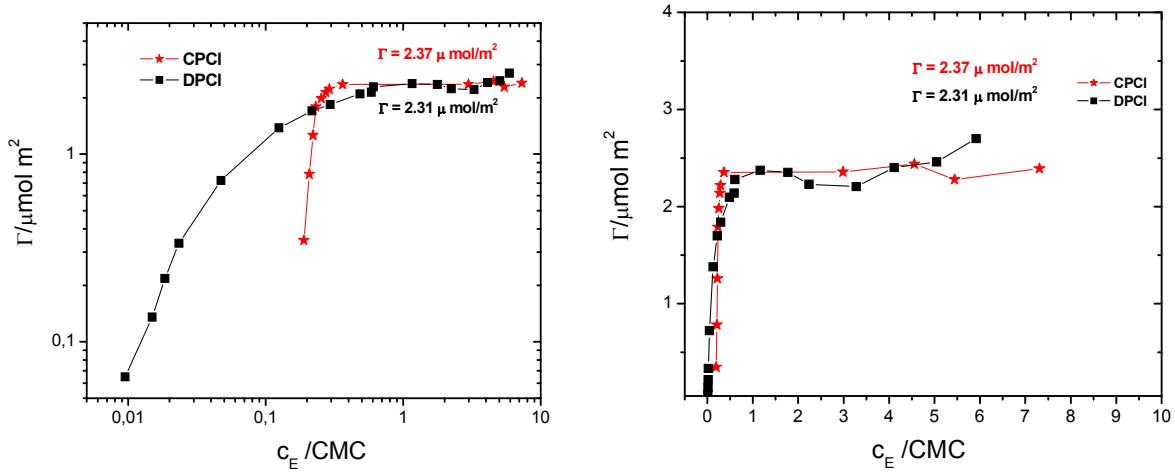

Fig. 5.4 Adsorption isotherms of DPCl and CPCl in SBA-15 at 0.1 M KCl and pH = 9.

Adsorption isotherms of dodecyl pyridinium chloride and cetyl pyridinium chloride on a nonporous silica (Aerosil OX50) obtained by Goloub and Koopal [Golo97] show significant differences between two salt concentrations and between the two alkyl chain lengths. In the nanopores of SBA-15, the plateau values of the adsorption isotherms are significantly lower than on the silica beads OX50. Experimental results reported by Goloub and Koopal are summarized and compared with the results of the present work in Table 5.1.

	Γ_m in μmol m^{-2}	
	OX50	SBA-15
DPCl (0.1M)	4.0	2.5
CPCl (0.1M)	5.0	2.4
DPCl (0.001M)	2.7	2.39
CPCl (0.001M)	4.3	2.44

Table 5.1: Plateau values of the adsorption isotherms of DPCl and CPCl on silica beads (OX50) and in the periodic mesoporous silica SBA-15 measured at two electrolyte concentrations (0.1 M and 0.001 M of KCl solution).

As can be seen in Table 5.1, CPCl has a significantly higher plateau values Γ_m than DPCl on the OX50 silica nanoparticles and addition of electrolyte causes a significant increase of Γ_m for both surfactants. At low salt concentration, adsorption in the first layer as well as second layer of the surfactant bi-layer increases with the chain length of the surfactant molecule, so that the difference in the plateau values of adsorption isotherm is smaller for CPCl than for DPCl in the case of OX50.

In the case of SBA-15, however, these differences are almost absent. Neither significant effect of salt concentration nor an influence of the chain length of the hydrophobic alkyl chain on the maximum amount of surfactant adsorption was observed for the adsorption in SBA-15.

5.2 Adsorption isotherms of nonionic surfactants in SBA-15

The influence of the pore size on the adsorption of nonionic surfactants was studied in a systematic way by Dietsch et al [Diet07] by measuring adsorption isotherms of the surfactant C_8E_4 in a series of controlled-pore glass materials (CPG-10) with mean pore widths in the range 10 to 50 nm. Pronounced S-shaped adsorption isotherms were found for all materials but a decrease of the plateau value Γ_m with decreasing pore width was found when the pore size was below 25 nm. Preliminary results for the adsorption of C_8E_4 in a SBA-15 material of pore diameter 8.5 nm and a MCM-41 material of 2.9 nm obtained by R. Dabiri [Dab02] confirm this trend, which is shown in Figure 5.5.

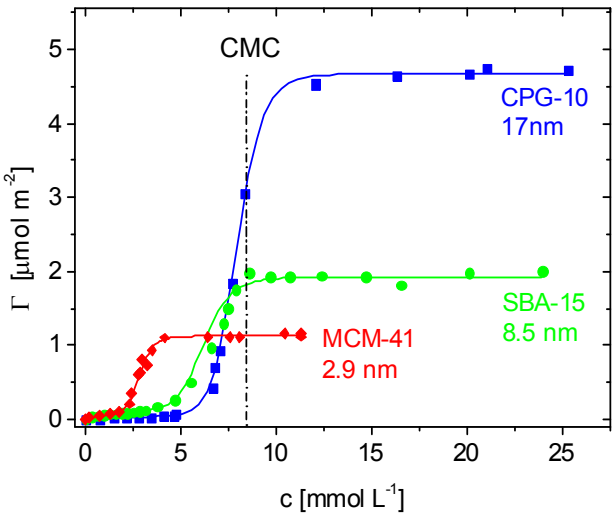

material	Γ_m (μmol m^{-2})	c_0 (mmol L^{-1})
CPG-10	4.7	10
SBA-15	1.9	8
MCM-41	1.2	4

Fig. 5.5: Influence of pore size on the surfactant adsorption. Decrease of Γ_m, and c_0 with decreasing pore width [Dab02], where Γ_m is the maximum surface coverage, and c_0 is critical surface aggregation concentration. The Γ_m and c_0 values are summarized in the table (right).

Adsorption isotherms of $C_{10}E_5$ and $C_{10}G_2$ in a SBA-15 material of ca. 7 nm pore diameter obtained by Eltekov [Find07] are presented in Appendix A1. These results, like those mentioned above, were obtained by micro-column adsorption chromatography. Recently the adsorption isotherm of $C_{12}E_5$ in one of the present SBA-15 materials (sample D16 – 129, see table 4.1) was determined in our group by the classical depletion method, using surface tension measurements to determine the concentration of the surfactant in the supernatant solution. This

isotherm, shown in Figure 5.6, has a plateau value of 1.25 mmol/g, corresponding to a limiting surface concentration $\Gamma_m \approx 1.53$ μmol m^{-2} [Müt10].

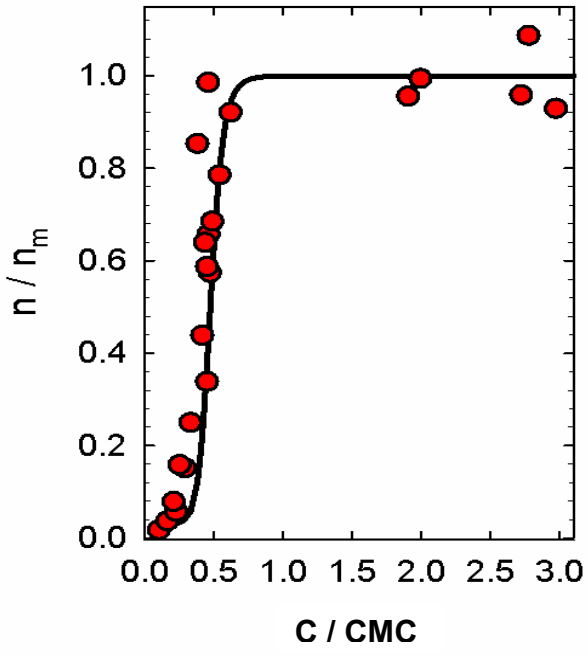

Fig 5.6 Adsorption isotherm of $C_{12}E_5$ in SBA-15 obtained by using surface tension measurements.

5.3 TGA measurement

As an independeant check of the direct adsorption measurements, the amount of surfactant in the samples studied by SANS was determined by Thermogravimetric Analysis (TGA). As explained in Section 4.2, the samples were prepared by equilibrating known amounts of SBA-15 with aqueous solutions of the surfactant such that the amounts of surfactant corresponds to fractions f = 1/3, 2/3, or 3/3 of the plateau value Γ_m of the adsorption isotherm[4]. Since the SANS measurements were made in aqueous solvents of different scattering length density (SLD), it was also of interest to check if the isotope composition of the H_2O/D_2O mixtures had an influence on the adsorption equilibrium of the surfactant in the pores. Accordingly, in the following figures the samples are identified by the following parameters: type of surfactant, nominal adsorbed surfactant amount expressed by filling fraction f, SLD (expressed in units of

[4] For this TGA measurement, the SBA-15 samples of experiment D16:9-10-847 (see Appendix) were used, the rest portions of which were reserved after SANS measurement.

10^{10} cm^{-2}) of H_2O/D_2O mixture used in the sample preparation: SLD = 3.7 (contrast-matching mixture = M), SLD = 5.0 and SLD = 6.3 (pure D_2O = D), and concentration of electrolyte in the case of cationic surfactants.

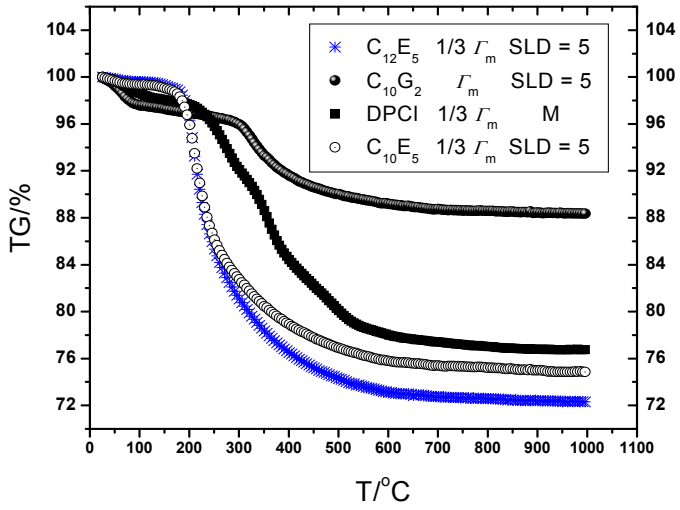

Fig. 5.7: TGA profiles of SBA-15 samples adsorbed with the 4 different surfactants investigated in the present work.

The TGA and DTG curves of SBA-15 samples show characteristic behaviours depending on the type of adsorbed surfactants, as demonstrated in Figure 5.7, where representative TGA curves of SBA-15 samples loaded with four different surfactants are presented. A multi-step weight loss is observed for the SBA-15 samples with adsorbed DPCl, while the TGA profiles of other samples show rather simple temperature dependence. In general, three regions of weight loss are observed.

These regions are marked by three limiting temperatures T_0, T_1 and T_2. T_0 is the temperature at which the TGA measurement starts, while T_1 and T_2 represent the lower and upper end temperature of the surfactant decomposition. Accordingly, the first region from the initial temperature T_0 (30°C) up to T_1 is assigned to the loss of physically bound water and break-up of hydrogen bonded network[5]. In this region, weight losses between 0.4% and 3.9% were observed depending on the type of adsorbed surfactant. The shape of each TG profile and the final temperature of this region clearly depend on the type of surfactant: e.g. For $C_{10}G_2$ the first

[5] In case of pure silica, it is reported that most of the physically adsorbed water is removed below 150°C and at 200°C all the water from the surface is gone [Mir07].

region ends at about 100°C, for DPCl at about 120°C, for $C_{12}E_5$ and $C_{10}E_5$ at about 160°C (see Table 5.2).

Sample	T_1/°C	m_1/%	m_2/% (at T_2)
$C_{10}E_5$ 1/3 Γ_m(5)	161	99.1	75.4
$C_{10}E_5$ 2/3 Γ_m (M)	162	99.3	60.5
$C_{10}E_5$ 3/3 Γ_m (D)	161	98.9	57.6
$C_{12}E_5$ 1/3 Γ_m (5)	166	99.1	72.8
$C_{12}E_5$ 2/3 Γ_m (D)	166	99.3	56.8
$C_{12}E_5$ 3/3 Γ_m (M)	161	99.5	65.6
$C_{12}E_5$ 3/3 Γ_m (5)	161	99.6	57.0
$C_{10}G_2$ 1/3 Γ_m (M)	101	97.2	86.7
$C_{10}G_2$ 2/3 Γ_m (M)	101	97.5	85.3
$C_{10}G_2$ 3/3 Γ_m (M)	101	98.3	85.3
$C_{10}G_2$ 1/3 Γ_m (D)	91	96.1	88.5
$C_{10}G_2$ 2/3 Γ_m (5)	91	96.6	88.4
$C_{10}G_2$ 3/3 Γ_m (5)	91	97.7	88.7
DPCl 1/3 Γ_m (M)	156	98.0	77.4
DPCl 2/3 Γ_m (D)	121	99.0	65.7
DPCl 3/3 Γ_m (5)	121	99.0	61.3

Table 5.2. The final temperature of water desorption region (T_1), TG value at this temperature (m_1) and TG value at a temperature T_2 = 700°C (m_2) are given. Samples are denominated after the type of surfactant, surfactant amount as fraction of the plateau value Γ_m of adsorption isotherm, and the scattering length density of solvent.

Above T_1, the TGA curves show a large loss of mass which can be attributed to the decomposition of adsorbed surfactant molecules. Further, each surfactant type exhibits a sample-specific progress in the second region. In the range above the calcination temperature of SBA-15 materials (about 550°C), the TG value continues to decrease, which however cannot directly be associated with decomposition of adsorbed surfactant. This part of weight loss may be due to dehydroxylation of the silica surface, but further studies would be necessary

to corroborate this conjecture. Therefore, the TG value was taken not at the final temperature of the TGA measurement, but at $T_2 = 700°C$ to determine the mass fraction of SBA-15 powder and finally that of adsorbed surfactant in SBA-15.

To calculate the mass fraction of the adsorbed surfactant, the temperatures T_0, T_1 and T_2 were at first determined by analyzing the DTG profile of the respective sample. The TG values $m_0 = m(T_0)$, $m_1 = m(T_1)$, and $m_2 = m(T_2)$ were then taken at these temperatures. The mass fraction of surfactant can finally be calculated after following relation:

$$m_{surf} / m_s = \Delta m_{12} / m_2, \tag{5.1}$$

where $\Delta m_{12} = m(T_1) - m(T_2)$. The specific surface area a_s of employed SBA-15 material was then applied to convert the mass fraction of surfactant to Γ as follows,

$$\Gamma = m_{surf} / (M \cdot m_s \cdot a_s). \tag{5.2}$$

The TG and DTG profiles of SBA-15 samples with different types of adsorbed surfactant will be presented in the following. TG profiles exhibit up to 4 points of inflection depending on the type of adsorbed surfactant. At the points of inflection, precedent slow decrease turns to a maximum slope and in case of the last one in a TG profile, the TG value approaches asymptotically to a minimum value after it. These points of inflection in TGA curves appear in DTG profiles as pronounced downward peaks.

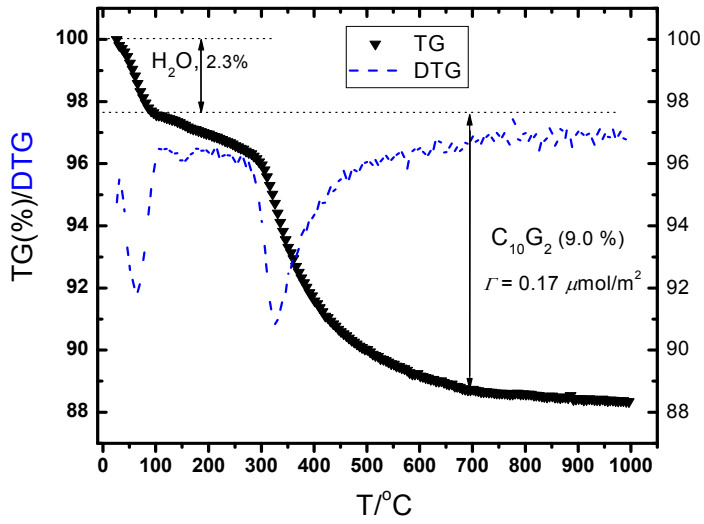

Fig.5.8. TG and DTG curves of SBA-15 sample with adsorbed $C_{10}G_2$ (Γ_m), prepared in water of SLD = 5.0. For the surfactant $C_{10}G_2$, 9.0 % weight loss corresponds to a Γ value of 0.17 μmol/m^2.

The SBA-15 samples with adsorbed decyl maltoside ($C_{10}G_2$) exhibit a point of inflection even in a relatively short first region of weight loss (up to ca. 100°C) followed by a linear decrease up to ca. 300°C which then turns into a steep decrease with a point of inflection at ca. 330°C.

In Figure 5.8, the weight loss of physically bound water and break-up of hydrogen bonded network as well as the mass fraction of adsorbed surfactant is presented by marking them with double arrows and corresponding values.

The SBA-15 samples with adsorbed alkyl ethoxylates ($C_{10}E_5$ and $C_{12}E_5$) show the simplest TGA and DTG profiles among all SBA-15 samples. Their TG profiles show two clearly separated regions: an initial region of linear decrease in weight (no pronounced point of inflection) up to ca. 160°C is followed by a region of monotonous exponential decrease, which is attributed to surfactant desorption and decomposition.

Typical TG and DTG profiles of SBA-15 samples with adsorbed $C_{10}E_5$ and $C_{12}E_5$ are shown together in Figure 5.9, for the sake of better comparison. The similarities in TG and DTG profiles as well as positions of T_1 (ca. 160°C) indicate similar adsorption behaviour of these two surfactants in SBA-15.

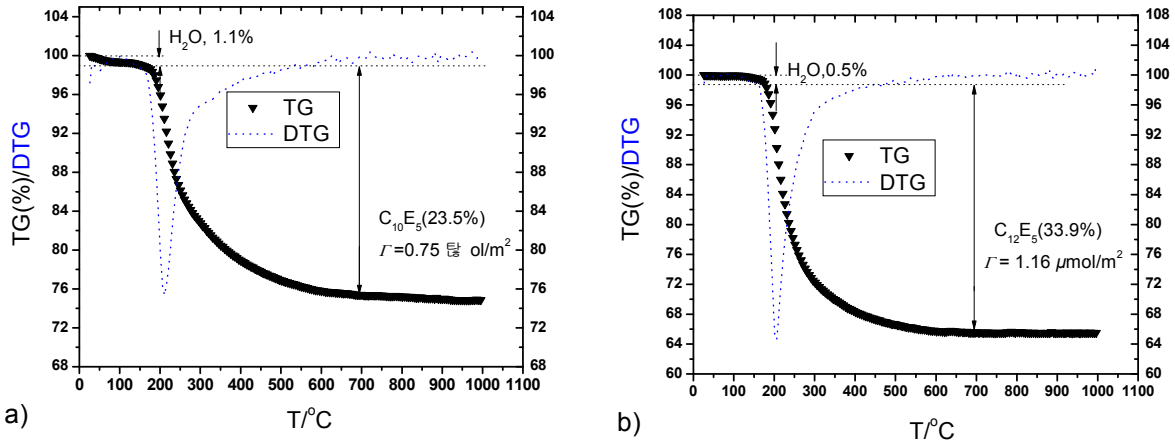

Fig.5.9 Typical TG and DTG profiles of SBA-15 sample with adsorbed a) $C_{10}E_5$ (1/3 Γ_m) in the water of SLD = 5 and b) $C_{12}E_5$ (Γ_m, M).

The TGA patterns of SBA-15 samples with adsorbed dodecyl pyridinium chloride (DPCl) show four points of inflection which can be characterized by DTG analysis in detail. The first region, which reaches up to 156°C is attributed to desorption of physically bound water and the break-up of hydrogen bonded network. Three steps of weight loss are then observed in the temperature range up to 520°C. These weight loss regions can also be identified with downward peaks in the DTG profile. The positions of the three minima in the DTG profiles are at nearly the same temperatures for all SBA-15 samples with adsorbed DPCl, independent of surfactant amount.

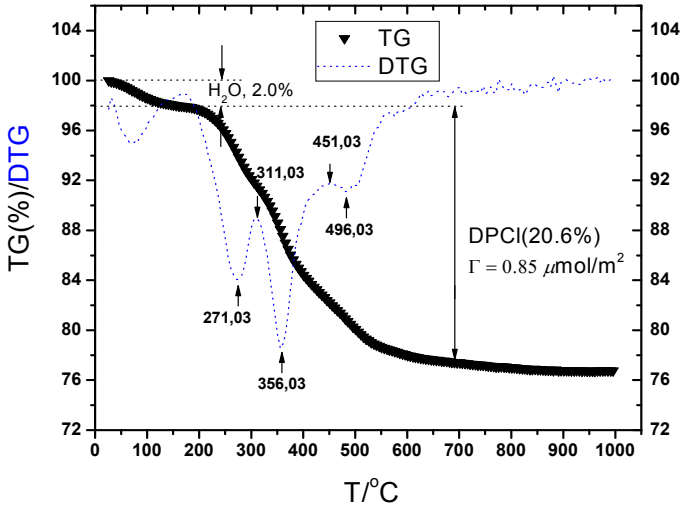

Fig.5.10: Typical TG and DTG curves for SBA-15 with adsorbed DPCl (1/3 Γ_m, M). The DTG profile of this sample exhibits three peaks after desorption of water (at ca. 120°C). The positions marked by arrows are present at the same temperature in all other SBA-15 samples with adsorbed DPCl.

Results and Discussion

The results of all TGA measurements on the surfactant contents in the SBA-15 samples are summarized in the Tables 5.3 to 5.6 and Figures 5.11 to 5.14. In the tables, values of the surface concentration Γ from TGA are given for samples prepared for nominal surface concentrations 1/3 Γ_m, 2/3 Γ_m and Γ_m in pure D_2O and in two H_2O/D_2O mixtures of scattering length density $5.0 \cdot 10^{10}$ and $3.7 \cdot 10^{10}$ cm^{-2}, respectively. The values of the plateau value used

in the sample preparation were taken from earlier determinations (or estimations) of this quantity and are given in the first column of the tables. In the figures, all TGA profiles of SBA-15 samples for the sake of comparison. Separate TGA and DTG profiles for each sample are given in the Appendix.

The results for the surfactant $C_{10}E_5$ presented in Table 5.3 indicate that for the nominal loadings 1/3 Γ_m and 2/3 Γ_m the amount of surfactant adsorbed in the SBA-15 material determined by TGA is in reasonably good agreement with the values estimated with the plateau value Γ_m. However, the TGA value for nominal loading Γ_m is significantly lower than the estimated Γ_m. This finding may be associated with an instability of SBA-15 against exposure to water. Galarneau et al. report a 52 % lost of the micropore volume of SBA-15 synthesized below 110°C, which leads to a 50 % decrease of specific surface area a_s, a 15 % increase in mesopore size and 11 % mesopore volume during water treatment [Garl07]. The increase of mesopore volume due to the decrease of micropore volume may slightly increase the amount of adsorbed surfactant in the pore, because the micropores are originally not accessible for surfactant molecules ever. However, overestimated amount of added surfactant during preparation is significantly large due to the large decrease of specific surface area (50 %), because it was calculated on the basis of the specific surface area a_s, which is obtained through N_2 sorption measurement.

The largest discrepancy between the plateau value from adsorption isotherm and that from TGA measurement is observed for the SBA-15 samples with adsorbed $C_{10}G_2$, where values of 0.18 ± 0.01 μmol/m^2 were measured by TGA for the SBA-15 samples prepared at the surfactant concentrations of 2/3 Γ_m and Γ_m, while a value of 1.0 μmol/m^2 was applied as Γ_m for sample preparation.

Another aspect may not be omitted: Some SBA-15 samples prepared with the same surfactant amount show different TGA values depending on the scattering length densities of used solvent (confer columns 3 and 4 of Table 5.5). For a quantitative and conclusive analysis further extensive and systematic investigation is necessary.

TGA results for $C_{10}E_5$ in SBA-15

Γ from adsorption isotherm	Γ from TGA		
	6.3(D_2O)	5.0	3.7(M)
1/3 Γ_m = 0.67		0.75	
2/3 Γ_m = 1.33			1.54
Γ_m = 2.00	1.73		

Table 5.3. Values of Γ in μmol/m^2 for different nominal levels of adsorption as determined from a direct determination of the plateau value of the adsorption isotherm (Γ_m = 2.0 μmol/m^2) are presented in the first column. The values of Γ in column 2-4 were obtained by TGA for samples prepared in water of different H_2O/D_2O ratio (here expressed by the SLD).

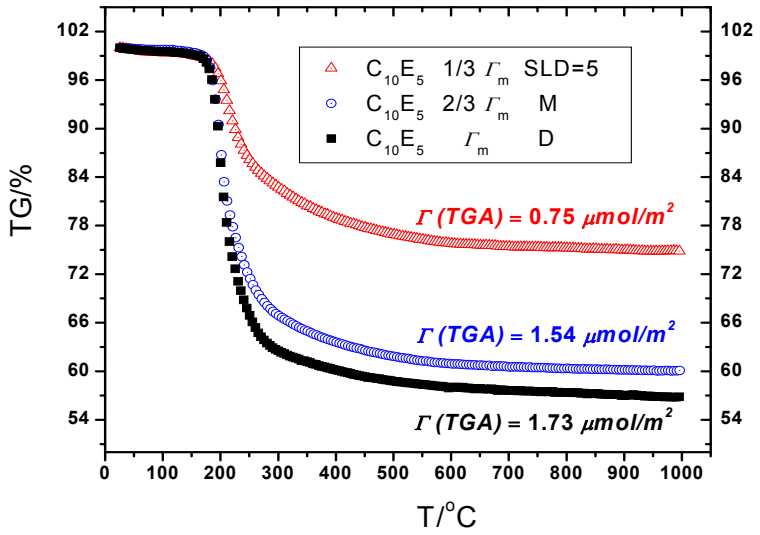

Fig.5.11. TGA curves of SBA-15 adsorbed by $C_{10}E_5$ with different amount of surfactant in contrast matching water (M), in the water of SLD = 5.0 and in pure D_2O (D). Corresponding surfactant amounts were calculated according to weight loss in the TGA.

TGA results for $C_{12}E_5$ adsorbed SBA-15

Γ from adsorption isotherm	Γ from TGA	
	5.0	3.7(M)
1/3 Γ_m = 0.80	0.81	
2/3 Γ_m = 1.60	1.68	
Γ_m = 2.40	1.68	1.16

Table 5.4. Values of Γ in μmol/m^2 for different nominal levels of adsorption as determined from a direct determination of the plateau value of the adsorption isotherm (Γ_m = 2.4 μmol/m^2) are given in the first column. The values of Γ in column 2 and 3 were obtained by TGA for samples prepared in water of different H_2O/D_2O ratio (here expressed by the SLD).

The Γ values 1.68 μmol/m^2 for both 2/3 Γ_m and Γ_m surfactant loadings seem to be absurd but a recent adsorption measurement employing surface tension measurement (see p. 55) reports a plateau value of Γ_m =1.53 for $C_{12}E_5$, which supports these TGA results.

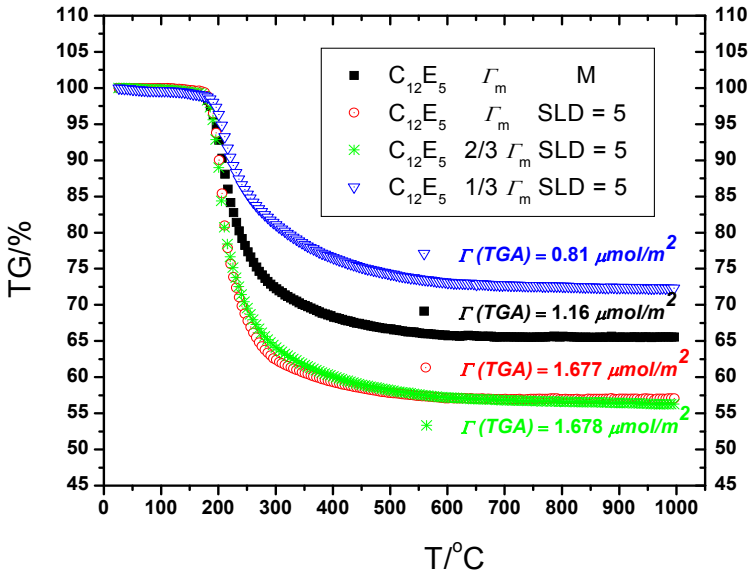

Fig.5.12 TGA curves of SBA-15 with adsorbed $C_{12}E_5$ with different amount of surfactant in contrast matching water (M), in the water of SLD = 5.0 and in pure D_2O (D). Corresponding surfactant amounts were calculated according to the weight loss in the TGA.

TGA results for $C_{10}G_2$ in SBA-15

Γ from adsorption isotherm	Γ from TGA		
	6.3(D_2O)	5.0	3.7(M)
1/3 Γ_m = 0.33	0.17		0.23
2/3 Γ_m = 0.67		0.17	0.27
Γ_m = 1.0		0.19	0.29

Table 5.5. Values of Γ in μmol/m^2 for different nominal levels of adsorption as determined from a direct determination of the plateau value of the adsorption isotherm (Γ_m = 1.0 μmol/m^2) are given in the first column. The values of Γ in column 2-4 were obtained by TGA for samples prepared in water of different H_2O/D_2O ratio (here expressed by the SLD).

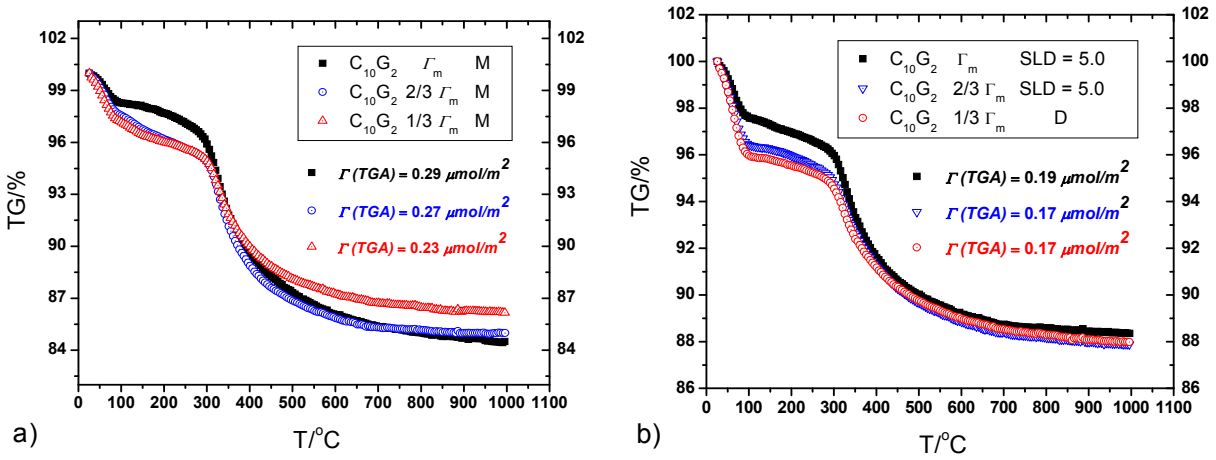

Fig.5.13: TGA curves of SBA-15 adsorbed by $C_{10}G_2$ and corresponding surfactant amounts calculated according to the weight loss in the TGA: a) in contrast matching water (M), b) in SLD = 5.0 and in pure D_2O.

TGA results for DPCl in SBA-15

Γ from adsorption isotherm	Γ from TGA		
	6.3(D_2O)	5.0	3.7(M)
1/3 Γ_m = 0.83			0.85
2/3 Γ_m = 1.66	1.63		
Γ_m = 2.50		1.97	

Table 5.6. Values of Γ in μmol/m^2 for different nominal levels of adsorption as determined from a direct determination of the plateau value of the adsorption isotherm (Γ_m = 2.5 μmol/m^2) are given in the first column. The values of Γ in column 2-4 were obtained by TGA for samples prepared in water of different H_2O/D_2O ratio (here expressed by the SLD).

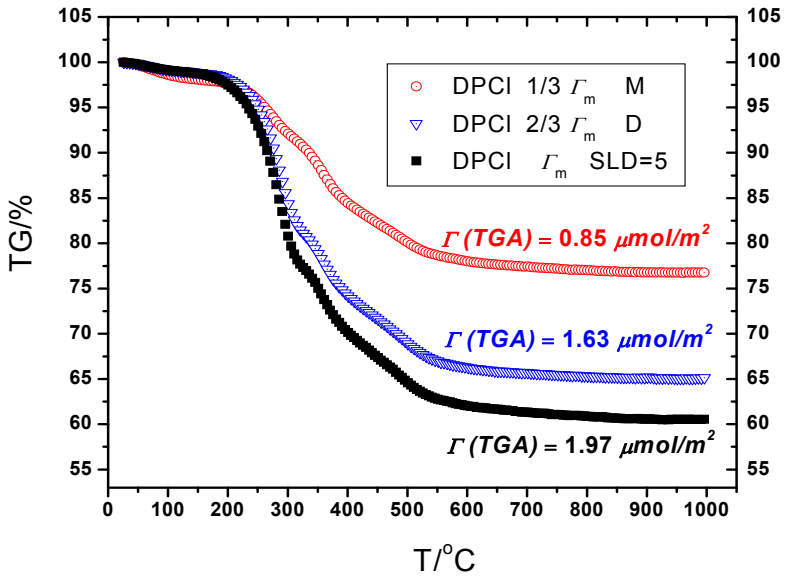

Fig.5.14: TGA curves of SBA-15 adsorbed by DPCl in contrast matching water (M), in the solvent of SLD = 5.0 and in pure D_2O (D). Corresponding surfactant amounts were calculated according to the weight loss in the TGA are given at the position of each TGA profile.

Chapter 6

SANS studies of Cationic Surfactants in SBA-15

The organisation of cationic surfactants (DPCl and CPCl) adsorbed in the cylindrical pores of a periodic mesoporous silica (SBA-15, pore diameter ca. 8 nm) has been studied by small-angle neutron scattering at different solvent contrast conditions. The cationic surfactants DPCl and CPCl were chosen as examples for surface-dominated behaviour. Due to electrostatic attraction between the negatively charged silica pore wall and the surfactant head group, the interaction strength of the cationic surfactants is the strongest among all surfactants investigated in the present work. The combination of attractive solid-wall interactions and repulsive electrostatic interaction between the charged head groups leads to a characteristic adsorption behaviour.

A SANS study of these systems was first performed at instrument V4 at the BER II reactor at the Helmholtz Zentrum für Materialien und Energie (HZB). In a series of SANS measurements, the fundamental features of the scattering curves could be resolved. In the experimental q range the scattering curve of SBA-15 is dominated by Bragg peaks resulting from the ordered array of mesopores. It is found that the peak intensities are strongly affected by the surfactant adsorption and the solvent contrast. The scattering curves can be modelled by combining the structure factor of a 2D hexagonal lattice with the form factor of a core-shell cylinder, in which the adsorbed surfactant film is represented by the shell of the cylinder. This simple model accounts to some extent for the experimental findings and provides a direct method for estimating the thickness of the adsorbed film at the pore walls. However, these measurements at HZB were limited by the instrumental resolution of the beam line V4, which was not high enough to seperate the Bragg peaks *(11)* and *(20)* of the silica matrix. Measurements at a higher instrumental resolution could later be performed at the small momentum transfer diffractometer D16 at the Institute Laue Langevin (ILL). In this Chapter, the low-resolution results obtained at HZB are presented in Section 6.1 and the high-resolution scattering data obtained at ILL are presented in Section 6.2.

6.1 Low-resolution results and analysis*

6.1.1 Fundamentals of analysis

For the analysis of the SANS curves a theoretical model [Imp00] was adopted which combines the structure factor of a 2D hexagonal lattice of cylindrical pores with the form factor of a three-density-level core-shell cylinder (see Figure 6.1). It is assumed that the pores are monodisperse and of circular cross-section and perfectly ordered on the lattice. The system is fully isotropic due to the powder form of the SBA-15 matrix. The spherically averaged total scattered intensity is modelled as [Imp00, Schre01, Zick06]

$$I(q) = KS(q)\left|F(q)\right|^2 + I_{diff}(q) + I_{inc} \tag{6.1}$$

where the first term describes the Bragg reflections from the ordered structure, with $S(q)$ the structure factor and $F(q)$ the scattering amplitude of the cylindrical pores with or without an adsorbed film, and K is a constant. $I_{\mathrm{diff}}(q)$ represents the diffuse scattering due to micropores or other inhomogeneities of the matrix, and I_{inc} is the incoherent scattering mostly due to protons of the solvent and surfactant. Using the Miller indices (hk) for the lattice planes of a 2D lattice, the structure factor $S(q)$ of an ideal undistorted lattice can be written as

$$S(q) \propto \frac{1}{q^2} \sum_{(hk)} m_{hk} L_{hk}(q) \tag{6.2}$$

with m_{hk} the peak multiplicity ($m_{\mathrm{h0}} = m_{\mathrm{hh}} = 6$, otherwise $m_{\mathrm{hk}} = 12$) and $L_{\mathrm{hk}}(\mathrm{q})$ the peak shape function, which for a Gaussian peak shape becomes $L_{\mathrm{hk}}(x) = (2/\pi\delta)\exp(-4x^2/\pi\delta^2)$, where δ is a parameter related to the standard deviation [Förs05], $x = (q - q_{\mathrm{hk}})$, and

$$q_{hk} = \frac{4\pi}{a_0\sqrt{3}} \sqrt{h^2 + k^2 + hk}\ . \tag{6.3}$$

The scattering amplitude of a uniform core-shell cylinder with scattering length densities of the core (ρ_1), adsorbed film (ρ_2) and matrix (ρ_3) (cf. Fig.6.2) is

* Results of this section were published in Progr Colloid and Polym Sci. 133, 116-122, 2006.

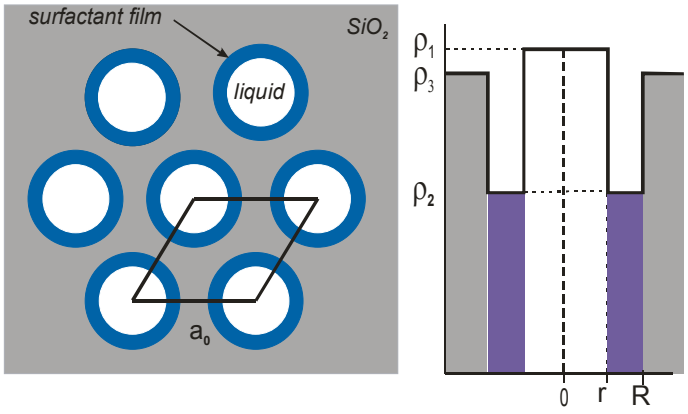

Fig. 6.1. Sketch of the 2D hexagonal packing of cylindrical pores coated with an adsorbed surfactant film (left) and density profile $\rho(r)$ of a three density level core-shell cylinder (ρ_1, liquid core; ρ_2, surfactant film; ρ_3, matrix) (right)

$$F(q) = 2\pi\left[(\rho_3 - \rho_2)R^2 \frac{J_1(qR^2)}{qR} + (\rho_2 - \rho_1)r^2 \frac{J_1(qr^2)}{qr}\right] \tag{6.4}$$

where R is the pore radius, r the inner radius of the adsorbed film, and J_1 is the Bessel function of the first order. Calculations for the form factor $P(q) = |F(q)|^2$ with fixed values of the pore radius (R = 4.0 nm) and scattering length density of the silica matrix ($\rho_3 = 3.7 \cdot 10^{10}$ cm^{-2}) and appropriate choices of the parameters r, ρ_1 and ρ_2 are shown in Figs. 6.4b and 6.5b. Results for the whole model function of Eq. 6.1 are shown in Fig. 6.6.

Figure 6.2 visualizes the radial profiles of scattering length density for a single pore with adsorbed surfactant bilayer in two different contrast scenarios: “film-contrast (contrast-matching water)” and “film and water-contrast (D_2O)”.

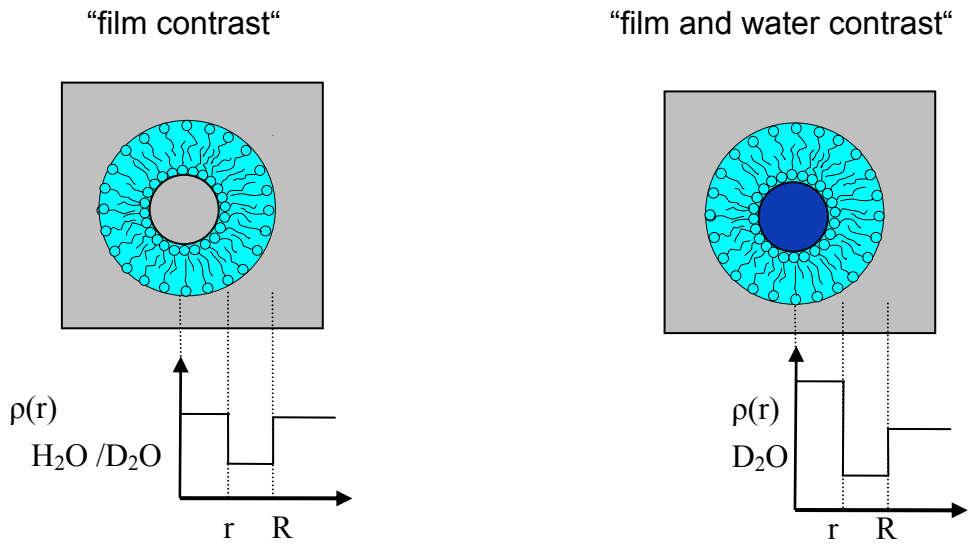

Figure 6.2: The radial profile of scattering length density for a single pore with adsorbed surfactant bi-layer in contrast matching solvent (left) and in D_2O (right).

6.1.2 Sample preparation

A high-quality sample of SBA-15 silica synthesized by the method reported by Zhao et al. [Zhao98] was used. Values of the specific surface area a_s, specific pore volume v_p, pore diameter D and lattice constant a_0 are given in Table 4.1 of Chapter 4 (V4 – 1091).

Samples of SBA-15 with adsorbed surfactant layers corresponding to the plateau value of the adsorption isotherm at different ionic strengths of the solution were prepared by combining appropriate amounts of surfactant and silica in aqueous KCl solutions (‘mixing-type’ samples). Initially, KCl solutions of required concentration (0.1 or 0.001 M) were prepared with water samples of different D_2O volume fractions, denoted as solvent A, B and C (Table 6.1). A suspension of 0.12 g SBA-15 in 10 g of this solution was prepared at pH 9, and the estimated amount of surfactant was added. After sonication and equilibration the supernatant was decanted, and the silica slurry was transfered into the sample cell shown in Figure 4.8. Samples of SBA-15 containing lower amounts of adsorbed surfactant were prepared from mixing-type samples by equilibration with known amounts of the H_2O/D_2O appropriate solvent and removal of the supernatant solution (‘washing-type’ samples).

Solvent	φ_H	ρ_l / 10^{10}cm^{-2}	I_{inc} / cm^{-1}	(I_{inc}–I_0) / cm^{-1}
A	0	6.3	0.05	0
B	0.197	5.0	0.29	0.12
C	0.385	3.7	0.17	0.24

Table 6.1. Composition φ_H (volume fraction of H_2O) and scattering length density ρ_l of the three H_2O/D_2O mixtures; I_{inc} represents the incoherent scattering of SBA-15/water samples in the absence of surfactant, I_0 is the respective value in SBA-15/D_2O.

6.1.3 Result and Discussion

SBA-15 in water. Scattering curves of SBA-15 embedded in water of three different scattering length densities (Table 6.1) are shown in Figure 6.3. The positions of the four leading Bragg reflexes (*10*, *11*, *20*, *21*) of this sample are indicated by vertical lines. In D_2O (solvent A), which gives a high scattering contrast against the silica matrix, the (*10*) reflex appears as an intense, broad peak centred at $q_{10} = 0.678$ nm^{-1}. The (*11*) and (*20*) reflexes are not resolved but form a joint peak due to the wavelength broadening of the neutron beam, and the (*21*) reflex appears only as a shoulder on top of the scattering background. The diffuse scattering intensity I_{diff} of the sample in D_2O falls off by about one order of magnitude in the q range from 0.4 to 4 nm^{-1}. When the scattering contrast of the liquid against the matrix is lowered, all Bragg peaks become less intense (curve for solvent B in Fig. 6.3). In the contrast-matching H_2O/D_2O mixture (solvent C) the Bragg peaks and diffuse scattering are entirely suppressed, except for an incoherent background I_{inc}, which is due mostly to the incoherent scattering of the protons of H_2O.

In the present work we assume that this incoherent background is given by the scattering intensity at $q > 4$ nm^{-1} where the scattering is independent of q. Fig. 6.3 shows that for SBA-15 in water, I_{inc} increases strongly from solvent A to C, and Table 2 indicates that the experimental values of I_{inc} are proportional to the H_2O content of the solvent, except for a small contribution I_0 which is also present in D_2O. This finding is to be expected as the amount of liquid in our slurry samples is similar in all measurements.

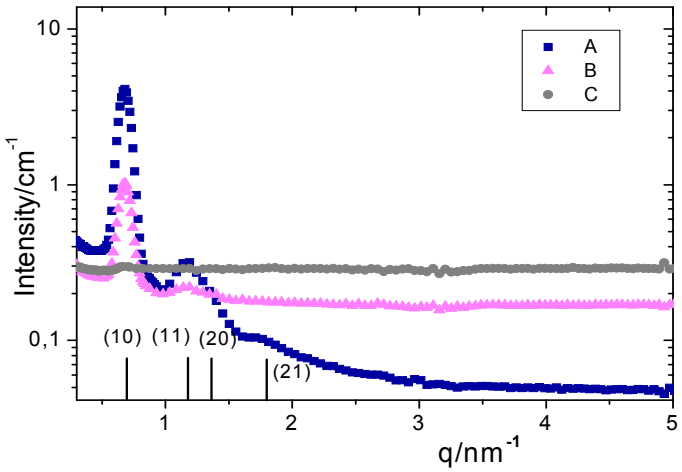

Fig. 6.3. SANS curve of SBA-15 in pure D_2O and two H_2O/D_2O mixtures of different scattering length densities (see Table 6.1). The positions of the leading Bragg reflections *(hk)* of SBA-15 are indicated by vertical lines.

SBA-15 with Adsorbed Surfactant

Solvent contrast variation. Figure 6.4a shows scattering curves from SBA-15 carrying an adsorbed layer of the surfactant DPCl, embedded in aqueous solutions of different scattering length densities (solvents A, B and C). The incoherent scattering background I_{inc} has been subtracted from the measured intensities in these graphs. The three samples were prepared in the same way (1 mM KCl solution, 'mixing type' protocol) and thus the state of the adsorbed surfactant film will be similar in these samples. Hence the curves in Fig. 6.4a show the influence of the solvent contrasts on the scattering at a given thickness of the adsorbed surfactant film. It is seen that the intensity of the (*10*) Bragg reflection decreases sharply with decreasing solvent contrast, but the broad peak centred near the *(11)* reflection and extending into the q range of the higher Bragg reflections is not strongly affected by the solvent contrast: There is some decrease in the scattered intensity from solvent A to solvent B, but no further decrease from B to C, where this broad peak is much stronger than the (*10*) peak.

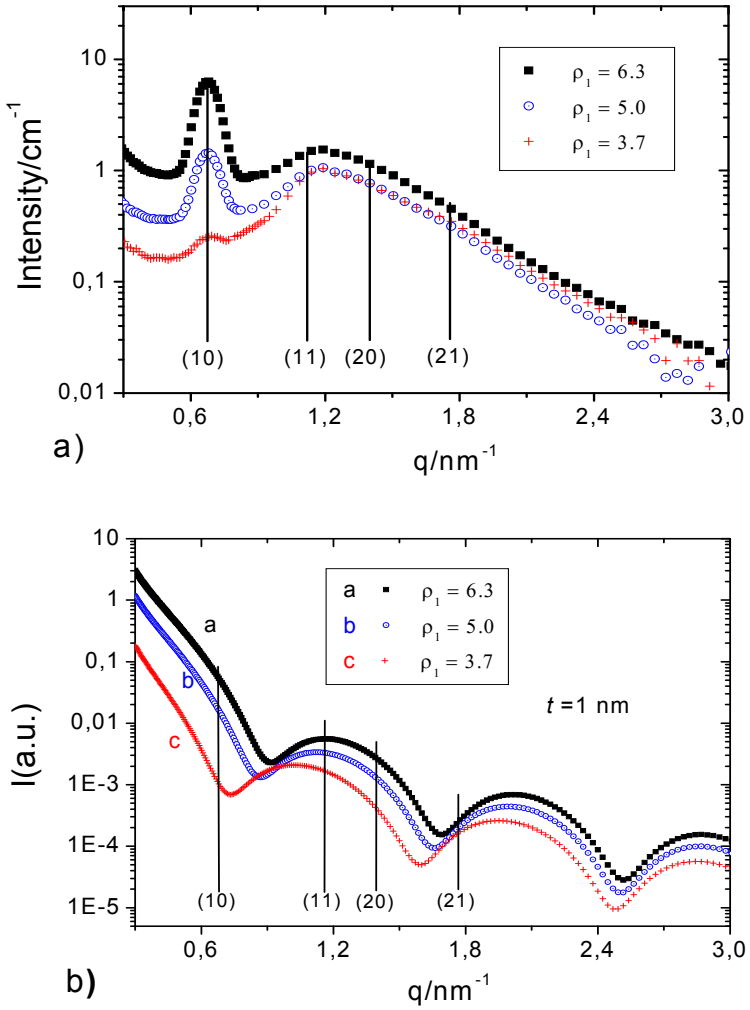

Fig. 6.4. (a) SANS curves from SBA-15 with an adsorbed film of DPCl for three solvent contrasts (water solvents A,B,C) at low salt concentration (1 mM KCl). The incoherent scattering has been subtracted for all samples; (b) Form factor of a core-shell cylinder with parameters appropriate for the SANS curves in (a)(see text). The positions of the Bragg reflections q_{hk} are indicated by vertical lines.

The main features of the scattering curves of Fig. 6.4a can be rationalized on the basis of the form factor model introduced above. Fig. 6.4b shows graphs of the form factor $|F(q)|^2$ as given by Eq. 6.4 for R = 4 nm and an adsorbed surfactant layer of thickness $t = R - r$ = 1 nm and scattering length density $\rho_2 = 1.65 \cdot 10^{10}$ cm^{-2}; the scattering length densities of the core liquid (ρ_1) are given for the three solvents in Table 2, based on the assumption that the core liquid consists of pure solvent. The graphs in Fig. 6.4b show that $|F(q)|^2$ is strongly dependent on ρ_1 in the q range near the (*10*) Bragg peak but less strongly dependent on ρ_1 in the q range near the (*11*) and (*20*) Bragg peaks. As the Bragg intensity $I(q_{hk})$ is proportional to $|F(q)|^2$ at $q = q_{hk}$ (Eq. 6.1), this result implies that the intensity of the (*10*) Bragg peak will decrease with decreasing scattering length density of the solvent while the intensity of the combined

(*11*)+(*20*) peak will be weakly dependent of ρ_1, in agreement with the experimental results of Fig. 6.4a. Hence the form factor model accounts for the observed influence of the solvent contrast on the intensities of the first and second Bragg peak. In particular, it shows that the pronounced decrease of the (*10*) peak intensity with decreasing scattering length density of the aqueous solvent is due to a decrease of the form factor at q values near the (*10*) peak.

Variation of layer thickness. The influence of the layer thickness of adsorbed surfactant films on the scattering curve of SBA-15 was studied with adsorbed films of DPCl and CPCl. It is well-established that the plateau value of the adsorption isotherm of cationic surfactants on silica increases with increasing ionic strength of the solution. Specifically, for the adsorption on a nonporous silica (Aerosil OX50) under the experimental conditions of the present work (pH 9) it is reported that an increase of the ionic strength from 10^{-3} M to 10^{-1} M KCl causes an increase of the plateau value of the adsorption isotherm from 2.7 to 4.0 μmol m^{-2} for DPCl, and from 4.3 to above 5 μmol m^{-2} for CPCl [Golo97]. Preliminary adsorption measurements of the two surfactants in the pores of SBA-15 support these trends, although the plateau values of the adsorption in the mesoporous SBA-15 matrix are significantly lower than at the surface of nonporous silica. Fig. 6.5a shows the influence of the surfactant layer thickness on the scattering curves of SBA-15 samples in film contrast (solvent C). In this figure, curves (a) and (b) represent films of CPCl corresponding to the plateau value of the adsorption isotherm in 10^{-1} M and 10^{-3} M KCl, respectively (mixing type samples), and curve (c) represents a film of DPCl prepared by the washing protocol in 10^{-3} M KCl. Hence the thickness of the adsorbed surfactant film decreases from (a) to (c). Fig. 6.5a shows that this decrease of the film thickness causes a systematic decrease of the (*10*) peak intensity. In the q range of the (*11*) and (*20*) reflexes the scattering intensity of samples (a) and (b) is similar and significantly higher than for sample (c), but in the q range of the *(21)* reflex sample (c) has the highest scattering intensity of the three samples.

Again these experimental observations can be accounted for in a qualitative manner by our form factor model. This is shown in Fig. 6.5b, where the form factor $|F(q)|^2$ is plotted for three values of the film thickness t (1, 2, and 3nm) in a pore of radius R = 4 nm for fixed values of the scattering length densities of the core liquid ($\rho_1 = 3.7 \cdot 10^{10}$ cm^{-2}), surfactant film (ρ_2 = 1.65

$\cdot 10^{10}$ cm^{-2}), and matrix ($\rho_3 = 3.7 \cdot 10^{10}$ cm^{-2}). It is seen that at $q = q_{10}$ the value of $|F(q)|^2$ decreases in a systematic way with decreasing film thickness.

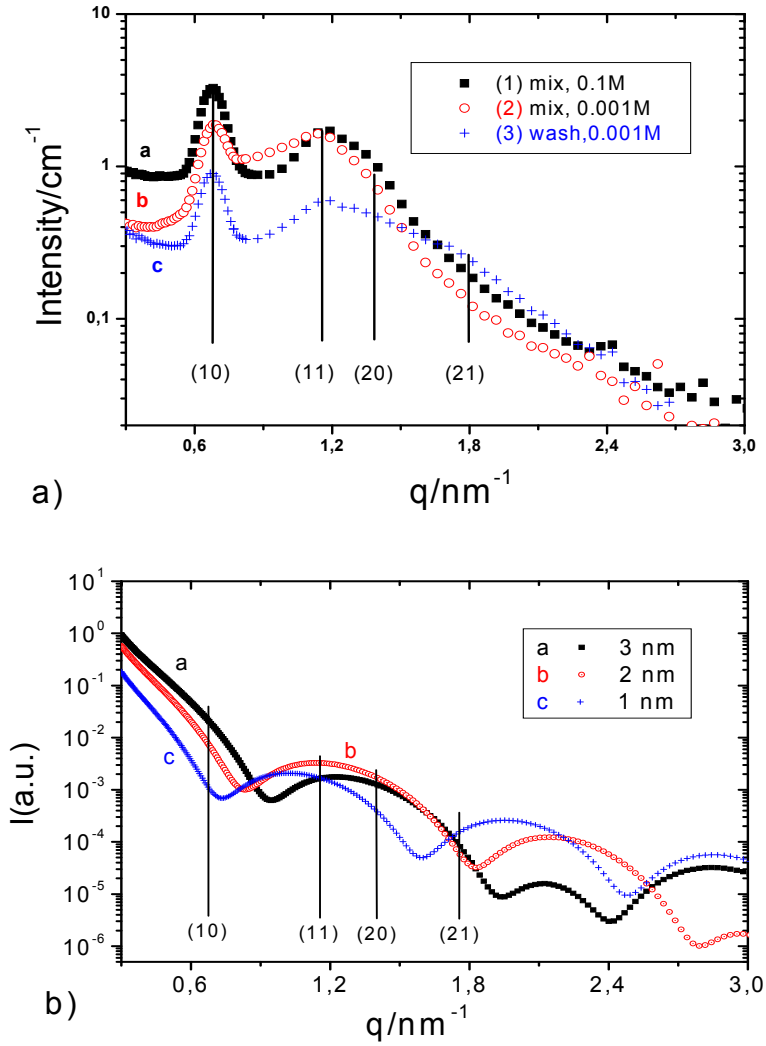

Fig. 6.5. (a) SANS curves from SBA-15 with adsorbed surfactant films in contrast-matching H_2O/D_2O (solvent C): CPCl at 0.1 M KCl (curve a), CPCl at 10^{-3} M KCl (curve b), and DPCl at 10^{-3} M KCl (washing type; curve c); (b) Form factor calculation with film thickness 3, 2 and 1 nm film thickness.

In the q range of the (*11*) and (*20*) reflexions $|F(q)|^2$ is of similar magnitude for films of thickness 3 and 2 nm, but significantly smaller for a film of 1 nm thickness, while in the q range of the (*21*) reflexion the smallest film thickness leads to the highest value of $|F(q)|^2$. All these findings are in qualitative agreement with the observed effects of the film thickness on the scattering intensities in the q regions of the Bragg reflexes.

Values of the film thickness t ranging from 1 to 3 nm, as adopted in the above model calculation, imply rather pronounced differences in the amount of adsorbed surfactant. For CPCl, a limiting adsorption $\Gamma_m \approx 5$ μmol m^{-2} (corresponding to 3 molecules/nm^2) is reported on a flat silica surface at pH 9 and high ionic strength (0.1 M KCl) [Golo97], but considerably lower values of Γ_m were found for the adsorption between two glass/solution interfaces at separations below 10 nm [Loka04]. Whereas on flat surfaces the surfactant can form a symmetric bilayer film, geometrical restraints in cylindrical nanopores will cause asymmetric bilayers in which the number of molecules in the inner layer is less than that in the outer layer. A relation between the adsorption Γ_m and the film thickness t in cylindrical pores can be obtained on the basis of the volume and mean cross-sectional area of the surfactant molecules, and an ad-hoc relation for the fraction of molecules accommodated in the inner layer as a function of pore radius R and film thickness t. With such a model one finds that film thicknesses of 1, 2 and 3 nm correspond to Γ values of ca. 1, 2 or 3 μmol m^{-2}, with the volume fraction of water in the adsorbed layer decreasing from ca. 55% for the lowest film thickness to ca. 35% at the highest film thickness. Preliminary measurements of the adsorption isotherm of CPCl in our SBA-15 sample at pH 9 give $\Gamma_m = 2.5 \pm 0.5$ μmol m^{-2} at high ionic strength (0.1 M KCl). Accordingly, the film thickness can be expected to be indeed about 3 nm for sample (a) and significantly lower for samples (b) and (c), as the in the model calculation shown in Figure 6.5.

Modelling the overall scattering curves. To represent the entire scattering curves $I(q)$ of the surfactant-loaded SBA-15 samples, the diffuse scattering $I_{diff}(q)$ caused by the silica matrix has also to be modelled. As SBA-15 consists of particles of submicrometer diameter, Porod scattering $I_P(q)$ from the outer surface of the particles will be dominant in the q range well below q_{10}, and diffuse scattering $I_D(q)$ due to micropores and other inhomogeneities of the matrix will contribute in a q range extending to well above q_{10}. Such contributions from frozen fluctuations induced by a random field can be represented by a Lorentzian square term [Lin94, Sche05]. Hence the overall diffuse scattering is modelled as

$$I_{diff}(q) = I_P(q) + I_D(q) = \frac{A_P}{q^4} + \frac{A_D}{\left(1+\xi^2 q^2\right)^2} \tag{6.5}$$

where ξ is the correlation length of the fluctuations. Fig. 6.6a shows how the overall scattering curve of a sample can be modelled by an incoherent superposition of the contributions of Eq

6.5 with Bragg scattering with an appropriate choice of the model parameters (ξ = 0.9 nm, A_D = 0.9 cm^{-1}, A_P = 0.1 ·10^{26} cm^{-5}, and δ = 0.12 nm^{-1}).

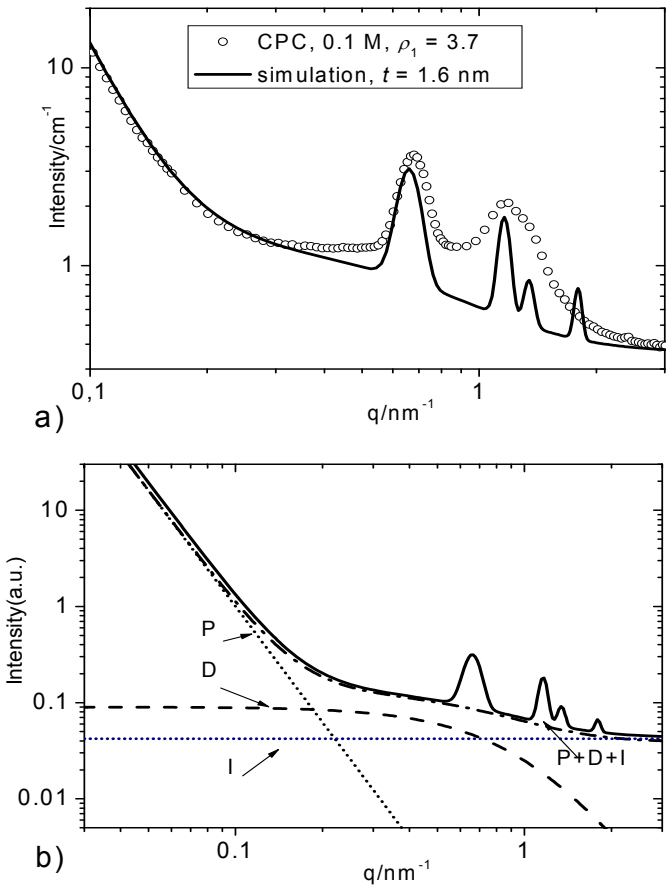

Fig. 6.6. Analysis of SANS data for CPCl in SBA-15 (0.1 M KCl): (a) Experimental data (open circles) and simulation (full line); (b) Individual contributions to the model function (Eq.6.5): (P) particle surfaces (Porod); (D) diffuse scattering of the matrix; (I) incoherent scattering; the full line shows the sum of all contributions plus Bragg scattering.

Comparison of the resulting function $I(q)$ with the experimental scattering curve for SBA-15 with an adsorbed surfactant film (Fig. 6.6b) indicates that the main features of the experimental data can be represented reasonably well by this formalism. However, several important details have not been taken into account in the present analysis, e.g., the effect of the wavelength distribution of the neutron beam, effects resulting from the lattice disorder (displacement of the pore centres from their ideal positions) and possible further contributions to the diffuse scattering which are not represented by the Lorentzian square term.

Summary

The present study shows that neutron small-angle scattering offers a useful tool for studying the organisation of surfactant layers adsorbed in the cylindrical pores of periodic mesoporous silica such as SBA-15. In the experimental q range the scattering curve is dominated by Bragg peaks resulting from the ordered arrangement of the mesopores in the silica matrix. The intensities of the individual Bragg reflexes are strongly affected by the surfactant adsorption and by the solvent contrast. The observed behavior can be understood by modelling the pore by the form factor of a core-shell cylinder. As the form factor exhibits pronounced minima in the q range of the Bragg reflexions, the intensity of the Bragg peaks can vary in a systematic way with the thickness of the adsorbed film. The overall scattering curve of the SBA-15 samples can be modelled by adding appropriate terms for the Porod and diffuse scattering of the matrix and the incoherent scattering resulting from the aqueous solvent. A major drawback of small-angle neutron scattering is the broad wavelength distribution, which implies that only the first Bragg reflex of SBA-15 is resolved while the higher Bragg reflexes appear as a combined peak. On the other hand, the possibility to study the surfactant films in different contrast conditions by using H_2O/D_2O mixtures of different scattering length density, greatly helps to verify the chosen model.

6.2 Results at higher instrumental resolution

On the basis of the preliminary study, two further series of measurements with DPCl could be realized with enhanced instrumental resolution. As described in section 4.3.2, the inherent wavelength distribution of the SAND instrument D16 at ILL is considerably narrower (≤ 1%) than that of V4 SANS instrument (ca. 12%) and could be further improved by setting appropriate collimation. Due to this improvement, the Bragg reflections *(11)* and *(20)* of SBA-15 loaded with DPCl could be resolved (Fig.6.7 and 6.8b). This is of importance for the data analysis, as will be explained in Chapter 7.

In the first set of measurements, SBA-15 samples of three surfactant loadings were studied in aqueous solutions of three different scattering length densities (3.7, 5.0 and 6.3 · 10^{10} cm^{-2}) at two salt concentrations (0.1 M and 0.001 M KCl). At the maximum surfactant loading (Γ_m) the three leading Bragg reflections could be observed due to enhanced instrumental resolution. In the second project, the evolution of aggregate structures in the pores could be quantitatively studied as a function of fractional filling $f = \Gamma/\Gamma_m$ in more refined steps (0.15, 0.3, 0.45, 0.6, 0.8, and 1.0). At the highest instrumental resolution four leading Bragg reflections could be observed at $f = 0.8$ and 1.0.

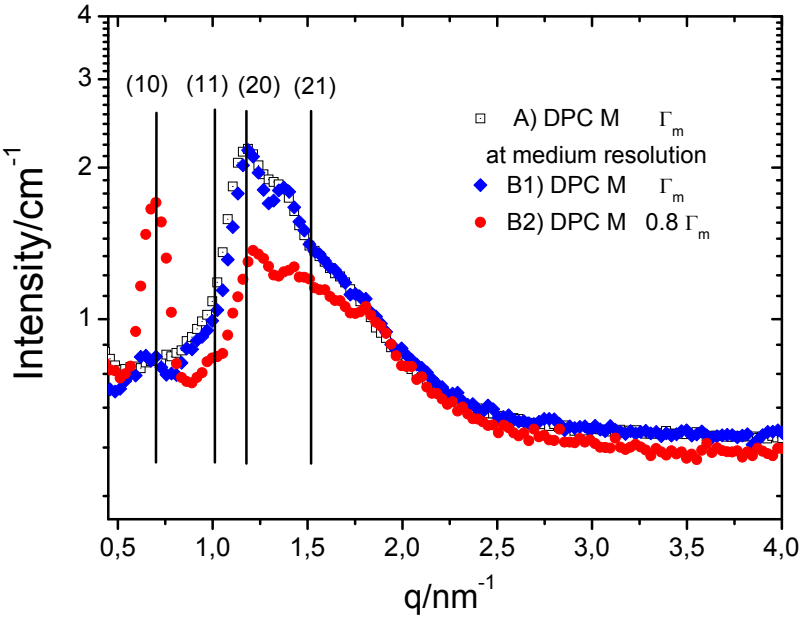

Fig. 6.7: Scattering curves of SBA-15 samples with adsorbed DPCl in contrast matching water (M) measured at medium resolution (A) and at the highest resolution (B): surfactant loading Γ_m (A and B1); 0.8 Γ_m (B2) at 1 mM KCl concentration. The positions of the four leading Bragg reflections are indicated by vertical lines.

As can be seen in Figure 6.7, the scattering curves of sample A prepared with a surfactant concentration corresponding to a loading of 2.4 μmol m^{-2} and of sample B1 prepared with a surfactant concentration corresponding to a loading of 2.0 μmol m^{-2} are almost identical, except for the q-range below q_{11}, which is attributed to the lower resolution of measurement A. We believe that in both of these measurements correspond to maximum loading of SBA-15. The excess amount of DPCl applied in the measurement A remained in the supernatant solution which was decanted. We assert that maximum loading of SBA-15 with DPCl in 0.001 M KCl corresponds to a limiting adsorption Γ_m = 2.0 μmol m^{-2}, in agreement with the TGA measurements, which yield Γ_m = 1.97 μmol m^{-2}.

Fig. 6.8 shows measurements with DPCl at medium resolution at lower salt concentration (0.001 M KCl) based on Γ_m = 2.4 μmol m^{-2}. Since the true maximum loading corresponds to Γ_m = 2.0 μmol m^{-2} the samples with 2/3 Γ_m and 1/3 Γ_m will correspond to 0.8 Γ_m and 0.4 Γ_m, respectively. As shown in Fig. 6.7 lowering the loading from 1.0 Γ_m to 0.8 Γ_m causes a drastic reduction of the intensity of the *(10)* Bragg peak.

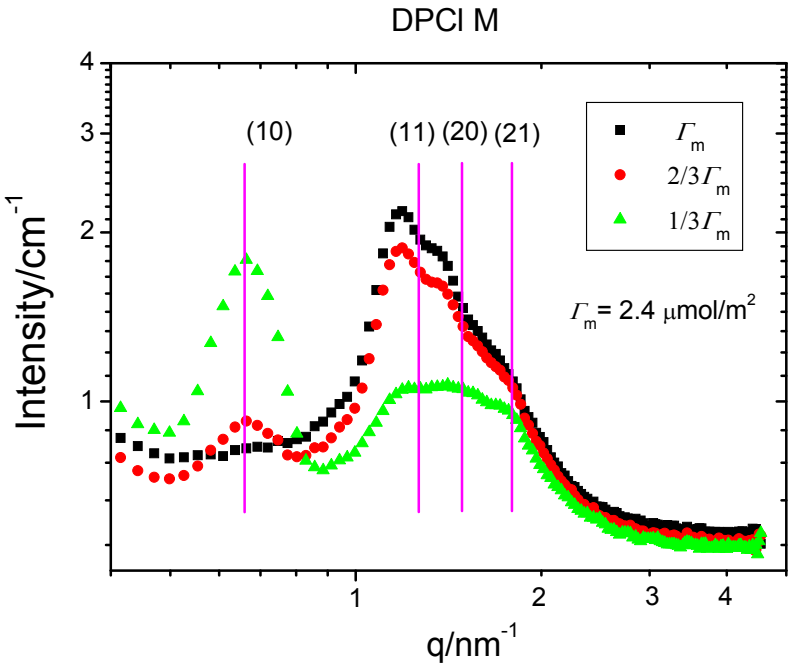

Fig. 6.8: Scattering curves of SBA-15 samples with adsorbed DPCl in contrast matching water (0.001 M KCl). Measurements performed at medium scattering resolution.

From the scattering profiles shown in Fig. 6.9 the following quantitative featured emerges as the loading with DPCl is increased: The integral intensity of the *(10)* Bragg reflection increase steadily up to $\Gamma/\Gamma_{max} \approx 0.6$ but falls off sharply as the loading is further increased to 0.8 and 1.0.

The integral intensity of the *(11)* and *(20)* Bragg reflections is very weak at relative fillings up to 0.6 but then increases sharply while the intensity of the *(10)* reflection decreases. At complete filling, the *(11)* and *(20)* peaks are very prominent while the *(10)* reflection has almost disappeared. At the highest loadings the *(21)* also becomes detectable.

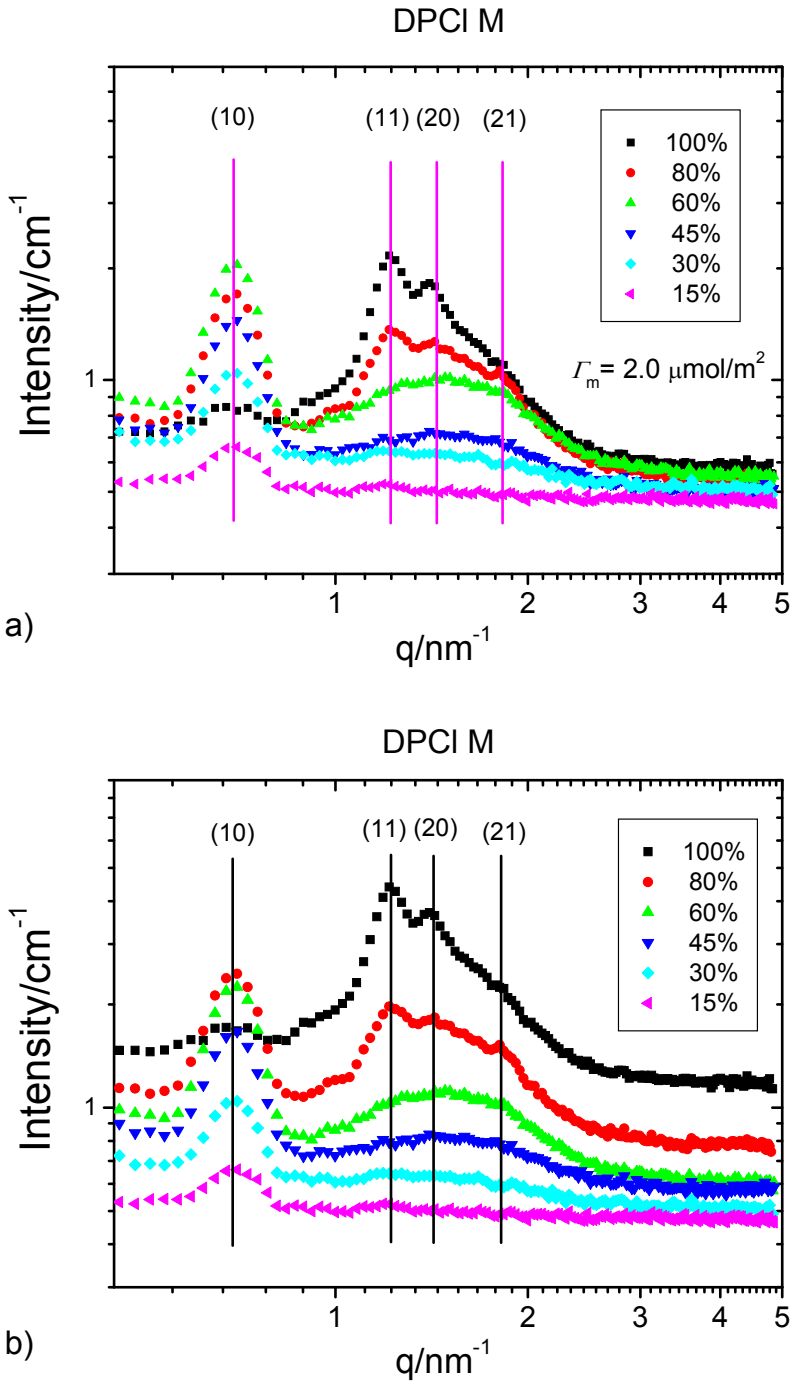

Fig. 6.9 Scattering curves of SBA-15 samples with adsorbed DPCl in contrast matching water (0.001 M KCl): a) at the highest realizable instrumental resolution at D16. In b) the intensities of the scattering curves of a) are shifted to better show their individual shapes.

In addition to the Bragg reflection there is a broad diffuse-scattering peak superimposed on the Bragg reflections *(11)*, *(20)* and *(21)*. The peak maximum of this diffuse peak gradually moves to higher q as the surfactant loading is increased. The existence of such a diffuse peak can be attributed tentatively to the formation of surfactant aggregates in the pores. This posture may implicate that at relative surfactant concentrations up to 0.6 the adsorbed surfactant does not exist in a form of a well-defined uniform layer but rather in a mixed structure of monolayer and micellar aggregates on top of the monolayer. That is, after building a monolayer of anchor molecules on the pore wall, additional surfactant molecules surface aggregates on top of those anchor molecules. This may correspond to the third stage of the well known two-step adsorption model [Atki03].

Because of the absence of Bragg reflexes of order higher than *(10)* at relative fillings up to f = 0.6, the data analysis method outlined in Section 6.1 could not be employed in that range of surfactant loadings. For the samples with filling factor f = 0.8 and f = 1.0 a modelling of the diffuse scattering on the basis of eq. 6.5 is shown in Fig. 6.10.

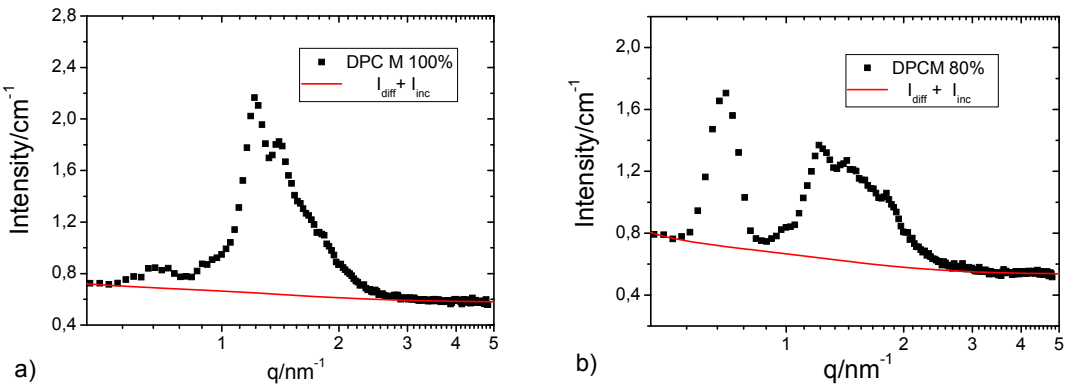

Fig. 6.10: Experimental neutron small-angle scattering curve of SBA-15 sample with adsorbed DPCl (full rectangle) and background scattering (diffuse scattering plus incoherent scattering: red line) : (a) at f = 1.0 and (b) f = 0.8.

Since the model $I_{diff}(q)$ function of eq. 6.5 is a monotonically decreasing function of q, it cannot account for the diffuse scattering peak in the q range between 1 and 2.5 nm^{-1}. In order to take care of this diffuse scattering peak, a model function with a non-monotonic $I_{diff}(q)$ is necessary. As will be explained in Chapter 7, the Teubner-Strey scattering function (eq. 7.1) gives a good account of the diffuse scattering contribution of surface aggregates of the non-ionic surfactants $C_{10}E_5$ and $C_{12}E_5$ in SBA-15. We tried to adopt this model scattering function also for the case of DPCl in the SBA-15 matrix. The fit results are presented in Figure 6.11, together with experimental scattering curves.

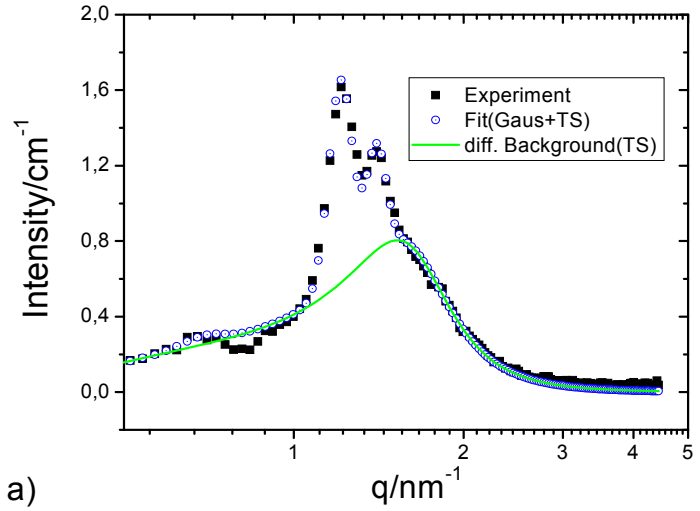

a)

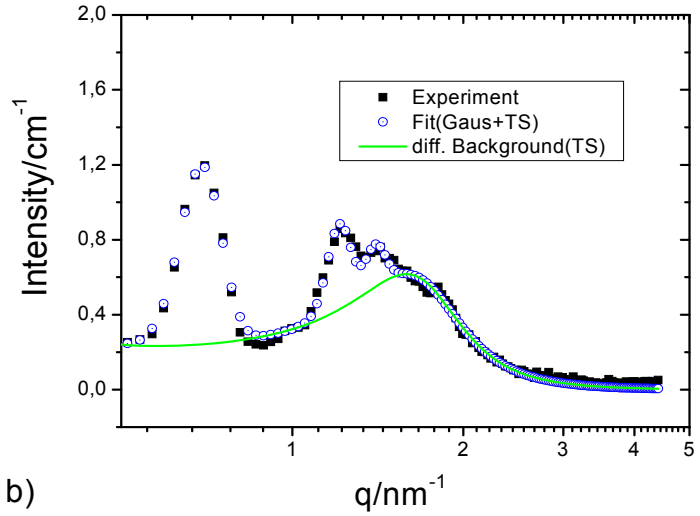

b)

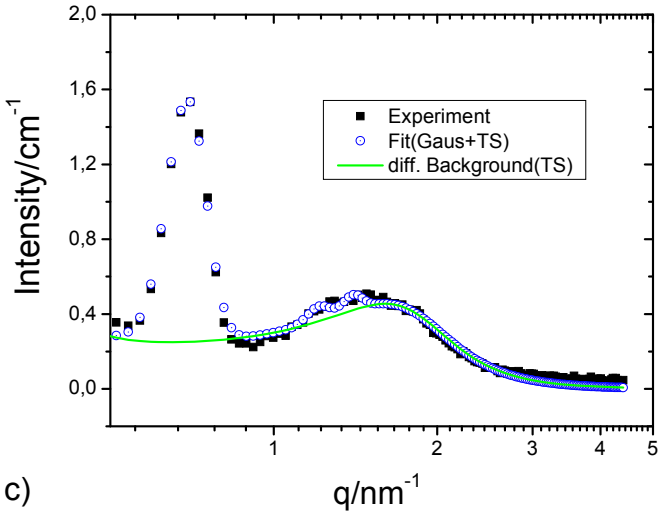
Intensity/cm-1
q/nm-1
Experiment
Fit(Gaus+TS)
diff. Background(TS)

c)

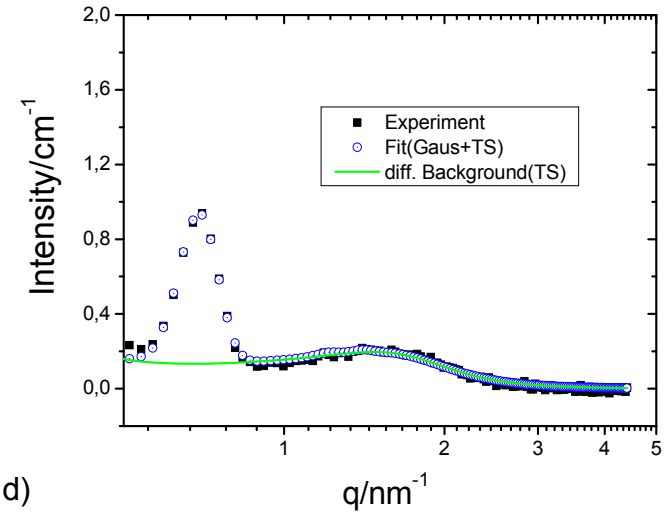
Intensity/cm-1
q/nm-1
Experiment
Fit(Gaus+TS)
diff. Background(TS)

d)

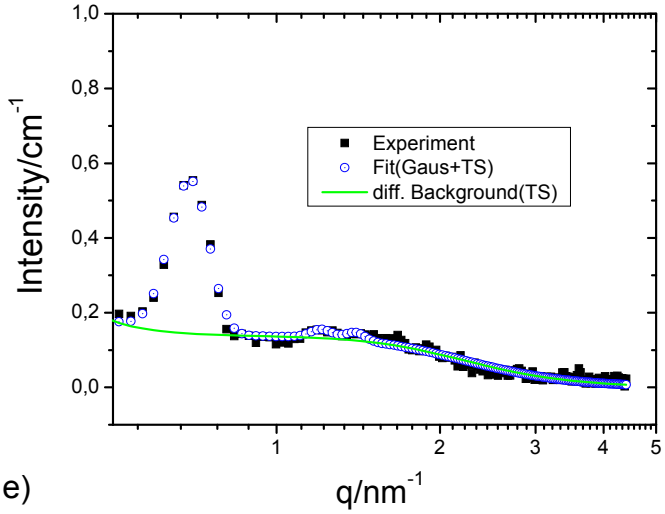
Intensity/cm-1
q/nm-1
Experiment
Fit(Gaus+TS)
diff. Background(TS)

e)

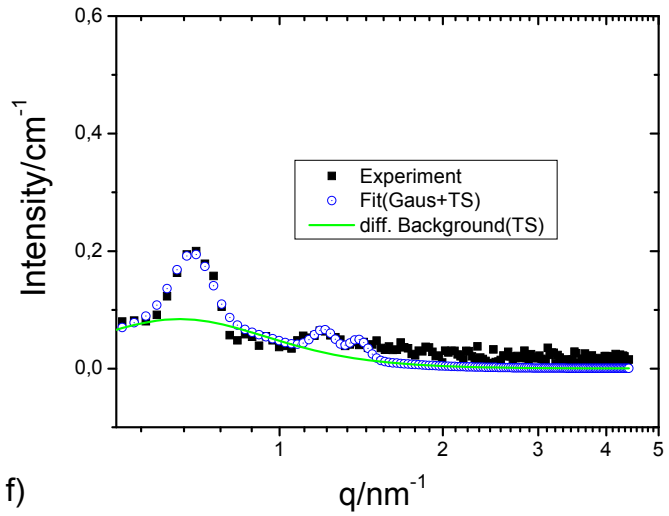

Fig. 6.11: Experimental neutron small-angle scattering curve of SBA-15 sample with adsorbed DPCl (black rectangle), fitted curve using gauss functions for Bragg peaks and modified Teubner-Strey for diffuse background scattering (blue hollow circle), and only diffuse background (green line) : a) at $f = 1.0$, b) $f = 0.8$, c) at $f = 0.6$, d) at $f = 0.45$, e) at $f = 0.3$, f) at $f = 0.15$.

Even though the entire fit function is mathematically in good agreement with the experimental scattering curve, the fit parameters r and $\Delta\rho$ resulting from the modified Teubner-Strey model function show unreasonable values. Firstly, the average film thickness $t = R - r$ at $f = 0.8$ is 2.8 nm and at $f = 1.0$ is 2.1 nm, which means a decrease in film thickness on increasing surfactant amount below maximum surface concentration. Secondly, the fit result provides a constant value of $\Delta\rho = 3.7 \times 10^{10}$ cm^{-2} for both surfactant concentrations. As the increase in $\Delta\rho$ with the filling fraction is attributed to an increasing average volume fraction of the surfactant in the layer at the pore wall, it is expected that $\Delta\rho$ also increases as the surfactant amount increases.

Both aspects contradict established adsorption behaviour as well as the successful analysis result of neutron scattering experiments on alkyl-ethoxylates in the Chapter 7 of present work. Therefore, a new model function for the diffuse scattering $I_{diff}(q)$ has still to be developed, for which the neutron scattering data of DPCl adsorbed SBA-15 samples are made available.

The incoherent background scattering SBA-15 samples with adsorbed DPCl in contrast matching solvent and D_2O are presented in Fig. 6.12. It increases almost linearly with increasing filling factor, where the samples in contrast matching water show no increase of incoherent background scattering at $f = 0.45$ and 0.8.

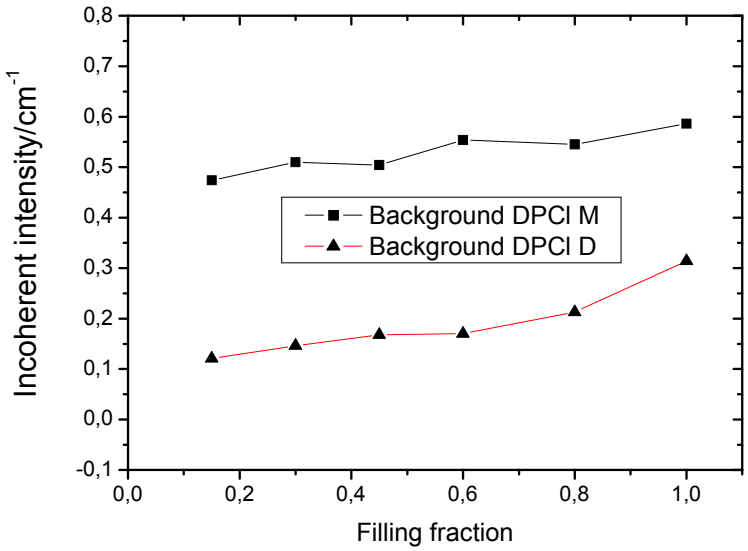

Fig. 6.12: Incoherent background scattering as a function of filling fraction: DPCl loaded SBA-15 sample in contrast-matching water (full rectangle) and in D_2O (full triangle).

Chapter 7

SANS studies of nonionic surfactants in SBA-15

This chapter presents results on the self-assembly of non-ionic surfactants (alkyl ethoxylate C_mE_n, alkyl glucoside C_mG_n) in the cylindrical pores of SBA-15 silica material obtained by Small-Angle Neutron Scattering (SANS). An analysis of the scattering data is also presented in this chapter. We start with a brief comparison of the scattering profiles of cationic and nonionic surfactants.

The surfactants investigated in the present work can be classified into three groups depending on the relative strength of interactions between surfactant head groups and silica pore wall. In the case of the alkyl ethoxylate surfactants C_mE_n (relatively strong adsorbing case) and alkyl pyridinium salt C_nPCl (very strong adsorbing case, reported in the preceding chapter), the intensity of individual Bragg peaks varies in a specific way depending on the "thickness" of the surfactant layer and the scattering length density of the aqueous solvent. In the case of the surfactants C_mG_n (weak adsorbing case), the scattering curves show significantly different behaviour compared to those of alkyl ethoxylates and alkyl pyridinium chlorides. In water/silica contrast matched samples, the Bragg reflections were either very weak (for the sample of $C_{10}G_1$) or even absent (for the sample of $C_{10}G_2$). For the SBA-15 samples with adsorbed $C_{10}G_2$, the form factor of spherical micelles could be adopted to fit the scattering data (see Fig. 7.10).

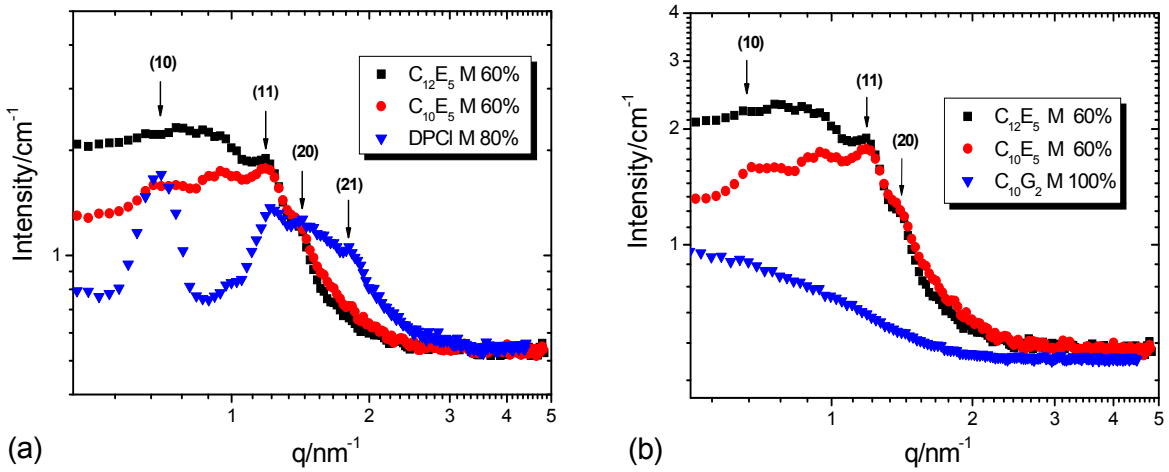

Figure 7.1: Scattering curves of SBA-15 samples in contrast-matching water: a) with adsorbed $C_{12}E_5$, $C_{10}E_5$ at a pore filling degree $f = 0.6$, and DPCl at $f = 0.8$; b) with adsorbed $C_{12}E_5$, $C_{10}E_5$ at $f = 0.6$, and $C_{10}G_2$ at $f = 1.0$. The positions of leading Bragg reflections are marked by arrows and indices.

A broad peak of diffuse but coherent scattering is observed in the scattering curves of SBA-15 with C_mE_n (Fig. 7.1), which is believed to be resulting from a non-uniform distribution of surfactant in the pore. Such a structure may result from discrete surface aggregates (surface micelles) or a patch-like structure of the surfactant aggregates or holes in the surfactant film. The position and maximum intensity of the diffuse peak change as a function of the amount of adsorbed surfactant, expressed by surfactant filling factors $f = \Gamma / \Gamma_m$. This implicates that the distance between the surfactant aggregates in the pore is changing with the amount of surfactant in the pores. For the analysis of the diffuse small angle scattering a new theoretical model was adopted as will be described in Section 7.1.

In general, the incoherent background scattering intensities of samples deliver additional information about the amount of actually adsorbed surfactant due to the hydrogen atoms in the surfactant molecules besides water. This effect is especially remarkable for the samples prepared with the contrast matching H_2O/D_2O solvent mixture, because the increase in the amount of hydrogen atoms depends then mainly on the amount of adsorbed surfactant in this case.

Two members of the family of alkyl pentaoxyethylene monoether surfactants with different length of alkyl chains but the same head group ($C_{12}E_5$ and $C_{10}E_5$) and three members of the alkyl glucoside surfactant family sugar ($C_{10}G_1$, $C_{10}G_2$ and $C_{12}G_1$) are investigated to study the surfactant adsorption in the SBA-15 material depending on the chain length as well as on the type of the head group.

7.1 Alkyl poly(oxyethylene) mono ether surfactants

The both alkyl ethoxylates $C_{10}E_5$ and $C_{12}E_5$ are known to form elongated aggregates such as ellipsoidal or wormlike micelles in the bulk solution, but they have somewhat different values of the packing parameter due to their different tail length [Patr97]. Therefore, qualitatively similar but quantitatively different adsorption behaviours are expected for these non-ionic surfactants in the pores of SBA-15. The samples with these surfactants were prepared according to the protocol for DPCl (section 6.2) and also measured with the instrument D16 at ILL.

In the scattering curves, the changes in the structure and shape of these surfactant aggregates can be qualitatively observed as a function of surfactant amount. For the SBA-15 samples loaded with the non-ionic surfactants $C_{12}E_5$ (Fig.7.2) and $C_{10}E_5$ (Fig.7.3), a unique morphological development of aggregates in the pores was observed.

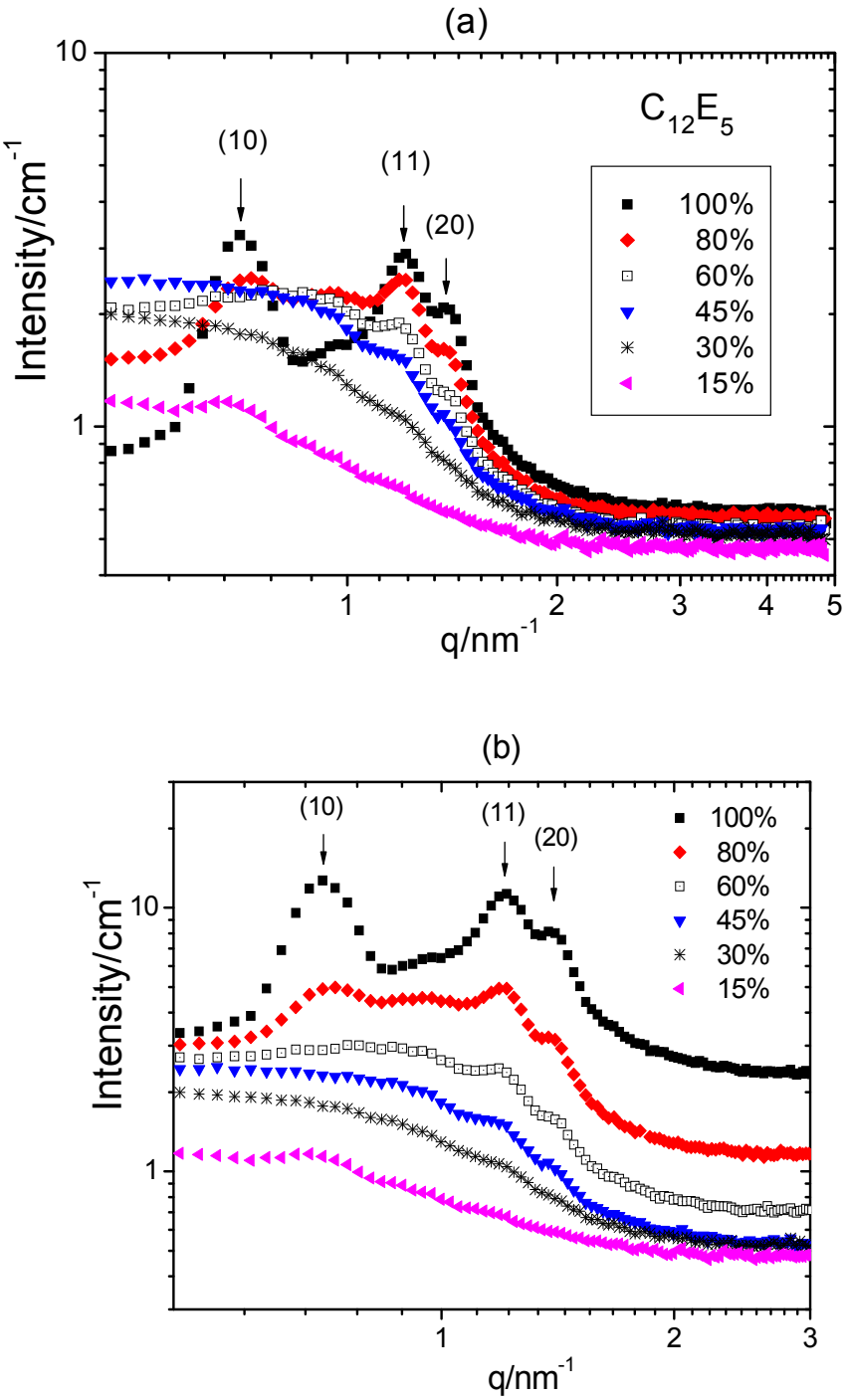

Figure 7.2 Scattering curves of SBA-15 samples loaded with $C_{12}E_5$ in contrast matching H_2O/D_2O at a series of filling fraction *f*. The positions of three leading Bragg peaks are marked by arrows and indices. In b) the intensities of the scattering curves in a) are shifted to better show their individual shapes.

The most significant features of the scattering profiles are the low intensity of the *(10)* reflection in general with exception of the pore filling degree $f = 1.0$ in the case of $C_{12}E_5$ and the pronounced diffuse scattering at the pore filling degrees around $f = 0.6$ in the q-range of three leading Bragg reflections. These features are caused by two different aspects of the surfactant self-assembly in the pores: decoration of the pore walls by some adsorbed surfactant aggregates almost built up to a layer (which causes the Bragg reflections), and the appearance of discrete surfactant aggregates at a preferred distance from each other (indicated by the peak in the diffuse scattering).

Up to a surfactant loading of 60%, the scattering curves of the contrast-matched SBA-15 samples with adsorbed $C_{12}E_5$ do not show the apparent *(10)* Bragg reflection except for $f = 0.15$ (just a hump around the position of *(10)* Bragg peak).
The behaviour of scattering profiles at low q ($q < 0.1$ nm^{-1}) is completely different from that of SBA-15 samples with adsorbed cationic surfactants C_nPCl. The profile for $f = 0.6$ exhibits a maximum at $q \approx 0.8$ nm^{-1} and the profile for $f = 0.45$ appears to have a maximum near $q = 0.6$ nm^{-1} while the profiles at lower filling fractions are still increasing at the lower experimental q values. Above the surfactant loading of 60%, the scattering intensity decreases as q approaches 0. Simultaneously, the *(11)* and *(20)* Bragg reflections and the diffuse scattering peak become more pronounced.

For SBA-15 loaded with $C_{10}E_5$, the scattering intensities at low q ($q < 1$ nm^{-1}) are much more influenced by the *(10)* Bragg peak than $C_{12}E_5$ loaded SBA-15 samples. Up to the surfactant loading of $f = 0.45$, the *(10)* peak is the strongest among the three leading Bragg peaks. The *(11)* and *(20)* Bragg reflections and the diffuse scattering peak show similar behaviour as the SBA-15 samples loaded with $C_{12}E_5$, where the diffuse scattering contribution of $C_{10}E_5$ loaded SBA-15 samples is less impressed than that of $C_{12}E_5$ loaded SBA-15 samples.

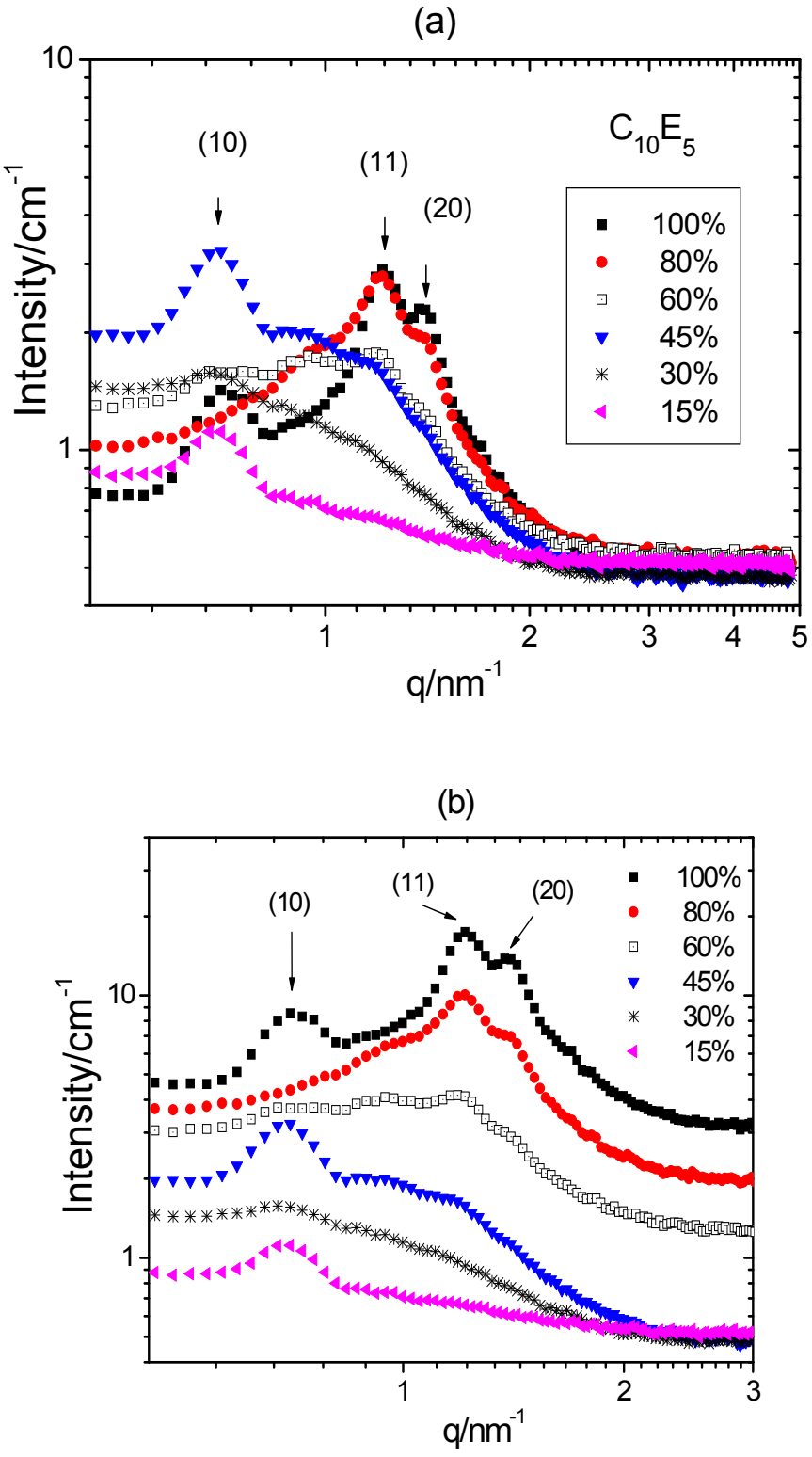

Figure 7.3: Scattering curves of SBA-15 samples loaded with $C_{10}E_5$ in contrast matching H_2O/D_2O at a series of filling fraction *f*. The positions of three leading Bragg peaks are marked with arrows and indices. In b) the intensities of the scattering curves in a) are shifted to better show their individual shapes.

Fundamentals of analysis

To analyze the scattering data of the SBA-15 samples with adsorbed $C_{10}E_5$ and $C_{12}E_5$, the formalism applied for the SBA-15 samples with adsorbed cationic surfactants (Equation 6.1 in Chapter 6) was modified by replacing the analytical function for diffuse scattering $I_{diff}(q)$. As explained above, the scattering profiles of the samples with $C_{10}E_5$ and $C_{12}E_5$ clearly exhibit a diffuse scattering peak at some filling factors, indicating a correlation of the position of the scattering centers in the sample, which indicates the formation of surfactant aggregates in the pores. Scattering profilies with such a correlation peak have been found in microemulsion systems [Teub87] and also in the late stages of spinodal decomposition of phase-seperating systems [Bind01]. The small-angle scattering behaviour of such systems can be described by a scattering function of the form

$$I_{diff} = B(q)\frac{I_0}{(1-I_0/I_m)(q^2/q_m^2-1)^2 + I_0/I_m} \tag{7.1}$$

where I_m and q_m are the coordinates of the maximum of $I_{diff}(q)$. For the Teubner-Strey scattering function [Teub87] which has been applied to microemulsion systems, the factor $B(q)$ is equal to unity. However as $I(q)$ tends to zero with $q \rightarrow 0$ for the present system, the correct behaviour of in this limit is obtained by setting $B(q) = q^4/(k+q^4)$, where k is a constant. As explained in sec. 3.2, the scattering function of Eq. (7.1) correponds to a two-particle density correlation function exhibiting a damped-periodic behaviour.

The quantities d and ξ are related to the experimentally accessible parameter q_m, I_m and I_0 by

$$\xi = \frac{\sqrt{2}}{q_m}\left[\frac{1}{(1-I_0/I_m)^{1/2}} - 1\right]^{-1/2} \tag{7.2}$$

$$d = \frac{2\sqrt{2}}{q_m}\pi\left[\frac{1}{(1-I_0/I_m)^{1/2}} + 1\right]^{-1/2} \tag{7.3}$$

where d represents the quasi-periodic separation of particles and ξ the range of the quasi-periodic order.

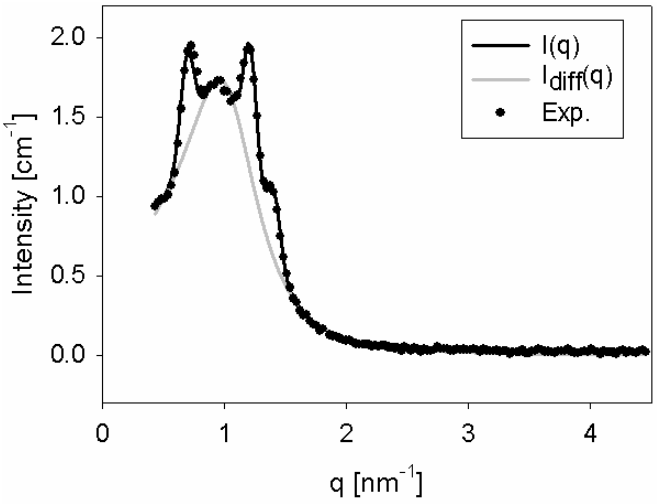

Fig. 7.4: Experimental neutron small-angle scattering curve of SBA-15 sample adsorbed by $C_{12}E_5$ at a loading of 80% (full circle), diffuse scattering (gray line) and simulated scattering curve (black line).

The experimental scattering data $I(q)$ were thus analysed on the basis of Eq. (6.1), again using the form factor of a cylindrical core-shell model (Eq. 6.4), but now adopting Eq. (7.1) for the diffuse scattering contribution $I_{\text{diff}}(q)$. A representative result of the analysis by employing the cylindrical core-shell model with Eq. (7.1) is presented in Fig. 7.4. The data analysis was performed by D. Müter (MPI of Colloids and Interfaces, potsdam-Golm) and is described in detail in his Ph. D. Thesis (Humboldt-Universität Berlin, 2010) [Müt10]. In essence, the fitting procedure allows to separate the contributions of Bragg scattering and diffuse scattering and yields two sets of parameters: (i) the integral intensities of the three leading Bragg reflection

$$\widetilde{I}_{hk} = \int I_{Bragg}(q) q^2 dq \tag{7.4}$$

for Bragg peaks hk and (ii) the parameters q_{m}, I_{m} and I_0 of Eq. (7.1). Fig. 7.5b) and 7.5d) shows the dependence of the integral Bragg intensities $\widetilde{I}_{hk}$ on the filling fraction for the case of in SBA-15. The dependence of the parameter q_{m} and of the intensity ratio I_0/I_{m} on the filling fraction is shown in Fig. 7.5a).

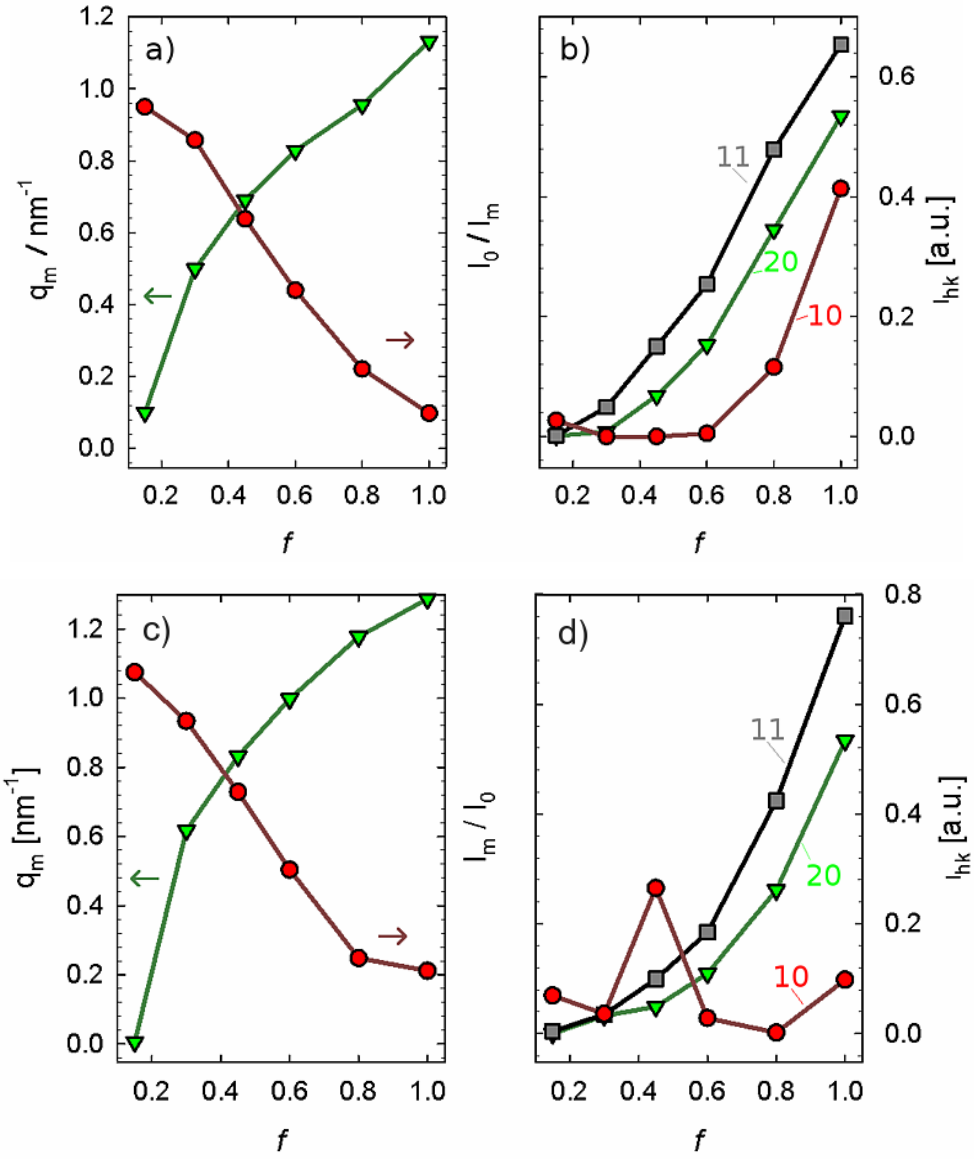

Fig. 7.5 Parameters q_m, I_0/I_m, and $\widetilde{I}_{hk}$ are presented as a function of filling fraction: a) and b) $C_{12}E_5$, c) and d) $C_{10}E_5$ loaded SBA-15 sample in contrast-matching water.

The position of q_m shifts to higher q value as the pore is filled with surfactant. The intensity parameter I_0/I_m decreases with increasing f (Fig. 7.5). From Equations 7.2 and 7.3, this implies a decrease in the interparticle separation d and an increase of the correlation length ξ with increasing f as shown in Figure 7.6.

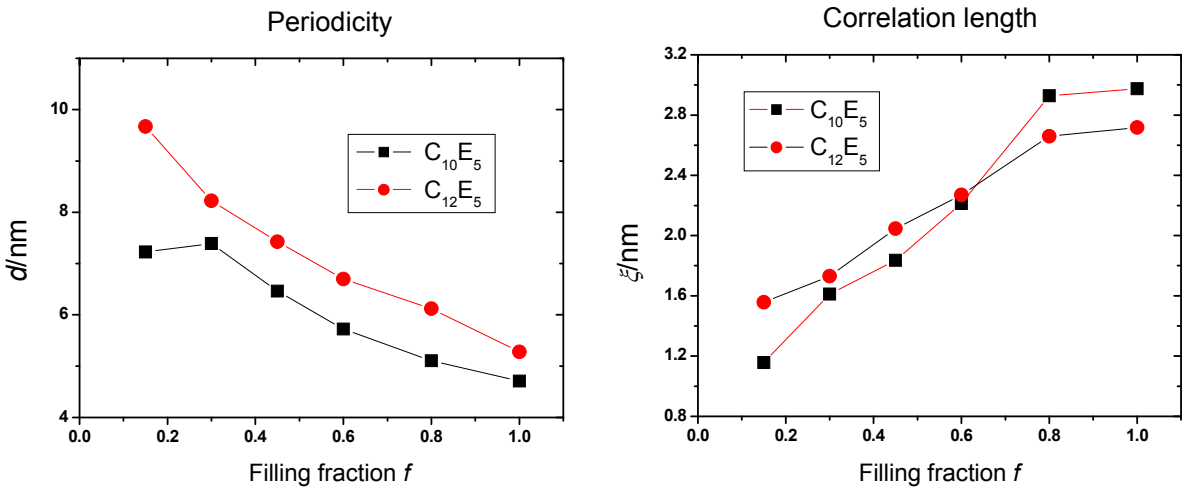

Fig. 7.6: The average distance d (periodicity) between the surfactant aggregates in the pore (left) and the respective correlation length ξ (right) are presented as a function of filling fraction: $C_{10}E_5$ loaded SBA-15 sample in contrast-matching water (black rectangle) and in $C_{12}E_5$ (red circle).

The correlation length ξ of the quasi-periodically arranged surfactant aggregates increases with increasing filling fraction, viz. from $\xi \approx 1.5$ nm at $f = 0.15$ to $\xi \approx 2.8$ nm at $f = 1$[6]. This implies that the surfactant aggregates are weakly correlated at low filling degrees but rather highly correlated at high filling degrees.

From the integral Bragg intensities $\tilde{I}_{hk}$ the parameter r (inner radius of surfactant layer) and ρ_1 (scattering length density of surfactant layer) were extracted for fixed values of the pore radius R and scattering length density of the matrix, ρ_0. From these, the thickness $t = R - r$ and scattering length density increment $\Delta\rho = \rho_0 - \rho_1$ of the surfactant layer were obtained. At low filling factors where the Bragg reflections are very weak (see Figures 7.2 and 7.3), the error limits on t and $\Delta\rho$ are large. At higher filling fractions ($f \geq 0.6$) the error bars are much lower and meaningful values of t and $\Delta\rho$ are obtained.

The increase in $\Delta\rho$ with the filling fraction is attributed to an increasing average volume fraction of the surfactant in the layer at the pore wall. The thickness of film for $C_{12}E_5$ increases monotonous (Fig. 7.7 right) as f increases. For $C_{10}E_5$, however, the film thickness increases not until $f = 0.45$, which implicates that the surfactant film begins to build at higher surfactant loading than $C_{12}E_5$ due to weaker interaction between the surfactant $C_{10}E_5$ and silica pore wall.

[6] Values of ξ / d in the range from 0.25 to 0.5 are reported for microemulsion systems in the bulk phase[Teub87].

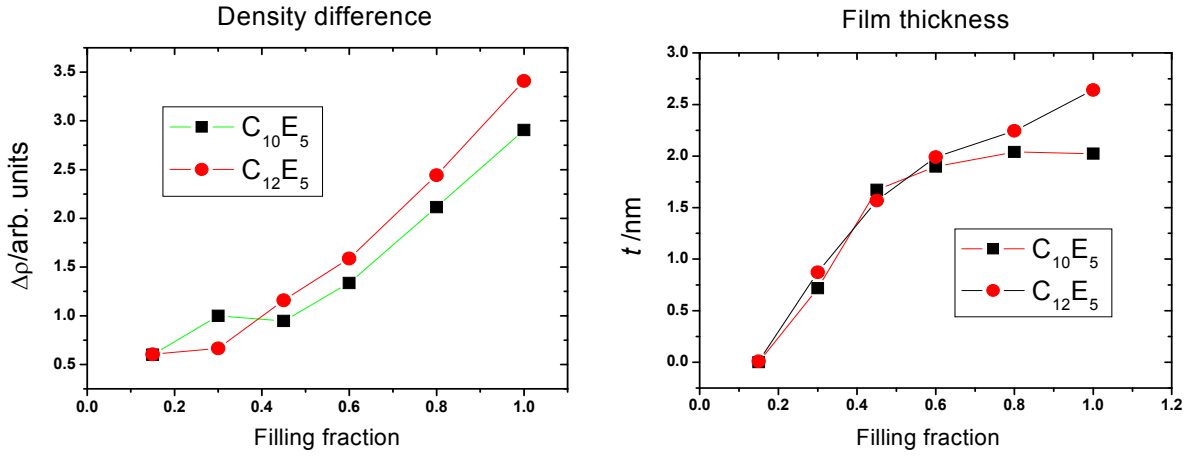

Fig. 7.7: The scattering density difference between the surfactant aggregates in the pore (left) and water/silica and the film thickness (right) are presented as a function of filling fraction: $C_{10}E_5$ loaded SBA-15 sample in contrast-matching water (black rectangle) and in $C_{12}E_5$ (red circle).

In Figure 7.8, the constant incoherent background scattering intensity is presented as a function of filling fraction *f* for both surfactants. For the surfactant $C_{12}E_5$, the incoherent background increases almost monotonously as expected. The non-monotonous behaviour in the case for the surfactant $C_{10}E_5$ may be due to experimental artifacts.

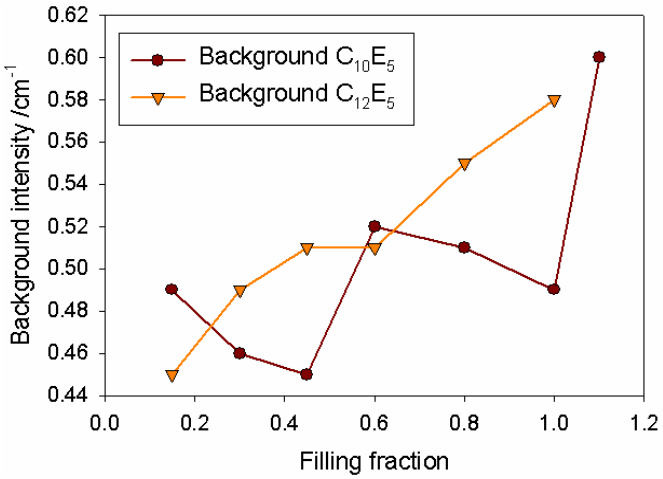

Fig. 7.8: Incoherent background scattering as a function of filling fraction: $C_{10}E_5$ loaded SBA-15 sample in contrast-matching water (black full circle) and in $C_{12}E_5$ (red full triangle).

In conclusion, the results and analysis in this section have shown that adsorption of the surfactant in the cylindrical pores of SBA-15 can proceed via the formation of a layer of surface micelles at the pore walls. This conclusion is based on the following observations (i) the existence of distinct surfactant aggregates in the pores follows from the finding that the diffuse scattering exhibits a correlation peak that moves to higher q as the pore filling increases. From the scaling of the inter-aggregate distance $z = d / d_{\min}$ with the pore filling f one finds that the size of the surfactant aggregates is constant over the entire pore filling range. (ii) The intensities $\widetilde{I}_{hk}$ of the leading Bragg peaks and their dependence on f clearly show that the surfactant aggregates are forming a film at the pore wall. The film thickness t derived from this analysis is compatible with oblate ellipsoidal surface micelles of thickness 2.8 nm. Hence the information derived from the diffuse scattering and the intensities of the Bragg peaks is complementary in the sense that the former proves the existence of distinct aggregates and the latter indicates the formation of a film, which leads to the conclusion that adsorption in the pores proceeds via the formation of a layer of distinct surface micelles at the pore walls.

7.2 Alkyl glucoside and alkyl maltoside surfactants

The head groups of alkyl glucoside (C_nG_1) and alkyl maltoside (C_nG_2) surfactants are strongly hydrated in water and form micelles of spherical or ellipsoidal shape in aqueous solution [Lipf07, Möll99]. On the other hand, it is known that these surfactants sparingly adsorb on to the silica surface from the aqueous solution. With the surfactants $C_{12}G_1$, $C_{10}G_1$ and $C_{10}G_2$, the influence of alkyl chain length for identical head group ($C_{12}G_1$ and $C_{10}G_1$) as well as the influence of head group for identical alkyl chain ($C_{10}G_1$ and $C_{10}G_2$) on adsorption behaviour can be effectively compared.

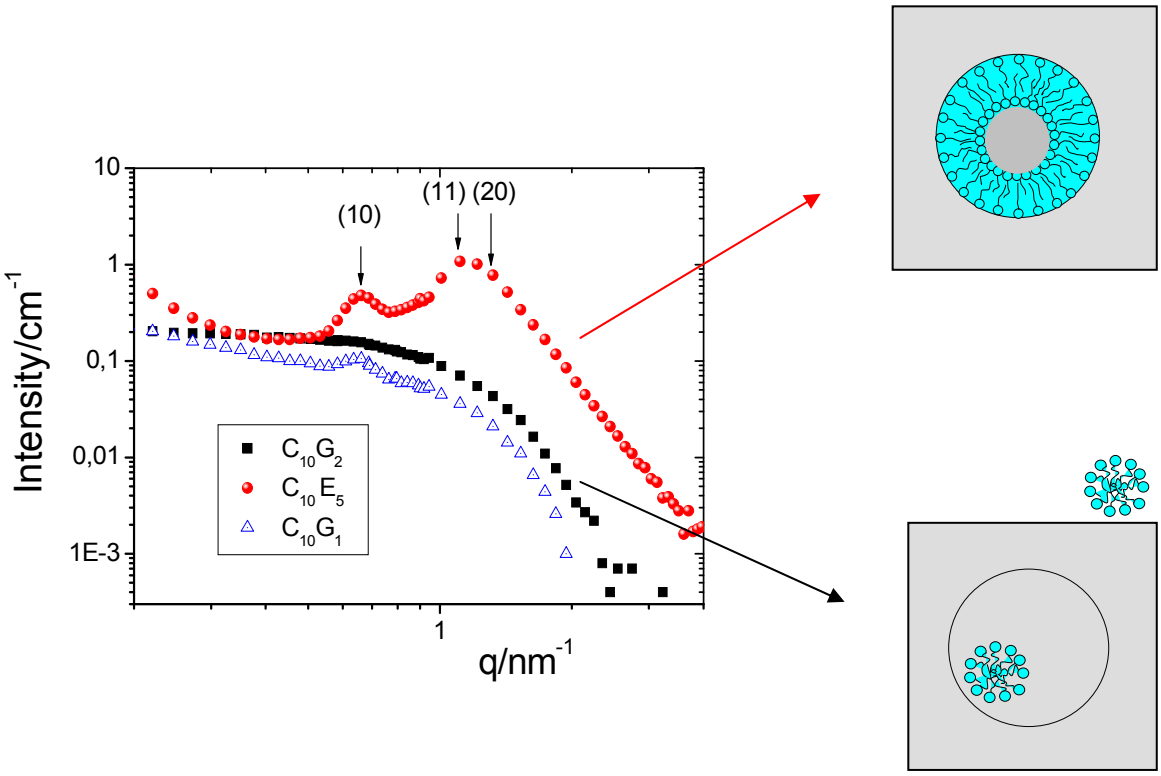

Figure 7.9: Comparison of the scattering curves of SBA-15 with three different adsorbed surfactants ($C_{10}E_5$, $C_{10}G_2$ and $C_{10}G_1$) in contrast matching H_2O/D_2O against the silica matrix.

In the preparation of the samples for SANS measurements with $C_{10}G_1$ and $C_{10}G_2$ it was assumed, that the plateau value of the adsorption isotherm (Γ_m) of these surfactants in SBA-15 were 0.5 μmol/m^2 ($C_{10}G_1$) and 1.0 μmol/m^2 ($C_{10}G_2$). Later the TGA measurements showed, however, that these values were much too high (see Section 5.3). Due to this fact a large part of

the surfactant was not adsorbed but remained in the supernatant, which was not transferred into the sample cell. Accordingly, the amount of surfactant in the sample cells was significantly lower than in the measurements with $C_{10}E_5$ and $C_{12}E_5$, and can be estimated only indirectly, as explained later.

In Figure 7.9, the scattering curves of SBA-15 samples loaded with $C_{10}G_2$ (full rectangle) and $C_{10}G_1$ (hollow triangle) are compared with that of a SBA-15 sample with adsorbed $C_{10}E_5$. The scattering profile of $C_{10}E_5$ in SBA-15 (full circle) exhibits the features discussed in Section 7.1 which indicates a layer of surfactant aggregates adsorbed on the pore wall. The scattering profile of the SBA-15 sample with adsorbed $C_{10}G_2$ exhibits a fundamentally different behaviour. It does not exhibit any prominent Bragg reflections, which implicates that no adsorbed surfactant layer is formed on the pore wall. Instead, the scattering curve has characteristic features of a solution of small micellar aggregates.

The scattering profile of the SBA-15 sample with $C_{10}G_1$ shows a weak scattering contribution of 2D hexagonal lattice as a hump at the position of *(10)* Bragg reflection, which appears to be superposed on the scattering function of an elongated surfactant aggregates in solution.

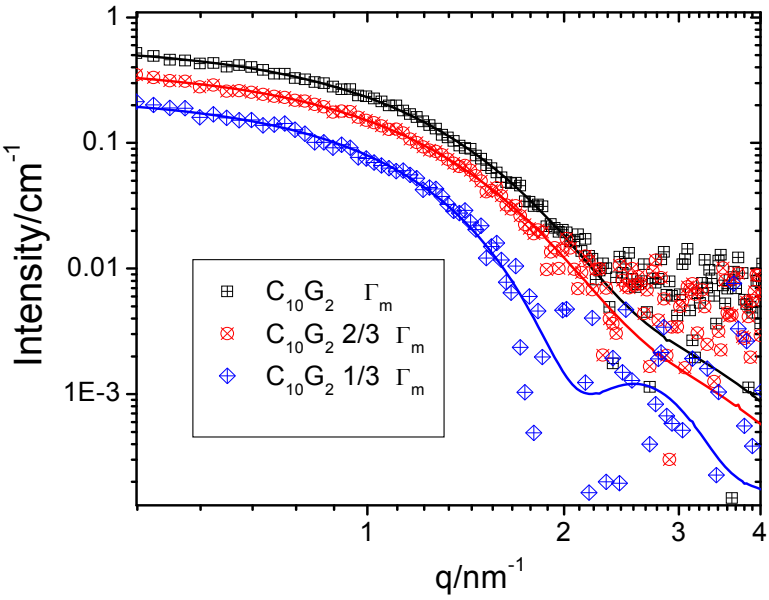

Figure 7.10: Scattering curves of SBA-15 with three different loadings of surfactant $C_{10}G_2$ (solid lines are corresponding fit functions).

The scattering curves of SBA-15 samples with three different loadings of $C_{10}G_2$, corresponding to 1/3 Γ_m, 2/3 Γ_m and Γ_m are shown in Figure 7.10. The incoherent background scattering was subtracted for further analysis, which causes in logarithmic presentation a strong noise in data statistics at high-q range. The scattering curves can be represented by the form factor of spherical micelles. The fit parameters are given in Table 7.1. The fit results (Table 7.1) suggest that the surfactant molecules at the lowest concentration of 1/3 Γ_m appear to assemble to a bigger number of aggregates than at higher concentrations at almost the same size.

Γ/Γ_m	s	Vol. fraction f_p /%	R_0/nm
1/3	0.24	0.96	1.58
2/3	0.24	0.97	1.55
1	0.23	1.00	1.55

Table 7.1 Fit results (SASfit ©) of SBA-15 with three different loadings of surfactant $C_{10}G_2$ the fit functions of which are presented as solid lines in Figure 7.10. R_0 is radius of micelles in the log-normal distribution with volume fraction f_p as a fit parameter and s is polydispersity of aggregates.

A question which arises is, whether the micelles are situated in the pore or in the solution outside the silica particles. This question was addressed by D. Müter in a simulation based on a two-dimensional model of 2025 circular pores on a hexagonal pore lattice, assuming contrast-match between the matrix and the pores[7]. Circular 'micelles' were introduced into the pores chosen at random, so that any pore can contain between 0 and 3 micelles. The scattering profile was calculated for the situations when 100, 200, 500 or 1000 micelles were accommodated in the pores. It was found that the *(10)* Bragg reflection can be detected when 200 micelles were present, the *(10)* and *(20*) reflections were detectable with 500 micelles, and the four leading Bragg peaks were clearly seen with 1000 micelles (Fig. 7.11).

[7] Private communication.

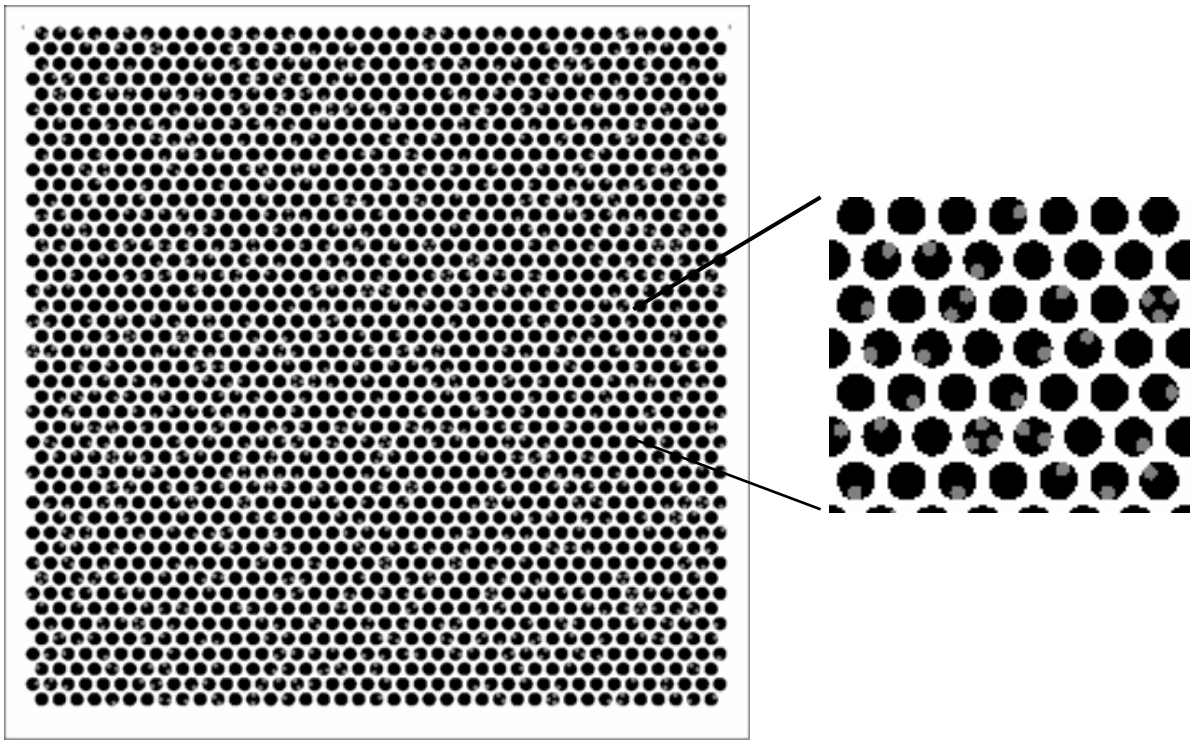

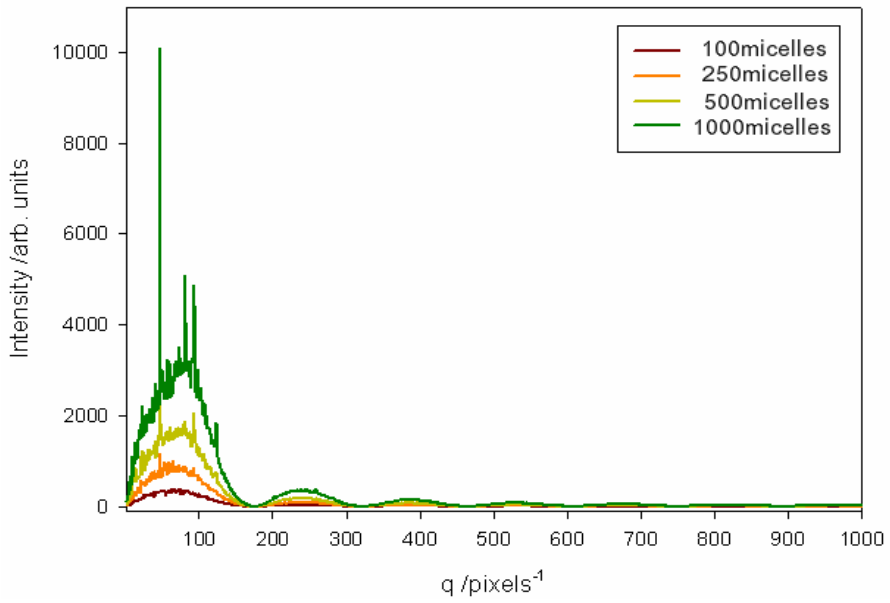

Figure 7.11: a two-dimensional model of 2025 circular pores on a hexagonal pore lattice (upper graphic) with an inset of enlarged pores and a simulation based on it, assuming contrast-match between the matrix and the pores (lower graphic).

To assess the significance of this simulation for a three-dimensional system, we consider that the micelles have a diameter $d = 0.25\ a_0$, where a_0 is the lattice constant and thus the 2D simulation corresponds to a strip of a 3D pore lattice of thickness $L \approx 0.3\ a_0$. Accordingly, the volume of the simulation box is $V \approx A^2 L = 608\ a_0^3$, and thus the volume fraction of micelles

$\Phi_M = N \cdot v_M / V$, where $v_M = (\pi/6) \cdot d^3$ is the volume of a micelle and N the number of micelles. Thus we find $\Phi_M = 0.02$, 0.04, 0.11, and 0.20 for $N = 100$, 200, 500, and 1000.

Experimental scattering curves of SBA-15 samples with adsorbed $C_{10}G_2$ do not show any Bragg reflections. Thus, through an analysis of the water amounts in and outside of the SBA-15 silica pores, it was attempted to investigate the local distribution of $C_{10}G_2$ micelles in surfactant loaded SBA-15 slurry.

Sample	**Wet SBA-15 loaded with surfactant/*mg***	**Water/*mg***	**Silica/*mg***
$C_{12}E_5$ Γ_m (M)	151	98	30
$C_{12}E_5$ Γ_m (D)	156	103	31
$C_{10}E_5$ Γ_m (M)	155	101	31
$C_{12}E_5$ 0.6 Γ_m (M)	153	108	25
$C_{10}E_5$ 0.6 Γ_m (M)	157	111	29

Table 7.2. Analysis of water content in slurry-samples of SBA-15 loaded with the non-ionic surfactants $C_{12}E_5$ and $C_{10}E_5$. The mass fraction of silica and surfactant in the SBA-15 sample was taken from TGA measurement.

The amount of water in the SBA-15 slurry samples used in the SANS measurements with $C_{12}E_5$ and $C_{10}E_5$ was determined by transferring the samples to a glass container which was weighed before and after drying in a slightly evacuating oven at 80 °C. By combining the result of this analysis with the TGA results, it was found that on average the SANS cells contained ca. 30 mg SBA-15 and 100 – 110 mg water, depending on the loading with surfactant (Table 7.2). Since the SBA-15 sample used in these measurements has a specific pore volume of ca. 1 cm^3/g (Table 4.1), the maximum mass of water in the pores can be ca. 30 mg and the rest (70 – 80 mg) will be in the space between the SBA-15 particles. The mass fraction of surfactant in the samples loaded with $C_{10}G_2$ was ca. 13 % at maximum loading, corresponding to ca. 4 mg, or to a volume fraction of 4 %. On the basis of the theoretical simulation discussed above one expects that the *(10)* Bragg reflection of the pore lattice should be detectable if the volume fraction of micelles in the pores is 2%, and both *(10)* and *(20)*

Bragg reflections should be detectable if the volume fraction of micelles in the pores is 4 %. The fact that no Bragg reflection can be seen for $C_{10}G_2$ (see Fig. 7.9), thus suggests that the volume fraction of this surfactant in the pores is less than 2%. This implies that the pores are depleted of surfactant. In the case of $C_{10}G_1$ the (10) Bragg reflection is detectable (Fig. 7.9), when 0.43 %wt of $C_{10}G_1$ was added in the sample preparation.

Sample	m_1/% (silica+surfactant)	m_2/% **(silica)**	m_s/% **(surfactant)**
$C_{10}E_5$ 1/3 Γ_m (5)	99.1	75.4	23.5
$C_{10}E_5$ 2/3 Γ_m (M)	99.3	60.5	38.7
$C_{10}E_5$ 3/3 Γ_m (D)	98.9	57.6	41.4
$C_{10}G_2$ 1/3 Γ_m (M)	97.2	86.7	**10.4**
$C_{10}G_2$ 2/3 Γ_m (M)	97.5	85.3	**12.2**
$C_{10}G_2$ 3/3 Γ_m (M)	98.3	85.3	**13.0**
$C_{10}G_2$ 1/3 Γ_m (D)	96.1	88.5	**7.6**
$C_{10}G_2$ 2/3 Γ_m (5)	96.6	88.4	**8.2**
$C_{10}G_2$ 3/3 Γ_m (5)	97.7	88.7	**9.0**

Table 7.3. The TGA results for the non-ionic surfactants $C_{10}E_5$ and $C_{10}G_2$ are presented, where m_1 is the mass fraction of silica and surfactant in a dry SBA-15 sample, m_2 pure silica and m_s pure surfactant.

Table 7.2 shows the amounts of surfactant-adsorbed SBA-15 slurry which has been transferred in a sample cell (second column), the amounts of water (third column) and the amount of SBA-15 (the fourth column) in it. The amount of pure SBA-15 in the cell was estimated by applying TGA results in the fourth column of Table 7.3.

Chapter 8

Summary and Outlook

In the present work, the structure and shape of surfactant aggregates adsorbed in the cylindrical mesopores of SBA-15 silica studied by SANS, the adsorption measurements of these surfactants and the TGA measurements of surfactant adsorbed SBA-15 samples were reported.

Neutron small-angle scattering method was proved to be a useful tool for studying the organisation of surfactant aggregates adsorbed in the cylindrical pores of periodic mesoporous silica such as SBA-15. Contrast matching method, a privileged advantage of neutron scattering technique, could successfully be applied for various water-surfactant-SBA-15 systems. By using contrast matching mixture of H_2O/D_2O to silica matrix, the prominent Bragg reflexes could effectively be suppressed and the structural aspects of the surfactant aggregates could be enlightened.

The influence of surfactant head group (chemical property and size) and alkyl chain length on the adsorption behaviour has been demonstrated by employing $C_{10}E_5$, $C_{10}G_1$, $C_{10}G_2$, $C_{12}E_5$, $C_{12}G_1$, dodecyl pyridinium chloride ($C_{12}PCl$), and hexadecyl pyridinium chloride ($C_{16}PCl$). These surfactants can also be classified into three groups depending on the relative strength of interactions between surfactant head groups and silica pore wall. In the case of the alkyl ethoxylate surfactants C_mE_n (relatively strong adsorbing case) and alkyl pyridinium salt C_nPCl, the intensity of individual Bragg peaks varies in a specific way depending on the thickness of the surfactant layer and the scattering length density of the aqueous solvent. In the case of the surfactants C_mG_n (weak adsorbing case), the scattering curves show significantly different behaviour compared to those of alkyl ethoxylates and alkyl pyridinium chlorides. In water/silica contrast matched samples, the Bragg reflections were either very weak ($C_{10}G_1$) or even absent ($C_{10}G_2$). For the SBA-15 samples with adsorbed $C_{10}G_2$, the form factor of spherical micelles was successfully applied to fit the scattering data.

Scattering profiles of $C_{10}E_5$ and $C_{12}E_5$ adsorbed SBA-15 samples, obtained at contrast-matching conditions between the aqueous solvent and the silica matrix could be represented

quantitatively by an analytical scattering function (modified Teubner-Strey function) for the diffuse small-angle scattering superimposed with Bragg reflections from the pore lattice. These two contributions provides complementary information about the self-assembly of the surfactant in the pores: diffuse scattering indicates the formation of surfactant aggregates at preferred distances from each other and analysis of the Bragg peaks shows that a layer of surfactant is formed at the pore walls. These findings suggest that adsorption of the surfactant starts by formation of discrete surface aggregates, which increase in number and later merge to interconnected patches as the plateau of the adsorption isotherm is approached.

In the case of SBA-15 samples with adsorbed cationic surfactants (DPCl and CPCl), the intensities of the individual Bragg reflexes are also strongly affected by the surfactant adsorption and by the solvent contrast. The observed behaviour could be qualitatively understood by modelling the pore by the form factor of a core-shell cylinder. As the form factor exhibits pronounced minima in the q range of the Bragg reflections, the intensity of the Bragg peaks can vary in a systematic way with the thickness of the adsorbed film. But the form factor of a core-shell model combined with the Teuber-Strey function for diffuse scattering could not be applied for the analysis of SBA-15 samples with adsorbed cationic surfactant.

The adsorption isotherms of the cationic surfactants DPCl and CPCl in SBA-15 silica were measured using depletion method. Other than in the case of silica nanoparticles OX50, the adsorption of both surfactants did not show any significant dependence on the electrolyte concentration and the alkyl chain length.

By employing TGA measurement, the maximum amount of surfactant adsorption in SBA-15 could independently be checked. The TGA results were referred for the discussion, whether the $C_{10}G_2$ micelles may be located in or outside the pores.

In outlook, further investigation about the influence of solvent scattering length density on surfactant adsorption and development of an appropriate model function for the scattering curves of cationic surfactant loaded SBA-15 samples would be a challenging and pioneering work. Also, a more systematic combination of TGA measurement with the neutron scattering data would help check the actual amount of adsorbed surfactant in the SBA-15 sample and thus enable more reliable analysis of surfactant aggregate structure and shape.

Appendix

A.1 Adsorption isotherms of non-ionic surfactants

Adsorption isotherms of $C_{10}G_2$ and $C_{10}E_5$ in SBA-15 silica have been measured at two different temperatures (25°C and 45°C) by Anton Eltekov in our group and the plateau values of them were adopted from this measurement for sample preparation of present work. For $C_{12}E_5$, Jens Meissner recently has measured an adsorption isotherm in SBA-15 using surface tension measurement and was shown in Section 5.2.

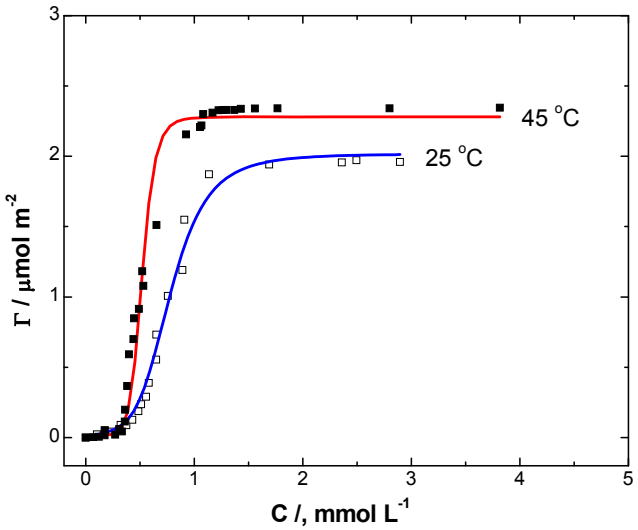

$C_{10}E_5$ in SBA-15

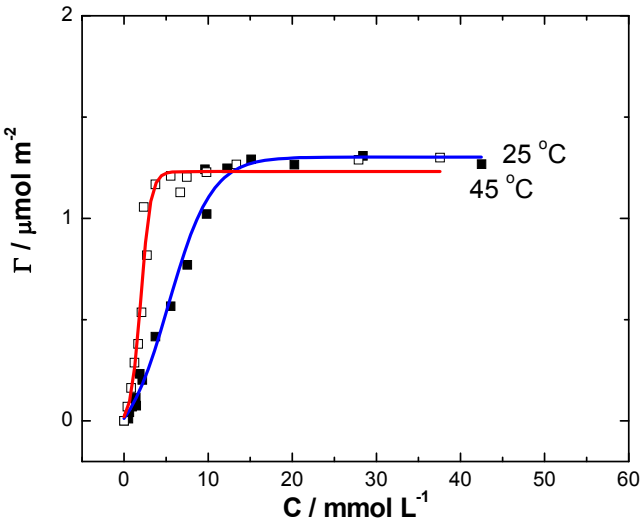

$C_{10}G_2$ in SBA-15

A.2 Series of SANS Measurements

In this section the SANS measurements performed during this Ph.D. project are documented with respect to the specifications of instrument and details of preparing procedure of the samples. Two separate projects of SAND experiments with different experimental conditions have been performed at two large facilities, namely at BENSC (V4) and ILL (D16), over a period of four years. To deliver an overview of all the measurements, the SAND experiments are presented after the proposal number. The scattering curves of SBA-15 samples which are not presented in Chapter 6 and 7 are documented under the corresponding project here.

A.2.1 V4 Series

Four proposals have been granted and performed at V4 instrument of BENSC, HMI. With respect to the choice of surfactant and the realization of contrast scheme, the whole investigation program could be constructively developed during these experimental sessions. Among them, the experiment "CHE-04-1140" did not yield useful results probably due to changed alignment in the collimation unit.

CHE04-0935

The experiments performed during this beam time had exploratory character to verify whether the surfactant molecules would build aggregates at the pore wall of SBA-15 samples or adsorb strongly onto the wall to build layer like structures. After determining the composition of contrast-matching mixture of H_2O/D_2O for SBA-15 silica, surfactant was added to the contrast matching water for adsorption in SBA-15. Lower loadings of surfactant were then realized by equilibrating the surfactant-adsorbed SBA-15 powder with known amounts of water.

CHE04-1011

In this project the influence of the surfactant head group and the dimension of pore on the surfactant self assembly in the pores was investigated. The dependence of surfactant head group size and shape on the adsorption and self-assembly in the silica mesopores was studied with three non-ionic surfactants of equal alkyl chain length, yet with different head groups in their size and chemical property, viz. decyl penta (ethylene glycol) ($C_{10}E_5$), decyl glucoside ($C_{10}G_1$) and decyl maltoside ($C_{10}G_2$). To study the effect of the pore size, i.e., the curvature of pore wall, specific surface area and the pore volume, SBA-15 materials of two slightly

different pore diameters were investigated using SANS by adsorbing the same surfactant ($C_{10}E_5$) from contrast-matching water at the surfactant concentration corresponding to Γ_m. As can be expected, the SBA-15 sample with a larger pore diameter shows slightly stronger incoherent scattering intensity ($0.022 \cdot 10^{10}$ cm^{-2}, Figure A.1a), which can be attributed to the amount of adsorbed surfactant.

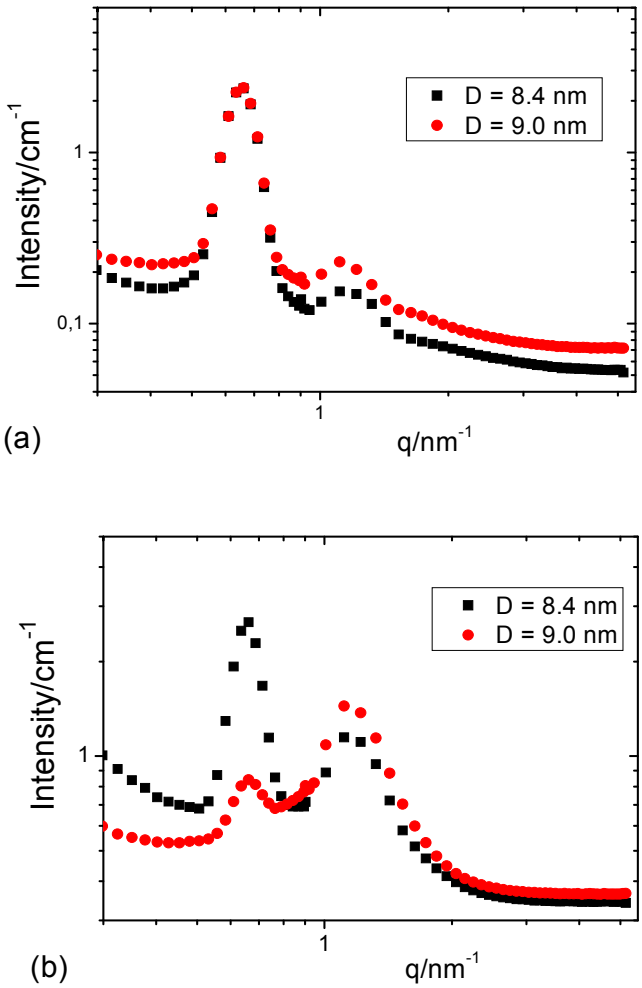

Figure A.1: SBA-15 materials of two different pore diameters were engaged: (a) adsorbed with surfactant $C_{10}E_5$, solved in contrast matching water and (b) immersed in D_2O without surfactant.

As is shown in Figure A.1a, the SBA-15 samples immersed in pure D_2O exhibit different incoherent scattering intensities viz. $0.073 \cdot 10^{10}$ cm^{-2} (SBA-15 of 9.0 nm diameter) and $0.054 \cdot 10^{10}$ cm^{-2} (SBA-15 of 8.4 nm diameter). This difference in incoherent scattering intensity of $0.019 \cdot 10^{10}$ cm^{-2} between these two samples can be associated to larger pore volume v_p = 1.362/cm^3 g^{-1} of the SBA-15 sample with 9 nm diameter compared to those of 8 nm SBA-15 sample (v_p = 1.036/ cm^3 g^{-1} and specific surface area a_s = 882/m^2 g^{-1}).

When the SBA-15 silica is adsorbed with surfactant $C_{10}E_5$, increases the overall scattering intensity even in contrast matching water. Further, for the SBA-15 sample with 9.0 nm diameter, the adsorption of surfactant reverses the behaviour of intensity between *(10)* and *(11+20)* Bragg peaks. As reported in Chapter 6 and 7, this is a typical indication for the adsorption of layer like aggregates on the wall.

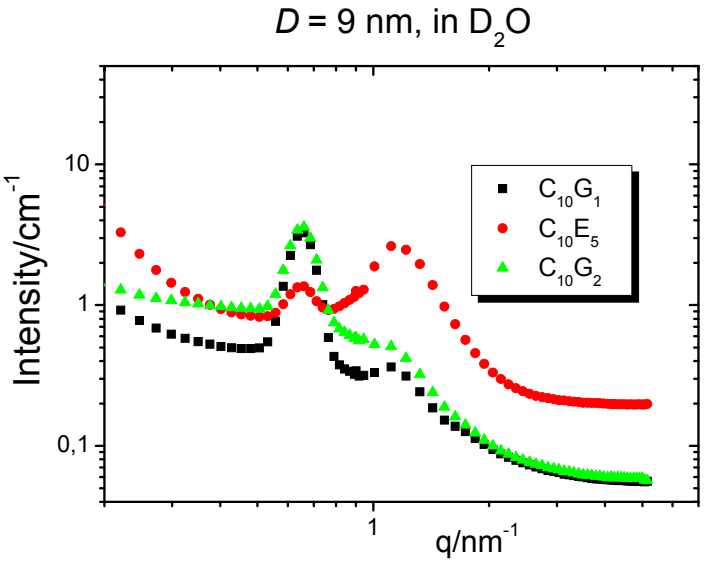

Figure A.2: Scattering curves of SBA-15 (D = 9 nm) with three different adsorbed surfactants ($C_{10}E_5$, $C_{10}G_2$ and $C_{10}G_1$) in D_2O.

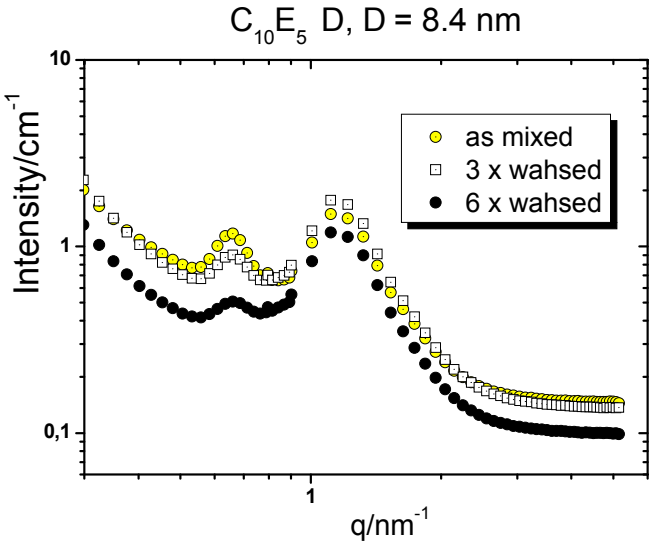

Figure A.3: Scattering curves of SBA-15 (D = 8.4 nm) with adsorbed $C_{10}E_5$ in D_2O at three different loadings emulated by washing protocol.

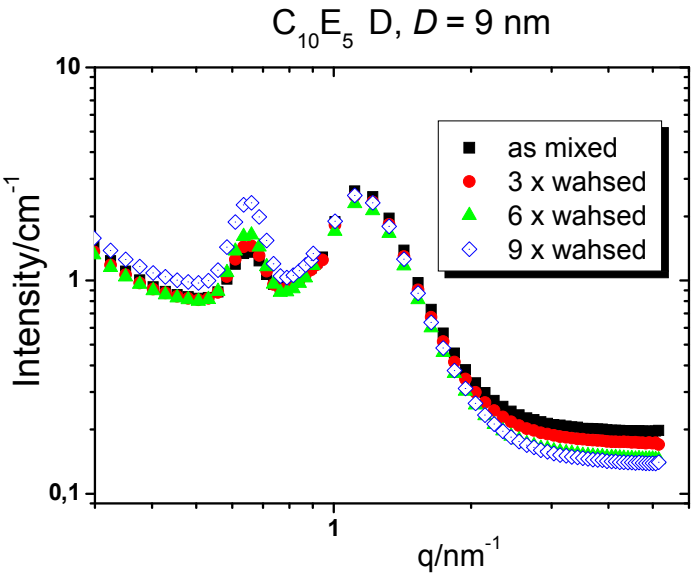

Figure A.4: Scattering curves of SBA-15 (D = 9 nm) with adsorbed $C_{10}E_5$ in D_2O at four different loadings emulated by washing protocol.

Three scattering curves of the SBA-15 samples with adsorbed the surfactant $C_{12}G_1$ are shown in Figure A.5. This surfactant adsorbs very sparingly in SBA-15, so that a broad peak around q = 2.5 nm^{-1} is presumably from solid $C_{12}G_1$ and not a Bragg peak from SBA-15.

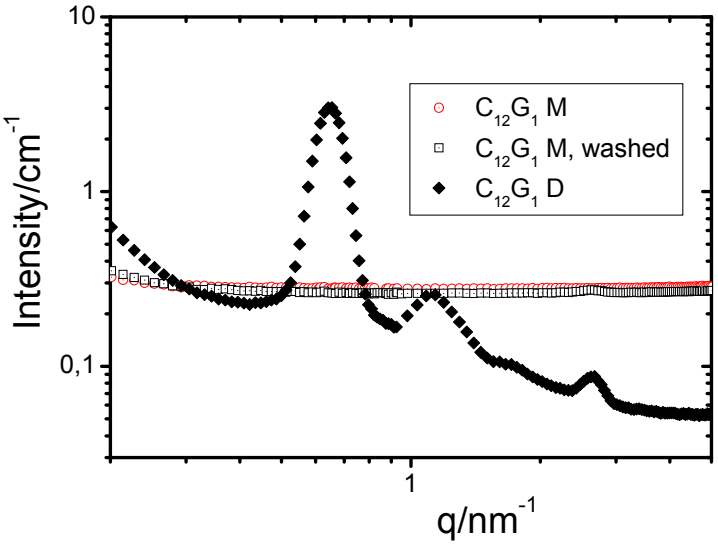

Figure A.5: Scattering curves of SBA-15 with adsorbed surfactant $C_{12}G_1$ in waters of two different scattering length densities (M: contrast-matching water, D: D_2O). Appropriate amount of water with the same SLD was applied again after decanting the supernatant of "as mixed" sample to prepare the "washed" sample.

The scattering profiles of “as mixed” sample and “washed” sample show simply an angle-independent incoherent background without any scattering contribution by structure- or form factor. Further, the minimal difference in incoherent background scattering intensity between them gives us additional information that the surfactant $C_{12}G_1$ adsorbs very sparingly in the SBA-15.

CHE04-1091

As a candidate for strong adsorbing species for SBA-15 material cationic surfactants of type alkyl pyridinium chlorides were investigated. In this measurement various experimental options (three scattering length densities, two salt concentrations for cationic surfactants and variation of surfactant amount in the pore by equilibrating surfactant adsorbed SBA-15 samples with known amount of water) were tried with two cationic surfactants DPCl and CPCl.

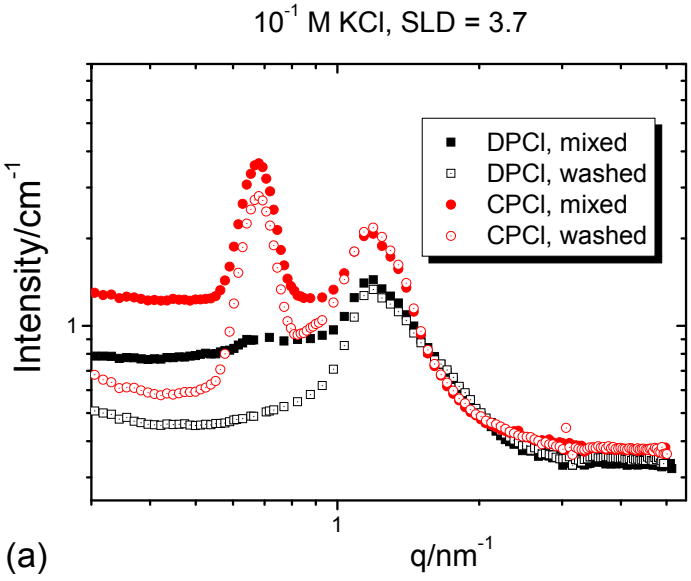

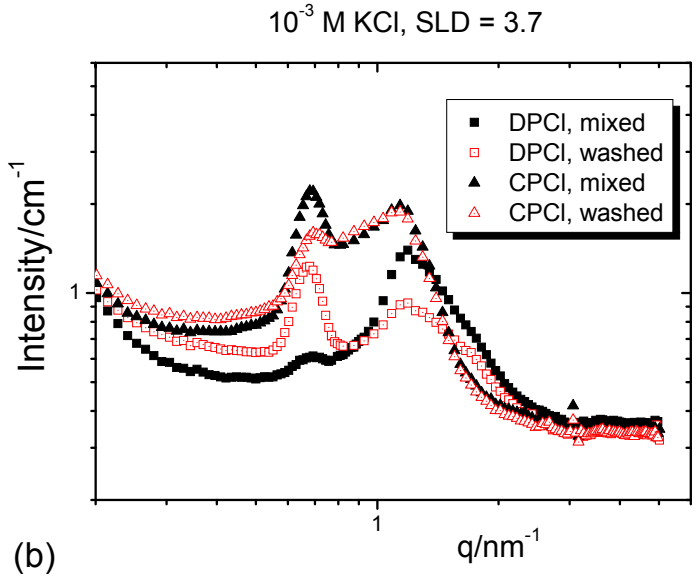
10-3 M KCl, SLD = 3.7
DPCl, mixed
DPCl, washed
CPCl, mixed
CPCl, washed
Intensity/cm-1
1
1
q/nm-1

(b)

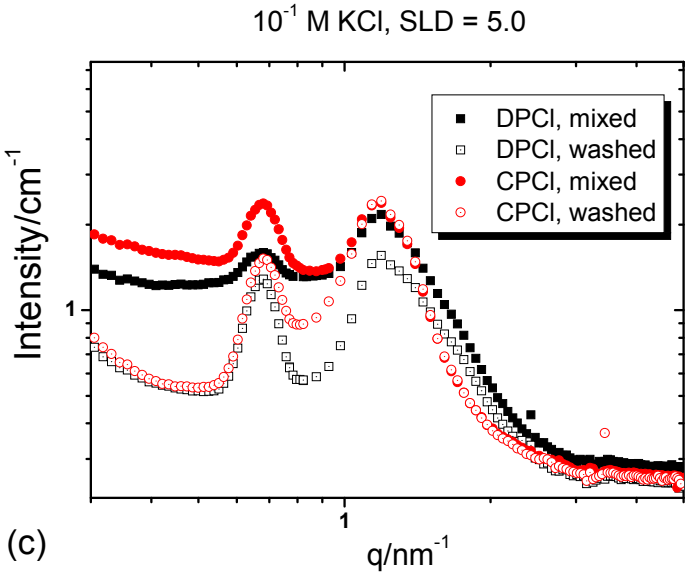
10-1 M KCl, SLD = 5.0
DPCl, mixed
DPCl, washed
CPCl, mixed
CPCl, washed
Intensity/cm-1
1
1
q/nm-1

(c)

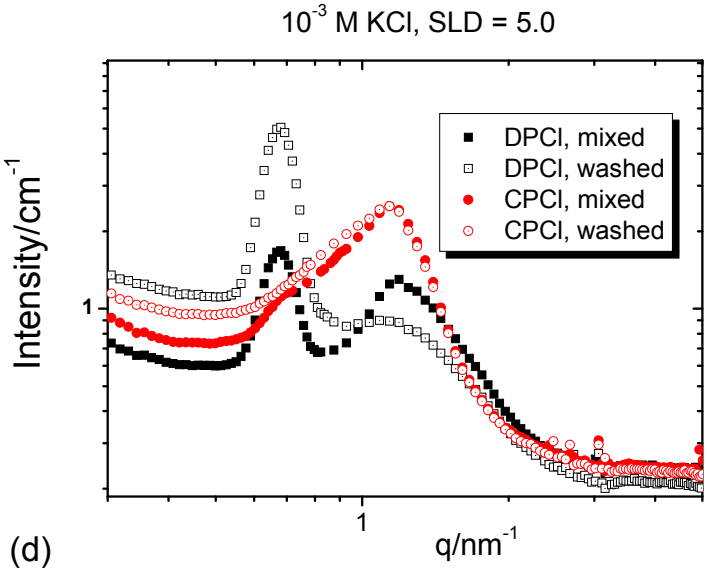
10-3 M KCl, SLD = 5.0
DPCl, mixed
DPCl, washed
CPCl, mixed
CPCl, washed
Intensity/cm-1
1
1
q/nm-1

(d)

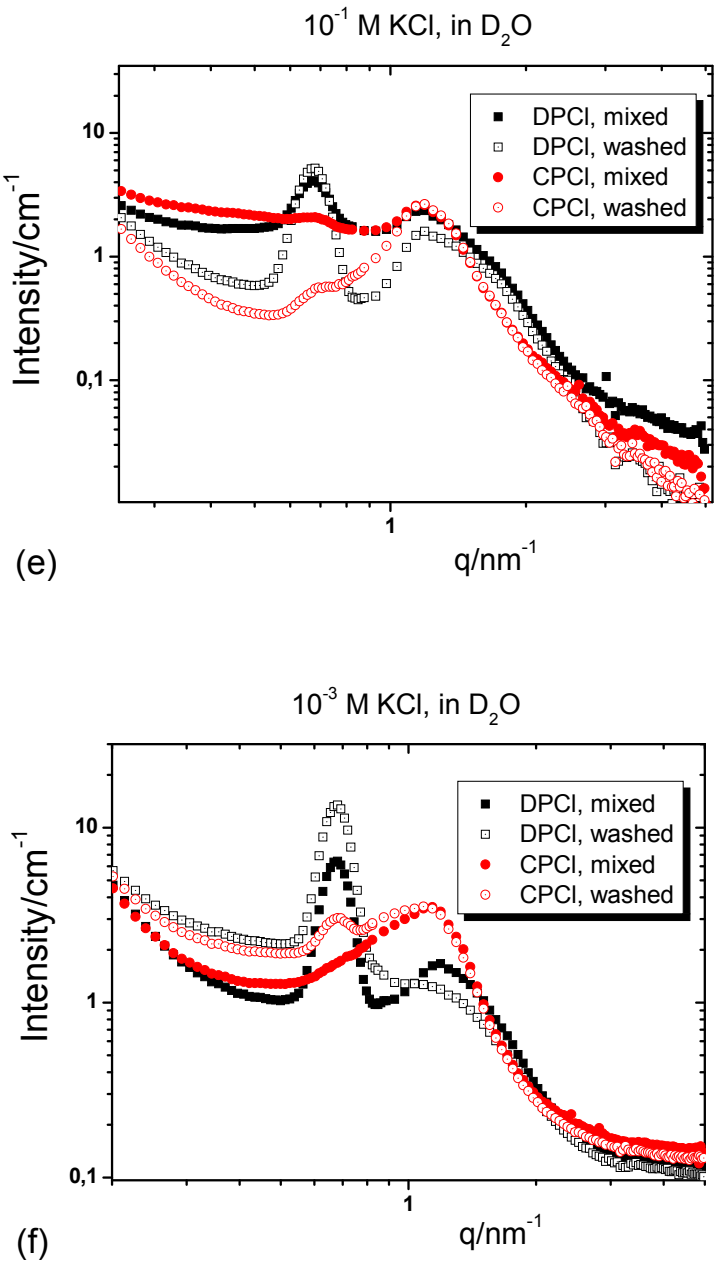

Fig. A.6 Scattering curves of SBA-15 with adsorbed cationic surfactant DPCl and CPCl at two different salt concentrations and 3 different SLDs.

CHE04-1140

To achieve better instrumental resolution a narrower collimation option for all detector distance was tried. To realize this collimator was placed at 12 m position for all detector positions. Unfortunately a systematic error in all scattering curves was observed.

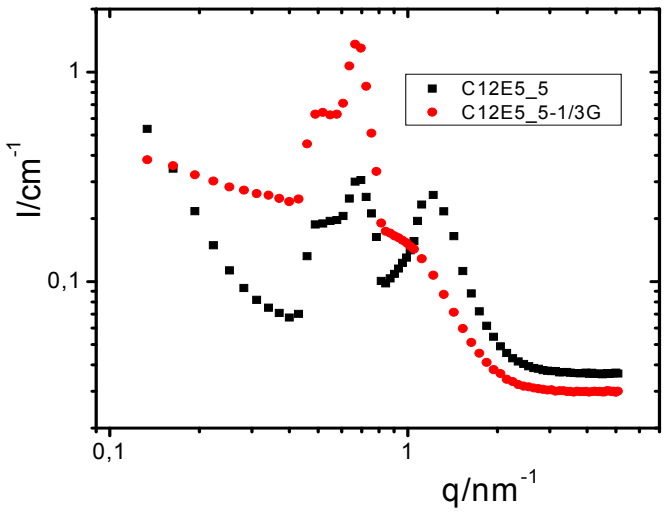

Fig. A.7: Scattering curve of SBA-15 with adsorbed $C_{12}E_5$ with deformed (10) Bragg peak. The deformation has been observed for all scattering curves systematically.

A.2.2 D16 Series

Two projects have been granted and performed successfully owing to outstanding collimation and relatively abundant neutron flux (maximum flux ~ 10^6 n.cm^{-2}.s^{-1}, if non-focussed, and ~ 8.2*10^6 n.cm^{-2}.s^{-1} when focussed at λ= 4.5 Å). In this series the advantage of D16 instrument could be fully exploited so that detailed development of surfactant adsorption in the SBA-15 at each stage of adsorption could be enlightened.

D16:9-10-847

For this series of measurement a collimation setting of 15.10 mm × 15.18 mm (slit 1) and 7.20 mm × 7.46 mm (slit 2) was used. A test experiment with a smaller collimation cross section was done at the end of beam time to check the possibility of better resolution in a reasonable measuring time (Figure 4.7).
The types of surfactants were varied in two aspects:
1) type of surfactant head groups (cationic pyridinium chloride, non-ionic ethylene oxide and maltoside)
2) alkyl chain length (C_{12} vs. C_{10})

The experimental parameters can be summarised as follows:

1) surfactants: alkyl ethoxylates ($C_{12}E_5$ and $C_{10}E_5$), alkyl maltoside ($C_{10}G_2$) and alkyl pyridinium chloride (C_{12}PCl)
2) salt concentrations (10^{-3} M or 10^{-1} M KCl) in the case of the cationic surfactant C_{12}PCl
3) surfactant loading in the pores (fractional filling $f = \Gamma/\Gamma_m$ = 1, 2/3, and 1/3, where Γ_m is the maximal loading, corresponding to the plateau value of the adsorption isotherms)
4) SLD of water (3.7, 5.0, and D_2O)

The same procedure was applied for sample preparation as former experiments at V4 except refined steps in fractional filling. The SAND measurements were made in aluminium sample cells specially developed for these studies, which are fully compatible to the linear sample changer of D16 at ILL.

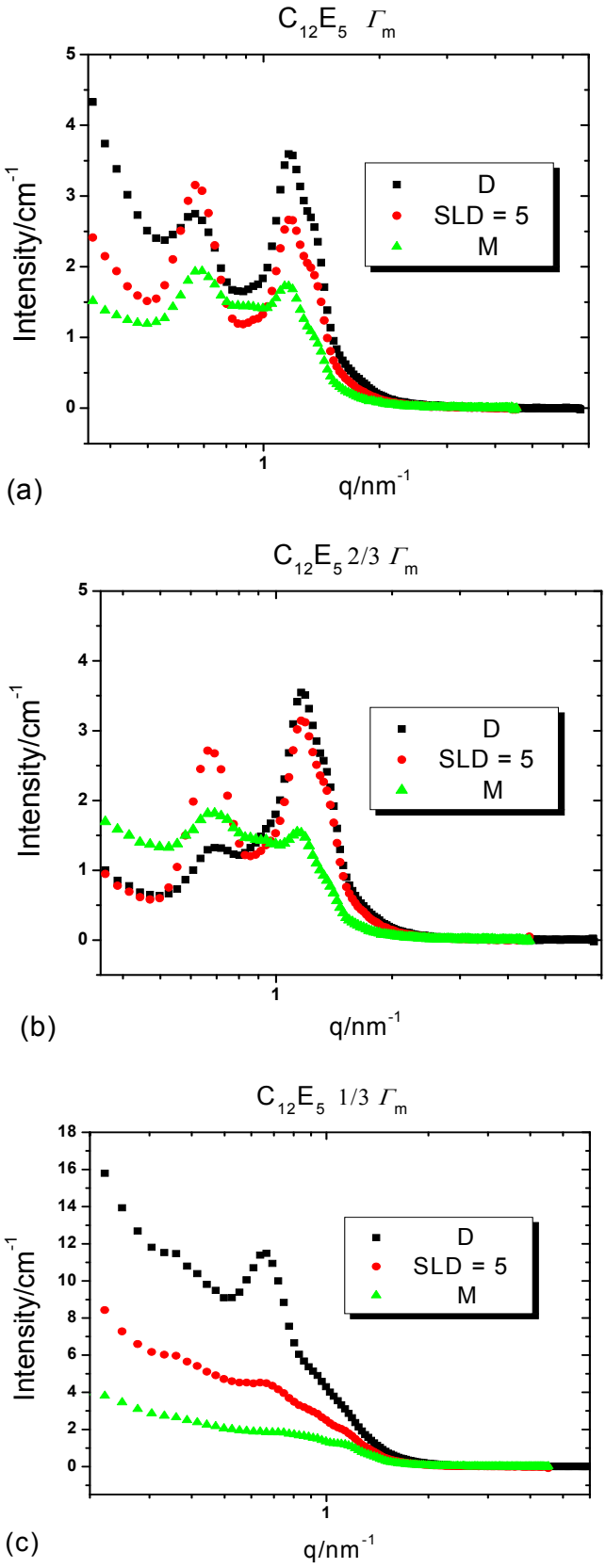

Fig.A.8 Scattering curve of SBA-15 with adsorbed $C_{12}E_5$ at 3 different surfactant loadings and SLDs. To show the effect of the scattering length density of solvent, scattering curves of 3 SLDs are presented together at the same surfactant loading.

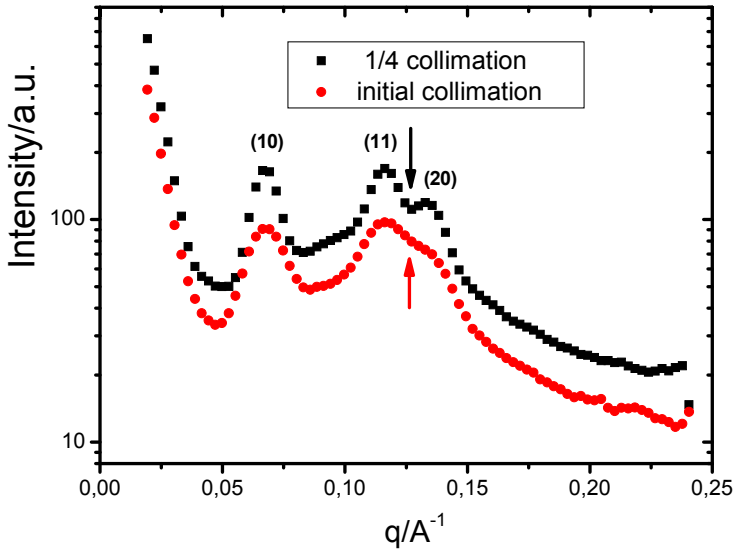

Fig. A.9: Comparison of two scattering curves measured with different collimation. For the test an identical SBA-15 sample adsorbed with $C_{12}E_5$ (67% of Γ_m) was measured with a collimation set up used for all samples of this project (red full circle) as well as with a collimation of quarter cross section to the initial set up (black full square).

D16:9-12-129

Owing to enhanced instrumental resolution and sophisticated planning of experimental scheme, fundamental findings could be made. For this project a collimation setting of 10.43 mm × 10.18 mm (slit 1) and 6.38 mm × 6.24 mm (slit 2) was realised as optimal instrumental resolution with reasonable data acquisition time at the beginning of beam time. This experiment focuses on a quantitative study of the evolution of aggregate structures in the pores as a function of fractional filling $f = \Gamma/\Gamma_{max}$ (Γ_{max}, the maximum adsorption), from $f = 0.15$ to the full extent of plateau value of the experimental adsorption isotherm. The SAND measurements were performed for two non-ionic surfactants ($C_{12}E_5$ and $C_{10}E_5$) and cationic surfactant Dodecyl Pyridinium Chloride (DPCl). In addition to the amount of surfactant the scattering length density of water (a mixture of H_2O and D_2O) was varied from the value of contrast-matching with silica to the highest realizable neutron scattering length density by D_2O.

Samples were prepared in the same way as previous experiment and the same aluminium cells were employed for present measurement.

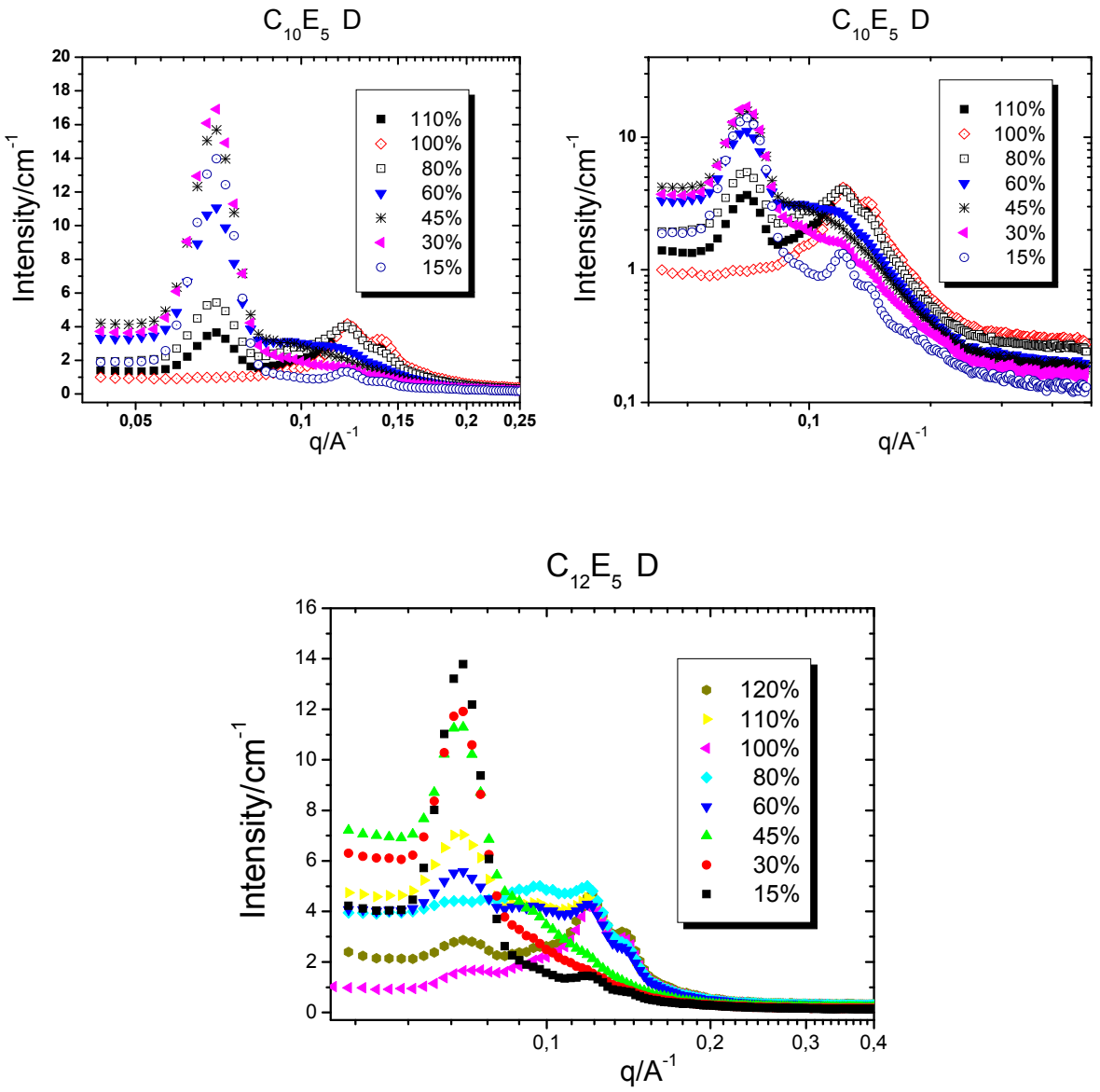

Fig. A.10 Scattering curves of SBA-15 with adsorbed $C_{10}E_5$ and $C_{12}E_5$ in D_2O. The surfactant loading larger than 100% are hier presented which were not presented in Chapter 7 due to unsure equilibrium.

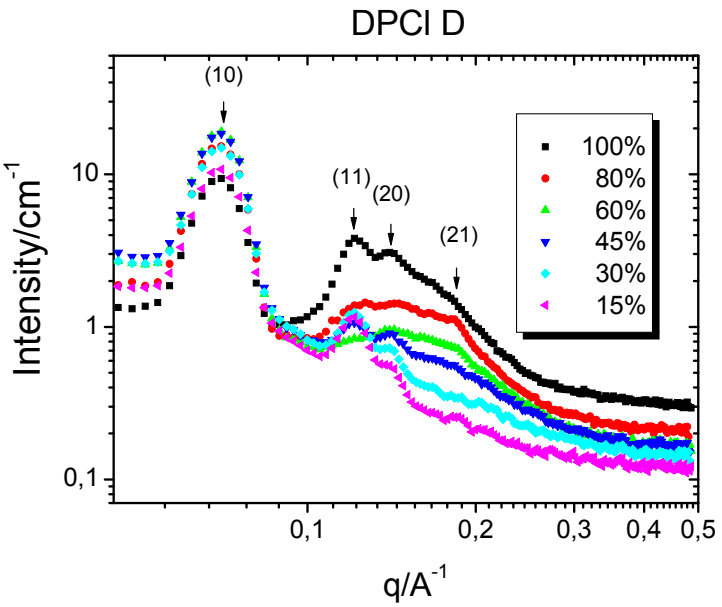

Fig.A.11 Scattering curves of SBA-15 with adsorbed cationic surfactant DPCl in D_2O.

A.3 TGA/DTG results

All detailed individual TGA and DTG profiles for each surfactant loaded SBA-15 sample which were not presented in Chapter 5 will be given in the following. DTG values are multiplied by an appropriate factor and shifted vertically to fit the scale of TGA values.

A.3.1 TGA and DTG profiles for SBA-15 samples with adsorbed $C_{10}E_5$

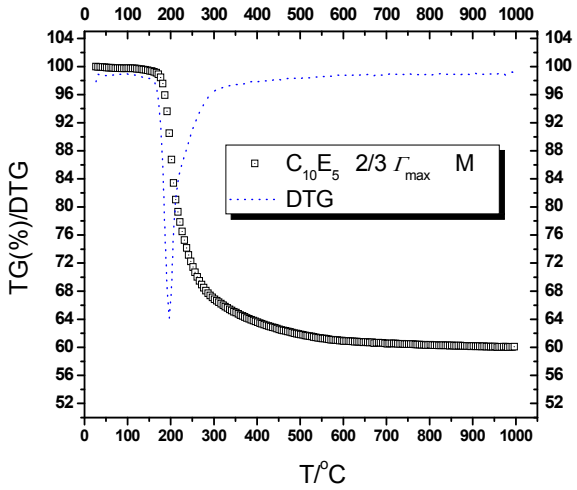

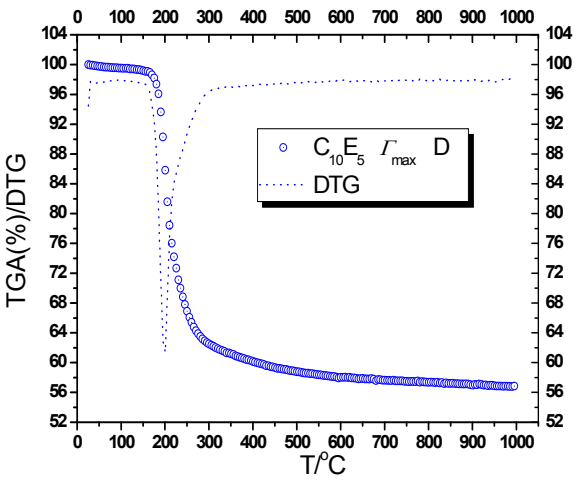

A.3.2 TGA and DTG profiles for SBA-15 samples with adsorbed $C_{12}E_5$

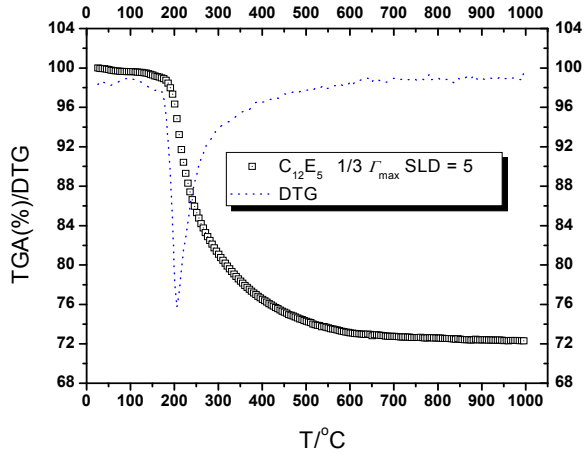

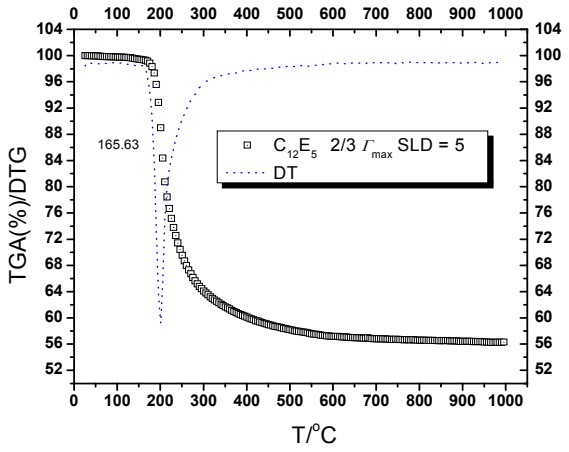

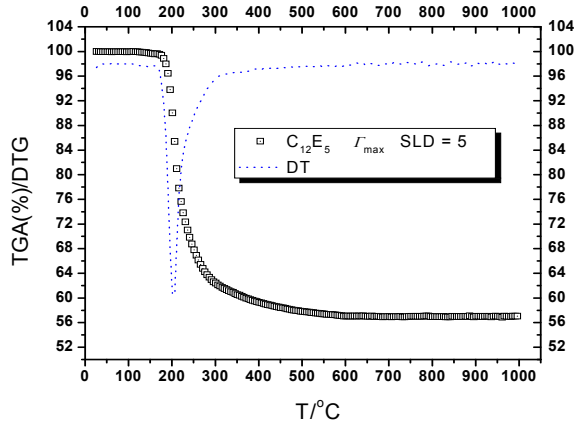

A.3.3 TGA and DTG profiles for SBA-15 samples with adsorbed $C_{10}G_2$

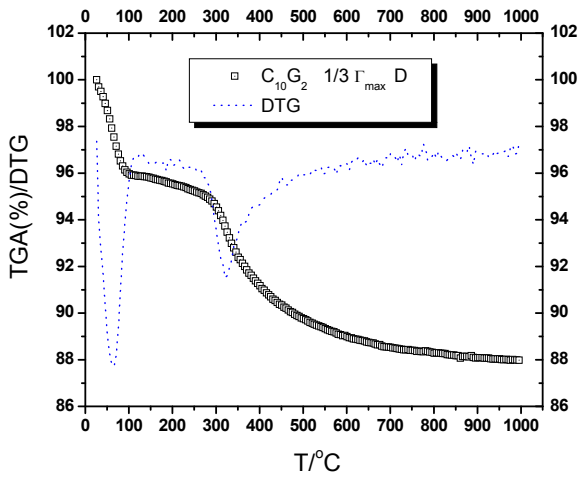

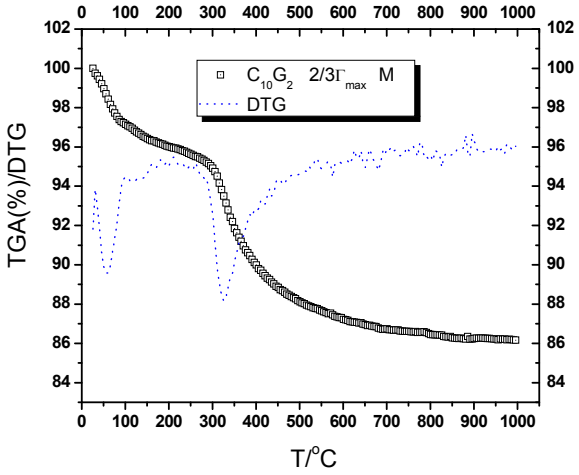

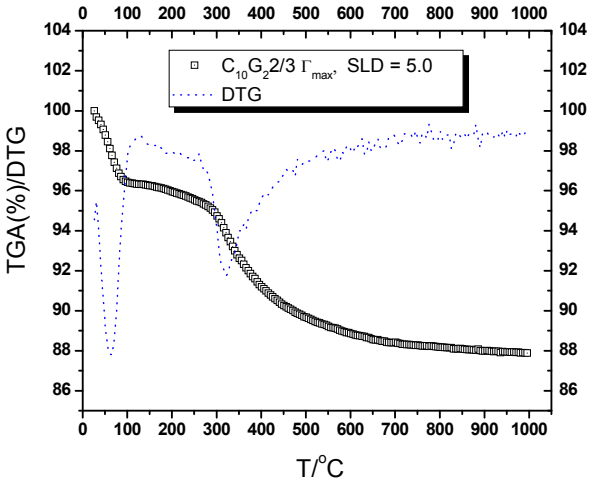

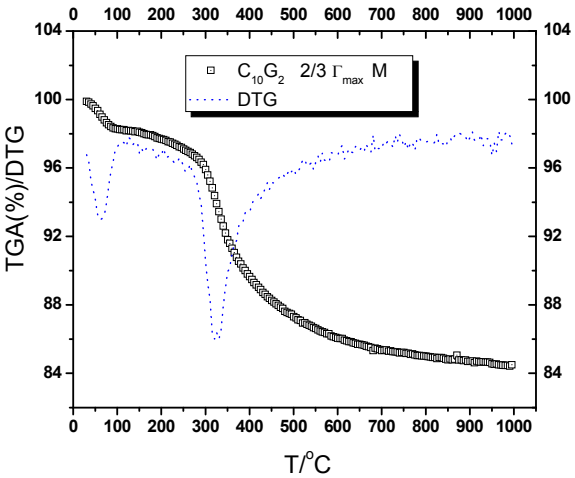

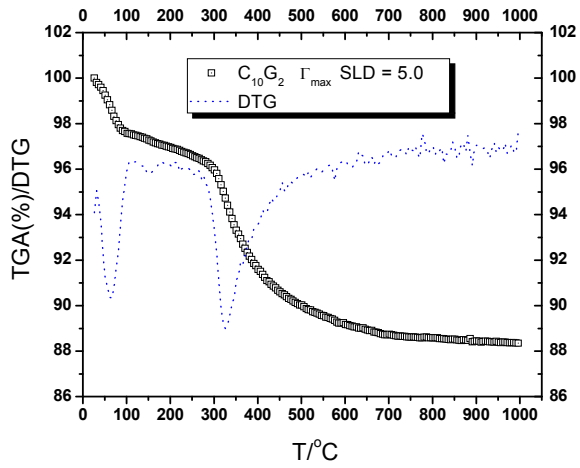

A.3.4 TGA and DTG profiles for SBA-15 samples with adsorbed DPCl

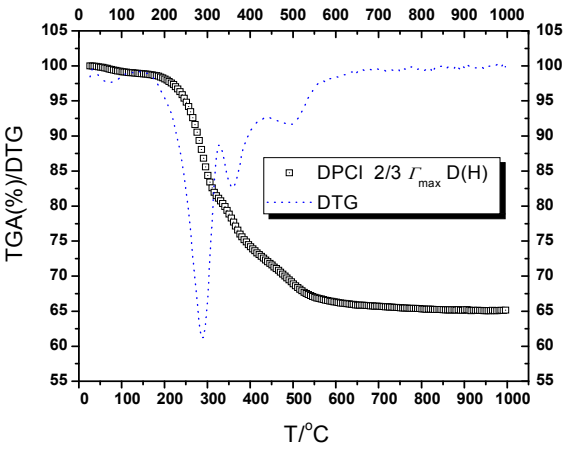

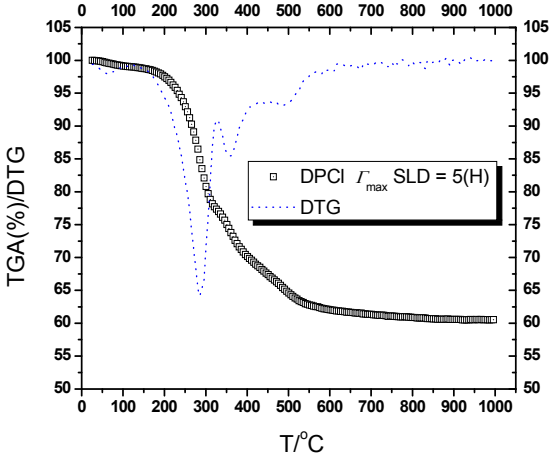

Bibliography

[Arai08] N. Arai, K. Yasuoka, and X.C. Zeng: Self-Assembly of Surfactants and Polymorphic Transitions in Nanotubes. *J. Am. Chem. Soc.* 130, 7916-7920, 2008.

[Atki94] P.W. Atkins: Physical Chemistry. Oxford University Press, 5th Edition. Oxford, Melbourne, and Tokyo, 1994.

[Atki03] R. Atkin, V.S.J. Craig, E.J. Wanless, S. Biggs: Mechanism of cationic surfactant adsorption at the solid-aqueous interface. *Advances in Colloid and Interface Science* 103: 219-304, 2003.

[Berg94] H.E. Bergna (Editor): The Colloidal Chemistry of Silica. *An American Chemical Society Publication*, 1994.

[Bind01] K. Binder, P.Fratzl: „Spinodal Decomposition“, in *Materials Science and Technology,* Vol. 5, Phase Transformations in Materials, 2nd Ed., G. Kostorz, Ed., Wiley VCH, Weinheim, 2001.

[Bunt07] G. Buntkowsky, H. Breitzke, A. Adamczyk, F. Roelofs, T. Emmler, E. Gedat, B. Grünberg, Y. Xu, H.-H. Limbach, I. Shenderovich, A. Vyalikh and G. H. Findenegg: Structural and dynamical properties of guest molecules confined in mesoporous silica materials revealed by NMR. *Phys. Chem. Chem. Phys.* 9: 4843-4853, 2007.

[Caba87] B. Cabane: Chapter 2. Small Angle Scattering Methods in “Surfactant Solutions”- Surfactant science series vol. 22, Edited by R. Zana. Marcel Dekker, Inc. New York, 1987.

[Cumm90] P.G. Cummins, E. Staples, J. Penfold: Study of surfactant adsorption on colloidal particles. *J. Phys. Chem.* 94: 3740-3745, 1990.

[Dab02] A. R. Dabiri, Dissertation, Technical University Berlin 2002.

[deJo06] K. P. de Jong, L. C. A. van den Oetelaar, E. T. C. Vogt, S. Ejisbouts, A. J. Koster, H. Friedrich, and P. E. de Jongh: High-Resolution Electron Tomography Study of an Industrial Ni-Mo/ -Al2O3 Hydrotreating Catalyst. *J. Phys. Chem. B Letters*, 110: 10209-10212, 2006**.**

[Des03] G. Despert, J. Oberdisse: Formation of micelle-decorated colloidal silica by adsorption of nonionic surfactant. *Langmuir 19*: 7604-7610, 2003.

[Diet07] O. Dietsch, A. Eltekov, H. Bock, K. E. Gubbins, and G. H. Findenegg : Crossover from Normal to Inverse Temperature Dependence in the Adsorption of Nonionic Surfactants at Hydrophilic Surfaces and Pore Walls. *J. Phys. Chem. C*, *111* 43: 16045–16054, 2007.

[Dra02] M. Drach, J. Narkiewicz-Michalek, W. Rudzinski, G.H. Findenegg, Z. Király: Calorimetric study of adsorption of nonionic surfactants on silica gel: Estimating the role of lateral interactions between surface aggregates. *Phys. Chem. Chem. Phys.* 4: 2307-2319, 2002.

[Drew] *"Surfaces, Interfaces, and Colloids"* by Drew & Myers, WILEY-VCH.

[Evans94] D.F. Evans, and H.Wennerstrom: The Colloidal Domain, Where Physics, Chemistry, Biology and Technology Meet, Chapter 3, VCH, New York, 1994.

[Feig87] L.A. Feigin, D.I. Svergun: Structure Analysis by Small-Angle X-Ray and Neutron Scattering, plenum Press, New York, 1987.

[Find07] G.H. Findenegg, A.Y. Eltekov: Adsorption isotherms of nonionic surfactants in SBA-15 measured by micro-column chromatography. *Journal of Chromatography A* Volume 1150, Issues 1-2: 236-240, 2007.

[Förs05] S. Förster, A. Timman, M. Konrad, C. Schellbach, A. Meyer, S.S. Funari, P. Mulvaney, and R. Knott: Scattering Curves of Ordered Mesoscopic Materials. *J. Phys. Chem. B*, 109: 1347–1360, 2005.

[Fried09] H. Friedrich, C. J. Gommes, K. Overgaag, J. D. Meeldijk, W. H. Evers, B. de Nijs, M. P. Boneschanscher, P. E. de Jongh, A. J. Verlkleij K. P. de Jong, A. van Blaaderen, and D. Vanmaekelbergh: Quantitative Structural Analysis of Binary Nanocrystal Superlattices by Electron Tomography. *Nano Letters* Vol. 9, No. 7: 2719-2724, 2009

[Garl07] A. Garlarneau, M. Nader, F. Guenneau, F. Di Renzo, and A. Gedeon: Understanding the Stability in Water of Mesoporous SBA-15 and MCM-41. *J. Phys. Chem. C,* 111: 8268-8277, 2007.

[Gior92] F. Giordano, R. Denoyel and J. Rouquerol: Influence of porosity on the adsorption of a non-ionic surfactant on silica. *Colloids and Surfaces A: Physicochemical and Engineering Aspects*, 71:293-298, 1993.

[Golo96] T.P. Goloub, L.K. Koopal and B.H. Bijsterbosch: Adsorption of Cationic Surfactants on Silica. Surface Charge Effects. *Langmuir*, 12: 3188-3194, 1996.

[Golo97] T.P. Goloub and L.K. Koopal: Adsorption of Cationic Surfactants on Silica. Comparison of Experiment and Theory. *Langmuir*, 13: 673-681, 1997.

[Gran98] L.M. Grant, F. Tiberg, W.A. Ducker: Nanometer-scale organization of ethylene oxide surfactants on graphite, hydrophilic silica and hydrophobic silica. *J. Phys. Chem B*, 102: 4288-4294, 1998.

[Hoff05] T. Hoffmann D. Wallacher, P. Huber, R. Birringer, K. Knorr, A. Schreiber, G.H. Findenegg: Adsorption and capillary condensation of Kr in a periodic mesoporous silica studied by X-ray small-angle diffraction. *Phys. Rev. B*, 72: 064122, 2005.

[How01] J.R. Howse, R. Steitz, M. Pannek, P. Simon, D.W. Schubert, G.H. Findenegg: Adsorbed Surfactant layers at polymer/lLiquid interfaces. A neutron reflectivity Study. *Phys. Chem. Chem. Phys.* 3: 4044-4051, 2001.

[Huin97] H.P. Huinink, A. de Kaizer, F.A.M. Leermakers, and J. Lyklema: Nonionic surfactants in cylindrical hydrophilic pores. *Progr. Colloid Polym. Sci.* 105:91-95, 1997.

[Imp00] M. Impéror-Clerc, P. Davidson, and A. Davidson: Exisrence of a Microporous Corona around the Mesopores of Silica-Based SBA-15 Materials Templated by Triblock Copolymers. *J. Am. Chem. Soc.* 122: 11925, 2000.

[Jaro06] M. Jaroniec and L.A. Solovyv: Improvement of the Kruk-Jaroniec-Sayari Method for Pore Size Analysis of Ordered Silicas with Cylindrical Mesopores. *Langmuir*, 22: 6757-6760, 2006.

[Leer05] F.A.M. Leermakers, L.K. Koopal,; W.J. Lokar, and W.A. Ducker: Modeling of Confinement- induced Phase Transitions for Surfactant Layers on Amphiphilic Surfaces. *Langmuir*, 21, 11534-11545, 2005.

[Lin94] M. Y. Lin, S. K. Sinha, J. M. Drake, Wu, P. Thiyagarajan, H. B. Stanley: Study of phase separation of a binary fluid mixture in confined geometry Export. *Physical Review Letters*, 72(14): 2207-2210, 1994.

[Lipf07] J. Lipfert, L. Columbus,V. B. Chu, S. A. Lesley, and S. Doniach : Size and Shape of Detergent Micelles Determined by Small-Angle X-ray Scattering. *J. Phys. Chem. B*, 111: 12427-12438, 2007**.**

[Loka04] W.J. Lokar and W.A. Ducker: Proximal Adsorption at Glass Surfaces: Ionic Strength, pH, Chain Length Effects. *Langmuir*, 20: 378-388l, 2004.

[Lug09] D. Lugo, J. Oberdisse, M. Karg, R. Schweins, G.H. Findenegg: Surface Aggregate Structure of Nonionic Surfactants on Silica Nanoparticles. *Soft matter*, 5(15): 2928-2936, 2009.

[Mir07] S.A. Mirji, S.B. Halligudi, N. Mathew, N.E. Jacob, K.R. Patil, and A.B. Gaikwad: Adsorption of methanol on mesoporous SBA-15. *Material Letters* 61: 88-92, 2007.

[Möll99] A. Möller: Streuexperimente an Tensidmizellen. Dissertation, Technical University Berlin 1999.

[Müt10] D. Müter, T. Shin, B. Demé, P. Fratzl, O. Paris, and G. H. Findenegg: Surfactant Self-Assembly in Cylindrical Silica Nanopores. *J. Phys. Chem. Lett.* 1, 1442-1446, 2010.

[Nala08] J. Nalaskowski, J. Drelich, and J.D Miller: Forces between Polyethylene Surfaces in Oxyethylene Dodecyl Ether Solutions as Influenced by the Number of Oxyethylene Groups. *Langmuir*, 24, 1476-1483, 2008.

[Pari04] S. Paria and K.C. Khilar: A review on experimental studies of surfactant adsorption at the hydrophilic solid-water interface. *Advances in Colloid and Interface Science* 110: 75-95, 2004.

[Patr97] H.N. Patrick, G.G. Warr, S. Manne and I.A. Aksay: Self-Assembly Structures of Nonionic Surfactants at Graphite/Solution Interfaces. *Langmuir*, 13: 4349-4356, 1997.

[Pen02] J. Penfold, E. Staples, I. Tucker: On the consequences of surface treatment on the adsorption of nonionic surfactants at the hydrophilic silica-solution interface. *Langmuir* 18: 2967-2970, 2002.

[Qiao03] Y. Qiao, M. Schönhoff, G.H. Findenegg: 2H NMR investigation of the structure and dynamics of the non-ionic surfactant C12E5 confined in Controlled-pore Glass. *Langmuir* 19: 6160-6167, 2003.

[Rubi91] D.N. Rubingh, P.M. Helmel, *Nonionic Surfactants*, Surfactant Science Series, Vol. 37. Marcel Dekker, Inc., 1991.

[Sche05] S. Schemmel, G. Rother, H. Eckerlebe, and G.H. Findenegg: Local structure of a phase-separating binary mixture in a mesoporous glass matrix studied by small-angle neutron scattering. *J Chem Phys*. 122(24): 244718, 2005.

[Schi87] M.J. Schick, *Nonionic Surfactants*, Surfactant Science Series, Vol. 23. Marcel Dekker, Inc., 1987.

[Schm06] R. Schmuhl, A. van der Berg, D.H.A. Blank, J.E. ten Elshof: *Angew. Chem. Int. Ed.* 45, 3341-3345, 2006.

[Schre01] A. Schreiber, I. Ketelsen, and G.H. Findenegg: Melting and freezing of water in ordered mesoporous silica materials. *Phys. Chem. Chem. Phys*., 3: 1185 – 1195, 2001.

[Shend03] I. G. Shenderovich, G. Buntkowsky, A. Schreiber, E. Gedat, S. Sharif, J. Albrecht, N. Golubev, G. H. Findenegg and H.-H. Limbach: Pyridine- ^{15}N – A Mobile NMR Sensor for Surface Defects of Mesoporous Silica. *J. Phys. Chem. B* 107: 11924-11939, 2003.

[Shin06] T. Shin and G. H. Findenegg: Surfactant Adsorption in Ordered Mesoporous Silica Studied by SANS. *Progr Colloid and Polym Sci.* 133, 116-122, 2006.

[Stei04] R. Steitz, P. Müller-Buschbaum, S. Schemmel, R. Cubitt, G.H. Findenegg: Lateral structure of a surfactant adsorbed layer at a hydrophilic solid/liquid interface. *Europhys. Lett.* 67: 962-968 2004.

[Strey90] R. Strey, R. Schomäcker, D. Roux, F. Nallet, and U. Olsson: J. Chem. Soc. Faraday Trans. 86: 2253, 1990.

[Stub01] C. Stubenrauch: Sugar surfactants – aggregation, interfacial, and adsorption phenomena. *Current Opinion in Colloid & Interface Science* 6: 160-170, 2001.

[Tale01] F. I. Talens-Alesson, R. Urbanski, and J. Szymanowski: Evolution of resistance to permeation during micellar enhanced ultrafiltration. *Coll. Surf. A*, 178 71-77, 2001.

[Teub87] M. Teubner and R. Strey: Origin of the scattering peak in microemulsions. *J. Chem. Phys.* 87: 3195-3200, 1987.

[Tibe96] F. Tiberg: Physical characterization of non-ionic surfactant layers adsorbed at hydrophilic and hydrophobic solid surfaces by time-resolved ellipsometry. *J. Chem. Soc., Faraday Trans.* 92: 531-538, 1996.

[Warr00] G.G. Warr: Surfactant adsorbed layer structure at solid/solution interfaces: impact and implications of AFM imaging studies. *Current Opinion in Colloid & Interface Science* 5:88-94, 2000.

[Zha97] L. Zhang, P. Somasundaran, and C. Maltesh: Adsorption of n-Dodecyl-β-D-maltoside on Solids. *Journal of Colloid and Interface Science* 191: 202-208, 1997.

[Zhao98-1] D. Zhao, J. Feng, Q. Huo, N. Melosh, G. H. Fredrickson, B. F. Chmelka, and G. D. Stucky: Triblock Copolymer Syntheses of Mesoporous Silica with Periodic 50 to 300 Angstrom Pores. *Science* 279: 548, 1998.

[Zhao98-2] D. Zhao, Q. Huo, J. Feng, B. F. Chmelka, and G. D. Stucky: Nonionic triblock and star diblock copolymer and oligomeric surfactant syntheses of highly ordered, hydrothermally stable, mesoporous silica structures. *J. Am. Chem. Soc.* 120: 6024, 1998.

[Zhu89] B. Zhu and T. Gu: General Isotherm Equation for Adsorption of Surfactants at Solid/Liquid Interfaces. *J. Chem. Soc., Faraday Trans. 1*, 85(11): 3813-3817, 1989.

[Zick06] G.A. Zickler, S. Jähnert, W. Wagermaier, S.S. Funari, G.H. Findenegg, and O. Paris: Physisorbed films in periodic mesoporous silica studied by in situ synchrotron small-angle diffraction *Phys. Rev. B*, 73: 184109, 2006.